

Single-Molecule Investigations Into How Plant Kinesin-12 Motor Proteins Accurately Align The Cell Division Plane

Dissertation
der Mathematisch-Naturwissenschaftlichen Fakultät
der Eberhard Karls Universität Tübingen
zur Erlangung des Grades eines
Doktors der Naturwissenschaften
(Dr. rer. nat.)

vorgelegt von
Mayank Chugh
aus Panipat, Indien

Tübingen
2019

Gedruckt mit Genehmigung der Mathematisch-Naturwissenschaftlichen Fakultät der Eberhard Karls Universität Tübingen.

Tag der mündlichen Prüfung

24.09.2019

Dekan

Prof. Dr. Wolfgang Rosenstiel

1. Berichterstatter:

Prof. Dr. Erik Schäffer

2. Berichterstatter:

Prof. Dr. Gerd Jürgens

To more deserving people who lack opportunities and resources to
chase their dreams in our inequitable world

Abstract

Plant cytokinesis is the ultimate step in cell division that partitions the parent cell into two daughter cells by the physical insertion of a cell plate. The accurate placement of the cell plate aided by the microtubule-based phragmoplast is indispensable as it governs proper morphology and further plant development. However, how a plant cell correctly orients and inserts the maturing cell plate into the right location of the plasma membrane is poorly understood. Two kinesin-12 members, phragmoplast orienting kinesin 1 and 2 (POK1 and POK2), are involved in the process, but how these molecular machines work is not known. It has been hypothesized that these POK motors guide the phragmoplast by interacting with the peripheral microtubules emanating from it.

In this thesis, single-molecule fluorescence and force spectroscopy of motor domains of POK1 and POK2 has been carried out to determine how these *Arabidopsis thaliana* motors function mechanically. It was found that POK1 and POK2 kinesin motors are moderately fast, plus-end-directed microtubule motors, which are capable of exerting forces. Interestingly, both motors switch between processive and diffusive modes that was quantified by an exclusive-state mean-squared-displacement analysis. Furthermore, the motors are the weakest kinesins characterized to date attributed to the latter switching behaviour. After establishing the polarity of peripheral microtubules in the root meristem of *Arabidopsis*, jointly the data support a model that POK motors push against the peripheral microtubules of the expanding phragmoplast. These pushing forces contribute to the proper guidance of the phragmoplast to possibly refine cell plate fusion site and orientation of the cell plate.

Intriguingly, the single-molecule characterization of the tail domain of POK2 revealed a novel microtubule-associated motor distinct from kinesins, dyneins, and myosins. This motor exhibits slow, processive, plus-end motility. Moreover, this tail domain is also capable of membrane binding preferentially to the phosphatoinositides. Therefore, this thesis proposes potential roles of POK2 in guiding as well as stabilizing and connecting the expanding phragmoplast to the plasma membrane.

In sum, this thesis provides mechanical insights into how active motors may assist in accurate positioning of cell walls in plants. Moreover, the finding of a new cytoskeletal motor may open avenues for detailed investigation and new discovery of related molecular machines.

Zusammenfassung

Die Zytokinese bei Pflanzen ist der letzte Zellteilungsschritt, bei dem die Eltern-Zelle durch physisches Einbauen einer Zellplatte in zwei Tochter-Zellen geteilt wird. Die genaue Platzierung dieser Zellplatte durch den Phragmoplasten, ist unverzichtbar, da sie die richtige Morphologie und die weitere Pflanzenentwicklung regelt. Die Art und Weise wie eine Pflanzenzelle die wachsende Zellplatte korrekt orientiert und an die richtige Stelle in der Plasmamembran einfügt, ist jedoch kaum verstanden. Zwei Mitglieder der Kinesin-12-Familie, Phragmoplast-orientierendes Kinesin-1 und -2 (POK1 und POK2), sind in diesen Prozess involviert, aber wie diese molekularen Maschinen funktionieren, ist unbekannt. Es wird vermutet, dass diese POK-Motoren den Phragmoplasten durch Interaktion mit den davon ausgehenden Mikrotubuli ausrichten.

In dieser Arbeit wurden die Motordomänen von POK1 und POK2 mit Einzelmolekülfluoreszenz- und kraftmikroskopie charakterisiert, um herauszufinden, wie diese Motoren der Spezies *Arabidopsis thaliana* mechanisch funktionieren. Die Messungen zeigen, dass konventionelle POK1- und POK2-Motoren mittelmäßig schnelle, zum Mikrotubulus Plus-Ende gerichtete Motoren sind, die nur sehr kleine, Kräfte ausüben. Interessanterweise wechseln beide Motoren zwischen Phasen diffusiver und gerichteter Bewegung, was durch eine exklusive Zustandsanalyse der mittleren quadratischen Abweichungen herausgefunden wurde. Nachdem die Polarität der peripheren Mikrotubuli im Wurzel-Meristem von *Arabidopsis* etabliert wurde, unterstützen die Daten zusammengefasst ein Modell, nach dem die POK-Motoren gegen die peripheren Mikrotubuli des expandierenden Phragmoplasts drücken. Diese Druckkräfte präzisieren möglicherweise die richtige Ausrichtung des Phragmoplasten und der Zellplatte.

Spannenderweise enthüllte die Einzel-Molekül-Charakterisierung der Schwanz-Domäne von POK2 die Existenz eines neuen aber Mikrotubulus-assoziierten Motors. Distinkt von Kinesin, Dynein und Myosin motoren Dieser neue Motor bewegt sich langsam aber prozessiv in Richtung des Mikrotubulus Plus-Ende. Außerdem ist diese Schwanzdomäne auch zum Binden an Membranen fähig, bevorzugt an Phosphoinositolen. Deshalb unterstützt diese Arbeit potenzielle Rollen von POK2 sowohl bei der Ausrichtung als auch der Stabilisierung des expandierenden Phragmoplasten, was für das akkurate Einbauen der Zellplatte notwendig ist.

Zusammengefasst liefert diese Arbeit Einsichten darüber, wie aktive Motoren beim Positionieren der Zellwände in Pflanzen mechanisch helfen können. Darüberhinaus ermöglicht die Entdeckung des neuen Zytoskelettmotors dessen detaillierte Untersuchung und die Entdeckung weiterer unbekannter verwandter Motoren.

Contents

I. Background	3
1. Cytoskeleton and associated molecular motors	5
1.1. Cytoskeleton	5
1.1.1. Microtubules	5
1.1.2. Actin	9
1.2. Cytoskeleton associated motors	10
1.2.1. Kinesins	11
1.2.2. Dyneins	13
1.2.3. Myosins	15
1.2.4. The design plan of cytoskeletal motors	16
2. Plant cytokinesis	19
2.1. Division plane selection and the preprophase band	20
2.2. Division site and the molecular memory	21
2.3. Phragmoplast and the kinesin-12 family	22
2.4. Evolution of cell division in plants	24
3. The power of reconstituted assays in cell biology	27
4. Aim of this work	29
II. Methods	31
5. The genes: construct designing and preparation	33
5.1. Whole RNA isolation	33
5.2. Whole genomic DNA isolation	33
5.3. Complementary DNA or cDNA synthesis	34
5.4. Agarose gel electrophoresis	34
5.5. Polymerase chain reaction (PCR)	34
5.6. DNA purification—gel extraction and PCR clean-up	35
5.7. Restriction digestion and ligation	35
5.8. Chemically competent cell preparation	36
5.9. Bacterial transformation using chemically competent cells	36
5.10. Luria Bertini (LB) media for bacterial growth	37
5.11. Plasmid preparation Mini and Midi	37

6. The proteins: expression and purification of proteins	39
6.1. Protein expression using SF9 insect cells	39
6.2. Protein purification	39
6.3. SDS-PAGE electrophoresis	40
6.4. Coomassie brilliant blue staining	40
6.5. Native-PAGE electrophoresis	40
6.6. Western blotting	41
7. The lens: microscopic techniques and sample preparation	43
7.1. Optical tweezers	43
7.1.1. Working principle	43
7.1.2. Design	44
7.2. Total internal reflection fluorescence (TIRF) microscopy	46
7.2.1. Working principle	46
7.2.2. Design	47
7.3. Microscopy assays	47
7.3.1. Glass cleaning	48
7.3.2. Silanisation	48
7.3.3. Flow cell preparation	49
7.3.4. Microtubule polymerization—taxol stabilisation	49
7.3.5. Microtubule polymerization—GMP-CPP stabilisation	49
7.3.6. Polarity marked microtubules	50
7.3.7. Microscopy assay and imaging conditions	50
7.3.8. Photobleaching assay	50
7.3.9. Microsphere preparation and force measurements	51
7.3.10. PIP strip assay	51
III. Results and Discussion	53
8. The kinesin motor domains of POK2 and POK1	55
8.1. POK2 _{1–589} -GFP is a plus-end-directed dimeric motor	55
8.2. POK2 _{1–589} -GFP motor switches between processive and diffusive modes	57
8.3. MSD analysis of POK2 _{1–589} -GFP motility modes	59
8.3.1. Derivation of MSD equation	61
8.4. SCI analysis of POK2 _{1–589} -GFP	64
8.5. POK2 _{1–589} -GFP is a weak motor	66
8.6. POK1 _{1–564} -GFP is a plus-end-directed motor	68
8.7. POK1 _{1–564} -GFP also switches motility modes	70
8.8. Multiple POK1 _{1–564} -GFP motors generate higher forces than multiple POK2 _{1–589} -GFP	71
8.9. Plus-ends of peripheral microtubules point towards the division site	72
8.10. Pushing model for the phragmoplast guidance	73
8.11. Implications of the pushing model for the phragmoplast guidance	75

9. The POK2 tail contains a membrane binding domain and Xenosin—a new microtubule motor	79
9.1. Bioinformatic analysis of the POK2 C-terminus	79
9.2. POK2 _{2083–2771} -GFP has a secondary microtubule binding site	81
9.3. POK2 _{2083–2771} -GFP displays microtubule plus-end motility	82
9.4. POK2 _{2083–2771} -GFP might be an unconventional microtubule motor	83
9.5. Implications of the microtubule motor in the POK2 tail	87
9.6. POK2 anchoring at the membrane	88
9.7. POK2 _{2083–2771} -GFP does not bind actin filaments	91
9.8. Proposed role of POK2 during plant cell division	92
9.9. Evolutionary aspects of POK2	95
IV. Closure	99
10.Outlook	101
Publications	107
List of Figures and Tables	109
Acknowledgments	121
11.Appendix: list of primers	123
Bibliography	125

Cells are ensembles of molecules interacting within boundaries. Some of the molecules are organised into supramolecular assemblies that have been likened to molecular machines. But the machine metaphor is rather limiting if we imagine machines of the human-made type such as we see around us. What human-made machine assembles itself from parts? What machine is constantly in material flux, tossing out parts and taking in new ones? What machine can repair itself? Yet these are all properties of many of the molecular machines found in cells—including the microtubule machine. organisation in the cell depends on a continuity of form, not on individual molecules. It operates far from equilibrium and disintegrates if not supplied with an input of energy. A big challenge for cell biology is to understand the emergent, self-organizing properties of interdependent molecular systems. It is likely that a successful response to this challenge will require multidisciplinary approaches, including a heavy dose of biophysics, systems analysis and computer modelling. It may be, following a quote from Richard Feynman, that we will not be able to fully understand these systems until we can create them. -Gary Borisy [1]

Introduction

Cytokinesis—*cyto* meaning cellular, *kinesis* meaning movement—is the ultimate step in cell division that partitions the parent cell into two daughter cells. It is a highly orchestrated process that kicks in after the parental DNA is properly segregated. Cytokinesis relies upon exquisite coordination amongst cytoskeleton, motor proteins, membrane dynamics, signalling, and a plethora of other proteins that enable such kinship. One particular, vital ingredient in cytokinesis is *alignment*. The coordination of protein assemblies assist accurate geometry sensing in the cell and precise alignment of cellular structures. Such an interplay leads to separation of cells at pre-determined, right positions. In animals, cytokinesis is achieved by cortical remodelling initiated and maintained by the anaphase spindle, thus marking the cytokinetic spot. Finally, the cells are abscised into two with the help of an actomyosin-based contractile ring. In plants, this fundamental process takes a different approach due to the rigid cellulosic walls outside the parental cell. Therefore, in plants a specialized cytoskeletal apparatus—the preprophase band—possibly dictates/organizes the division plane even before the spindle appears. Eventually, a physical membranous sheet called the cell plate is created inside the cell that causes separation of the two daughter cells. The cell plate is formed, expanded, and inserted into the pre-determined site by virtue of another cytokinetic structure—the phragmoplast. The accurate alignment of the cell plate becomes quite important in plants as it dictates morphological and functional roles that cells play during development.

This thesis aims at understanding functional roles of two microtubule-associated motor proteins namely, phragmoplast orienting kinesin 1 and 2 (POK1 and POK2), during accurate alignment of the cell division plane in *Arabidopsis thaliana*. The thesis presents the current knowledge, methods, new data, and proposes possible roles of POKs in rightly aligning the cell plate in plants. The thesis is divided into three parts. Part I or Background, takes a bottom-up approach describing the cytoskeleton and motor proteins that eventually serve as a basis for plant cell division plane prediction, cell plate formation, and ultimately separation of two daughter cells. Part I also provides a perspective on the reconstituted *in vitro* experimental approach in understanding an ensemble problem in an individualistic manner. This single-molecule system is the prime approach taken to this thesis to understand POKs function. Part II or Methods enlists all the experimental methods used. Part III or Results and discussion is split into two chapters. The first chapter, Chapter 8, unveils the single-molecule characterization of motor domains of POK1 and POK2. Based on the data gathered, the chapter proposes role of POK1 and POK2 in the alignment process during cytokinesis. The second chapter, Chapter 9, uses POK2 as a model system to decipher the unusual roles that the extraordinary tail of these kinesin plays. A comprehensive model of full-length POK2 functions during cell division is postulated. This chapter ultimately provides an evolutionary perspective of the kinesin-12 family in *Arabidopsis* focussing on POK2. Part IV or closure concisely provides an outlook for future understanding of POK2 and POK1 during cell division in plants.

Part I.
Background

1. Cytoskeleton and associated molecular motors

1.1. Cytoskeleton

Cells come in a myriad of shapes and sizes, from discoidal red blood cells to polygonal hepatocytes, to extensively branched neurons, to edgy and cuboidal cells in plants. Such assorted cellular architectures are established and maintained by dynamic intracellular networks of structural elements, together called as the cytoskeleton. The cytoskeleton plays a key role in cell shape, migration, motility, and polarity. It is also a basis for a plethora of vital processes inside the cell such as splitting of chromosomes during mitosis and creation of daughter cells during cytokinesis. The cytoskeleton also serves as 'tracks' for vesicular transport of cargoes and assist membrane dynamics. Apart from intermediate filaments, the dynamic pillars of the cytoskeleton conserved across the kingdoms are – actin and microtubules.

How do actin filaments and microtubules assemble, maintain themselves and create dynamic networks? These questions are fundamental to our understanding of all biological processes that they drive and regulate. The following sections concisely describe certain aspects of our current understanding of these two structural elements.

1.1.1. Microtubules

Microtubules are hollow cylindrical organelles of 25 nm in diameter but varying length. They are composed of $\alpha\beta$ tubulin heterodimers. These heterodimers arrange in a head-to-tail fashion to create polar protofilaments (Figure 1.1). Thirteen of these protofilaments connect laterally to form a sheet-like lattice that arranges and grows into a stiff cylinder (Figure 1.1).

The polarity of microtubules is intertwined with their dynamic behaviour and together they have indispensable consequences. The basis of dynamicity is the GTP binding site in the tubulin dimer. Both α and β tubulin have a GTP binding site at their longitudinal binding interface. The GTP bound in α tubulin is non-exchangeable as it is buried at the intradimer surface, while the GTP in β tubulin is exposed and exchangeable. Now putting polymerization into context, microtubule growth is regulated by GTP hydrolysis in the β tubulin. When a tubulin dimer is incorporated into a microtubule end, GTP hydrolysis takes place in the β tubulin, but with a slight delay. It is believed that the growing end of the microtubule harbours tubulin in a GTP bound state called the GTP-cap that stabilizes the GDP bound and unstable microtubule shaft (Figure 1.2). This GTP-cap model sufficiently explains the dynamic behaviour of microtubules [2]. The GTP-cap stabilizes the microtubule end and promotes further polymerization, while its detachment leads to rapid shrinkage called catastrophe. This fascinating ability of microtubules to grow and rapidly shrink is

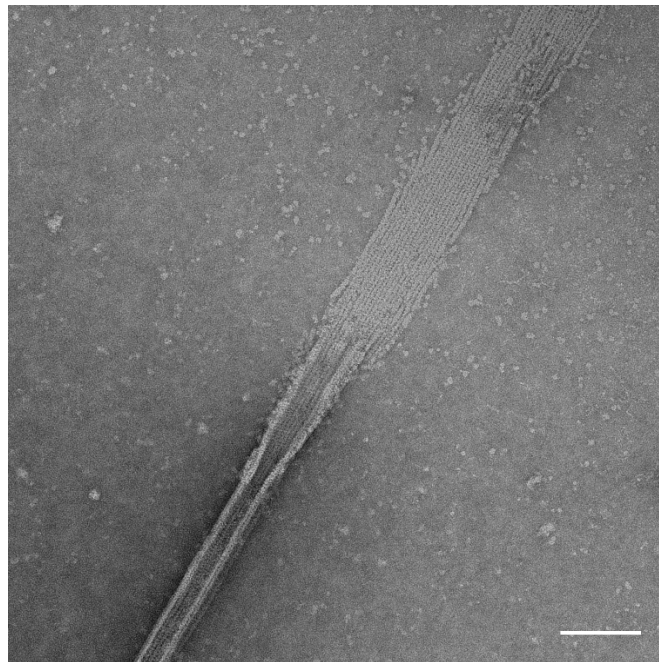


Figure 1.1.: Electron micrograph of a microtubule. A taxol-stabilized microtubule captured at the transmission electron microscope (TEM) in-house facility. The image depicts a microtubule with a hollow cylinder at the bottom and sheet of parallel arranged tubulin resembling beads on a string called protofilaments as it flattens out at the top. Note that there are more than thirteen protofilaments in this microtubule. This is due to *in vitro* polymerization of tubulin without nucleating factors and MAPs. Scale bar 100 nm. This figure was captured with Dr. York-Dieter Stierhof.

called *dynamic instability* [3–5].

Interestingly, this dynamic behaviour is different for both ends (Figure 1.2). The plus-end or the growing end harbouring β tubulin, grows faster (higher polymerization rate) and depolymerizes often (higher catastrophe frequency) compared to the minus-end [6, 7]. Although it is possible to reconstitute this behaviour beautifully *in vitro*, in general, the mechanisms that underlie such dynamic behaviour of a microtubule are not clearly understood. Possibly, these mechanisms are intrinsic as well as extrinsic. Intrinsic being regulated by the tubulin nucleotide state in the lattice versus microtubule ends. Extrinsic regulation by microtubule-associated proteins (MAPs) such as microtubule polymerases, depolymerases, severing enzymes, molecular motors, plus-end-tracking proteins (+TIPs) and minus-end-tracking proteins (-TIPs) [7].

Most of our understanding of microtubule dynamics relies on extrinsic regulation. Apart from regulation of the microtubules themselves, MAPs provide connections to other proteins or cellular structures, concentrate molecules for transportation purposes and thereby, spatially and temporally controlling cellular processes. Among the MAPs, +TIPs are very interesting and important for several reasons. Although involved in tracking the microtubule growing ends, these proteins are usually large, with multiple domains offering sites for binding to other proteins and TIPs [7]. Such binding can take place in a synergistic or competitive or hierarchical manner, thus creating networks [7]. End-binding proteins (EBs) are one of the well studied, autonomous plus-end-tip trackers and considered master regulators of +TIP networks [8–10]. Recent cryo-electron microscopy (EM) studies using GTP- γ S microtubules

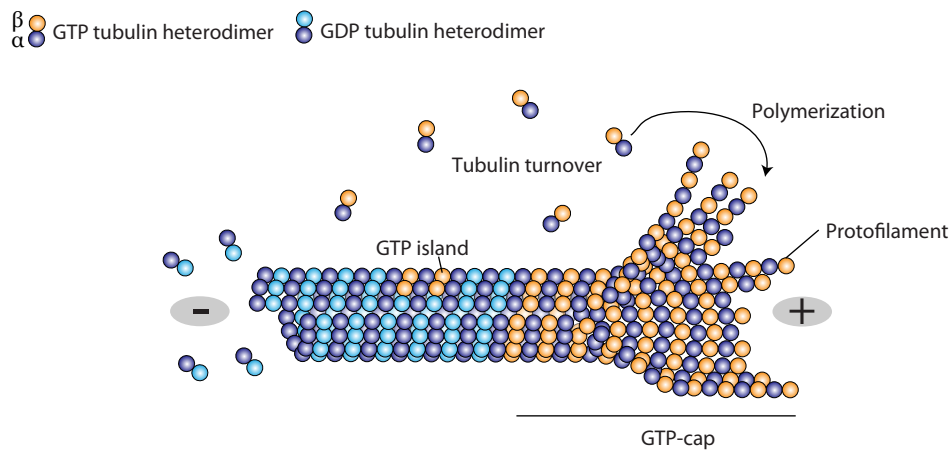


Figure 1.2.: Schematic of microtubule polymerization. The polymerization of microtubules are powered by attachment of GTP bound tubulin heterodimers (orange-purple) at the growing or plus-ends. This defines the GTP cap region at the microtubule growing end. Subsequently, GTP hydrolysis takes place in the β subunit of the heterodimer, resulting in a GDP bound (cyan-purple) microtubule lattice. This constitutes the minus-end of the microtubules. The GDP-bound state of microtubules leads to detachment of tubulin dimers from the minus-ends, thus creating a turnover of tubulin dimers in solution, which will ultimately power microtubule polymerization. Such tubulin turnover causes microtubule treadmilling.

have demonstrated that EB1 binds between two protofilaments, binding among four tubulin dimers [5, 11]. This positioning might enable EBs to sense and adopt changes in the microtubule lattice owing to GTP hydrolysis. Together, it can be assumed that +TIPs give an evolving character to the growing microtubule ends, and steer and regulate microtubule dynamics.

The +TIPs driven networks play a crucial role during *microtubule guidance*, *attachment of plus-ends to cellular substrates*, *microtubule bending*, and *signalling* that sits apriori to complex cellular processes. Motors and other MAP cross-linkers can guide microtubule growth along other microtubule filaments or even actin bundles. Certain motors such as Kif15, Eg5 in humans have been reported to transport microtubules along microtubules, thus creating parallel microtubule bundles or antiparallel sliding, respectively [12, 13]. The mitotic spindle is an outstanding example of such an interplay [14, 15]. Microtubule ends can also collect signalling proteins such as RHO GTPases-guanine nucleotide exchange factors (GEFs) that can modulate for example the actin cytoskeleton [16]. The concentration hubs of +TIPs at the ends, albeit transient, can couple cellular structures and push them along the direction of growth. Such a scenario is thought to propel endoplasmic reticulum (ER) protrusions via EB1 in the direction of microtubule growth [17]. Another interesting scenario is the attachment of dynamic microtubules with kinesin-7 CENP-E, Kif15 and other proteins present at the kinetochores. Such attachment is essential for proper alignment of chromosomes at the metaphase plate [15, 18, 19]. Microtubules can interact with the cortex as well, however, in a complicated manner [20]. Microtubules approaching the cell cortex can be captured, stabilized, or destabilized depending on the MAPs at microtubule ends or at the cortex [20]. In such scenarios, there is a facilitated yet direct interaction of +TIPs at microtubule ends

and with how much loads. Indeed, studies have shown that certain structural modifications can confer different physical strength to the microtubules and alterations in MAP binding. Thus, examining the molecular mechanisms of how tubulin heterogeneity is generated and maintained is very exciting. Besides the specialized cellular functions PTMs dictate, what affect it might have on microtubule dynamics will fathom our basic understanding of these filaments.

1.1.2. Actin

Actin is the most abundant proteins in many cells. It is found in two forms - globular (G) actin and filamentous (F) actin. The globular actin monomers (about 42 kDa) have four subdomains that arrange themselves in a bilobed manner exposing a deep ATP binding cleft between them. Based on the structure, the monomers can be identified with two features - barbed-end groove and pointed-end groove.

Similar to microtubules, actin monomers polymerize spontaneously under physiological conditions to form F-actin of diameter 4–7 nm. The actin filaments are composed of two right-handed strands of actin monomers (Figure 1.4). The whole structure can be visualized as a left-handed single-strand filament. The actin monomers bind ATP and incorporate onto the filament end, where they hydrolyse ATP. This incorporation mainly takes place on the barbed-end, hence giving a polarity to the filament and identifying the barbed-end as the growing end (Figure 1.4). The ATP hydrolysis in the actin lattice is very slow, with the detachment of γ phosphate being the slowest step [25]. It is thought that hydrolysis occurs in a random fashion, however, the nucleotide state of the neighbouring subunits might influence the process. One of the existing and not quite demonstrated hypothesis is that ATP hydrolysis in the actin filaments takes place in a zipper-like manner [26]. Interestingly, actin filaments undergo treadmilling similar to microtubules, where spontaneous depolymerization from the pointed-ends (minus-ends) fuel polymerization at the barbed-ends (plus-ends) [27].

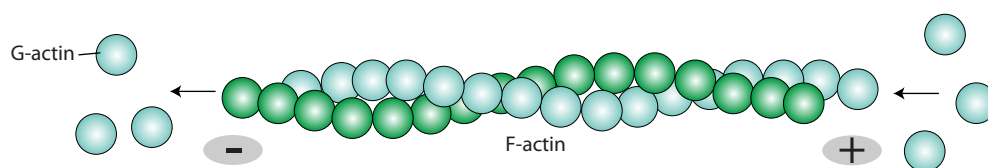


Figure 1.4.: Schematic of actin polymerization. The globular (G)-actin monomers bind ATP and form right-handed strands of filamentous (F)-actin. The barbed ends constitute the growing or plus-ends of the actin filaments while the pointed ends have lower growth rates thus defining minus-ends. Actin assembly and disassembly dynamics is fuelled by ATP hydrolysis and also exhibits treadmilling.

Actin dynamics in the cells is regulated by a variety of actin-binding proteins such as actin-monomer binding proteins, severing proteins, filament polymerases and depolymerases, capping proteins, cross-linking proteins, molecular motors and filament binding proteins. Quite like microtubules, actin filaments establish polar routes for vesicular transport, channel and coordinate cellular signalling and guide growing actin filaments. Interestingly, actin is known to form a huge meshwork via plenty of branching as well as unbranched networks

depending on the network proteins. In fact, in recent years competition between these sorts of intracellular actin networks have been highlighted to execute specific functions [28].

Although there are many functional and modular parallels between actin and microtubule filaments, their lattice structure and mechanical properties set them apart. Actin filaments are thin and flexible polymers, while microtubules are thicker and about 300 times stiffer [29]. Such stiffness allows microtubules to resist, for example, buckling during compressive forces [29]. On the other hand, actin tends to buckle under compressive forces unless bundled together such as in muscle cells. Therefore, the lattice structure and mechanical properties allow them to execute specialized functions. The organisation of microtubules is believed to be more long-range while actin organisation is thought to be a short-range remodeller.

Interestingly, actin has been intimately linked with membranes. Its activity right under the plasma membrane that constitutes the cell cortex is key to cortex stiffness and thus, control of cell shape. The plasma membrane has been shown to control actin activity by two means. A) Regulating the pool of actin monomers via its phosphoinositide lipids, B) modulating actin assembly with the help of guanine triphosphatases (GTPases) which are membrane bound or other assembly assisting proteins that bind to the membrane [30]. Recent studies have shown microtubule stability and cortex actin dynamics are capable of linking in positive and negative ways [30]. For example, spindle orientation in animals have been long proposed to be controlled by cortical actin and astral microtubules. Studies have now reported how the actin cytoskeleton might offer a cortical anchoring platform that could directly or indirectly via motors tether astral microtubules to the membrane, thus, exerting pushing or/and pulling forces to orient the spindle [30].

Therefore, questions such as—are these two cytoskeletal filaments functionally exclusive or can they synergistically drive cellular functions?—have gained momentum in recent years. Studies have demonstrated feedback loops and direct interaction modules between actin and microtubules. There has also been cross-fertilization of filament specific molecular motors that are now shown to interact and drive processes on both the filaments—actin and microtubules. For example, actin bundling kinesin in *Dictyostelium* [31], transport of actin filaments by non-processive rice kinesin-14 OsKCH1 [32] and *Xenopus* microtubule-binding myosin [33] are interesting examples. Identification of more such factors might provide new mechanical and functional insights into cellular networks.

1.2. Cytoskeleton associated motors

The inside of a cell is like a buzzing city that is dynamically organised and maintained by extensive transport systems. How the transport networks or tracks are organised has been described in the section above. But what sort of vehicles are used on those networks is the follow-up question. These intracellular vehicles are called cytoskeletal motors and they harness the energy produced from ATP hydrolysis as fuel to generate mechanical steps. There are three cytoskeletal motors known so far - *kinesins*, *dyneins*, and *myosins*. Kinesins and dyneins are motors that use microtubules as tracks while myosins use actin filaments as tracks.

What sort and how much cargoes can these motors transport? What makes them different from each other? Are their engines wired the same way? Following sections concisely answer these questions with the current state of knowledge.

1.2.1. Kinesins

Kinesins (from the Greek *Kinein*, meaning to move) are microtubule-associated motors that were discovered by Ron Vale and colleagues from giant squid axons and bovine brain in 1985 [34]. Using video microscopy and *in vitro* reconstituted motility assay, they could show that kinesin can translocate vesicles in the axons in an ATP-dependent manner [34]. This particular motor has since been called as kinesin-1 or conventional kinesin, and to date is the gold standard for characterization of any kinesin or cytoskeletal based motor. In the subsequent years after kinesin's discovery, the advent of sequencing tools and screening approaches led to genome-wide identification of motors related to kinesin. The Kinesin family has been expanding since then.

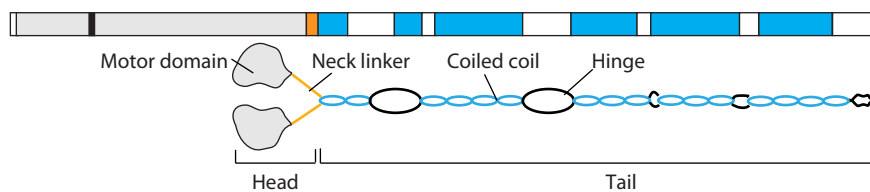


Figure 1.5.: Domain organisation and schematic of conventional kinesin. (*Top*) Domain organisation of human full-length kinesin-1 Kif5b. The Gray region represents the conserved motor domain that contains microtubule and ATP binding sites. The orange sequence represents the neck linker. The cyan stretches represents coiled-coils in the protein. The coiled-coil results were obtained from PCOILS from MPI toolkit (window 28, probability of 0.99–1) [35]. The white regions represents unstructured regions. (*Bottom*) Cartoon representation of a kinesin-1 homodimer with its motor domains, neck linker, coiled-coils and unstructured hinges.

The fundamental element of the kinesin molecule that generates motion is a stretch of about 350 conserved amino acids called the motor domain (Figure 1.5). The motor domain can be further classified into two major parts: a) a catalytic core, is the heart of any motor and consists of highly conserved residues that bind and hydrolyse ATP; b) a neck linker, is the lever that works in concert with the catalytic core to generate movement [36]. It is a fairly conserved region of 40 amino acids that is found towards the N or C terminus of the catalytic core. The microtubule binding domain of the kinesin molecule is also located in the motor domain region. Beyond the motor domain, most kinesins have an α helical coiled-coil region that is termed stalk or tail (Figure 1.5). The coiled-coil motifs in this region can enable oligomerisation and bind light chains, regulatory proteins or other macromolecules. Many kinesins have a globular domain after the stalk that is called tail and directly or in conjunction with other regulatory proteins serve as attachment points to the cargo [36]. The high degree of conservation in the motor domain has allowed classification of kinesin into 14 different families [37]. These families can be broadly divided into three types depending on the location of the motor domain in the protein sequence: N-kinesins possess the motor domain at their N-terminus, C-kinesins and M-kinesins that have motor domain sitting at the C-terminus or in the middle of the protein sequence, respectively. Generally, N-terminal motors are microtubule plus-end-directed kinesins and C-terminal motors are minus-end kinesins. M-Kinesins mostly depolymerize microtubules.

How does transport of macromolecules, mRNA, organelles and cytoskeletal assemblies of cytoskeletal motors such as kinesin operate at nanometre scale? How exactly does a kinesin move over tracks? How much load can it bear? These questions have been the core of research after the kinesin discovery. Insights into the stepping mechanism are mainly from single-molecule *in vitro* reconstituted assays. Using optical tweezers and video based/fluorescence microscopy, studies have clearly established that conventional kinesin is a highly processive homodimeric motor with an average speed of 800–900 nm/s, whereby processivity is defined as the number of steps it takes before detaching from the microtubule lattice requiring a dimeric motor [34, 38, 39]. It has been demonstrated that kinesin-1 takes 8 nm steps with each step being powered by the hydrolysis of one ATP molecule [40]. It takes an average of one hundred steps before it detaches from the microtubule [41, 42]. Using single-head kinesin labelling, it was demonstrated that kinesin-1 walks in a hand-over-hand fashion [43, 44]. The hand-over-hand mechanism describes the kinesin stepping behaviour in which the rear head translocates twice the centre of mass, while the front head does not move. This model is quite fascinating as it has two implications. It predicts symmetric hand-over-hand behaviour, thereby treating the two kinesin heads and microtubule interaction as structurally identical during stepping, and therefore, suggesting that the stalk rotates 180 degrees. On the other hand, asymmetric model advocates no stalk rotation during stepping. Recently, it has been demonstrated that kinesin-1 undergoes stalk rotation simultaneously while stepping in asymmetric hand-over-hand manner, thus generating torque during the movement process [44]. This rotary stepping mechanism can be compared to the winding of the rubber band of a toy aeroplane, as Joe Howard puts it during this mechanism’s prediction in 1996. Given that conventional kinesin is a cargo transporter, how much load it can bear is another intriguing question. Single kinesin-1 molecules have been shown to bear loads up to 5–6 pN [44, 45].

Zooming down further into how exactly does the mechanochemistry produces movement is quite some challenge. There have been controversies over how the two heads interact with the microtubules and what conformational changes are triggered by ATP hydrolysis. The assimilated consensus view of the kinesin-1 mechanochemical cycle [46] has been depicted in Figure 1.6. This model is based on three limitations – a) under saturating ATP concentrations one full cycle is split evenly into two head-bound and one head bound state (however one head bound state is recently questioned [44]), b) ATP binding happens when the two heads are bound to the microtubule lattice, c) ATP hydrolysis takes place prior to the transition from one-head bound to two head-bound state. This understanding serves as a basis for non-canonical walking mechanisms in other kinesins. For example, quite recently, *Arabidopsis* orphan kinesin PAKRP2 has been shown to undertake non-canonical stepping to achieve processivity [47].

Interestingly, characterisation of kinesins from different families and organisms have shown distinct behaviour on the microtubule lattice apart from exclusive processive motion. For example, MCAK, member of human kinesin-13, is a microtubule depolymerase that diffuses onto the microtubule lattice and depolymerizes microtubule ends with an unconventional ATPase cycle [48]. Many other kinesins such as *Drosophila* Kinesin-14 Ncd [49, 50], *Xenopus* Kinesin-7 CENP-E [18], human kinesin-5 Eg5 [51], and human kinesin-12 Kif15 [52] exhibit diffusive motion as an intermittent part of their processive motion. What conformational changes lead to such switching behaviour is not known. Moreover, how force generation is related to the switching behaviour is not understood. If the canonical mechanism is altered due to switching remains elusive. On the functional level, Eg5 and Kif-15 promote

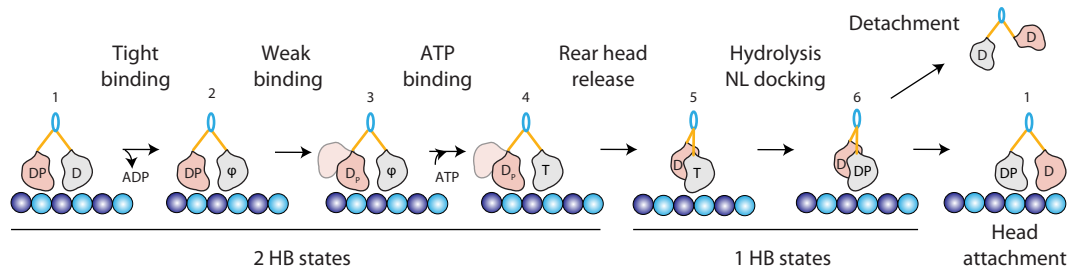


Figure 1.6.: Consensus view of the kinesin-1 mechanochemical cycle. Kinesin-1 binds to the microtubule lattice (cyan-purple) in a tethered two-head state (1). This allows rapid release of ADP from the front head creating an apo/ ϕ state (2). Subsequently, the rear head turns into an ATP waiting state (3). It is presumed during this state (2-3) transition, kinesin heads are weakly bound and may involve release of inorganic phosphate from the rear head. The front head then binds ATP and triggers a conformation change that allows detachment of the rear head (4). The detached rear hand translocates 8 nm forward (5). In this state (5), kinesin-1 is ideally in a one head-bound state. Thereafter, ATP hydrolysis takes place in the former front head in state (6). This hydrolysis event may lead to a new cycle where the kinesin enters once again in two-head bound state (1) with rear head translocating another 8 nm or undergoes detachment from the microtubule lattice. HB: head bound, NL: neck linker. This figure has been modified from [46].

antiparallel-sliding and parallel bundling of microtubules in the metaphase spindle, respectively [12, 13]. Clearly, kinesins do more than solely transport cargo. And therefore, insights into kinesins operating mechanisms is imperative to understand specialized cellular functions they conduct.

1.2.2. Dyneins

Dyneins are one of the huge protein complexes inside cells and the biggest cytoskeletal motor. They are microtubule-based motors that are primarily involved in retrograde transport and are the basis for cilia/flagella structure and beating. Although being discovered as first microtubule-associated motor in 1965 by Gibbons and colleagues, their enormous size makes it to date one of the least characterized and difficult motors to work with [53].

As compared to the kinesin motor domain (about 40 kDa) and myosin motorhead (about 80 kDa), the minimal motor domain of a dynein molecule is about 300 kDa, illustrating the structural complexity posed [54, 55]. However, the speeds and force measurements are of a similar order to processive kinesins, in micrometers per second and 6–7 pN, respectively, however for mammalian dyneins [56]. Yeast dynein exhibit forces up to 1 pN [57]. The dynein family has been divided into two classes - cytoplasmic dynein and axonemal dynein. Cytoplasmic dyneins primarily aids in cargo transport and regulating and orienting the spindle. Axonemal dyneins, located in a periodic manner along the length of the axoneme in flagella/cilia, generate forces that enable the flagella to beat. Despite these classes, their structure is quite similar.

Dyneins are composed of one to three heavy chains that contain the engine for the motors, i.e a microtubule binding site, an ATP binding site and important structural features that

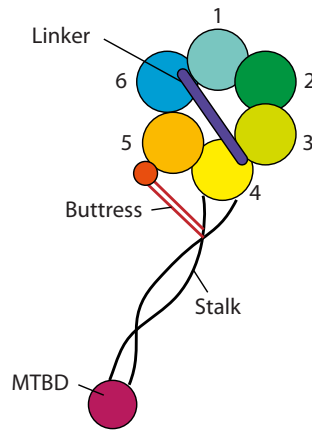


Figure 1.7.: Schematic representation of dynein. A monomeric dynein motor is presented here, although dyneins are capable of forming higher oligomeric structures such as dimers or trimers. Dyneins bind the microtubules via its microtubule binding domain (violet). This domain is separated from the ATP binding and hydrolysis unit with the help of a coiled-coil called stalk (black). The motor activity of dynein is fuelled by an ATPase ring composed of six individual ATP binding motifs, which belong to the AAA+ superfamily. The hexameric ring is co-ordinated among itself with the help of linker (purple). The linker connects two AAA+ domains and is involved in stepping of the dynein motor. The hexameric ring further controls the microtubule binding domain by modulating the stalk with a buttness (dark orange).

translate ATP hydrolysis into mechanical steps [58]. Unlike myosins and kinesins, the motor domain is a globular doughnut like feature that belongs to AAA+ (ATPases Associated with diverse cellular Activities) family. This globular AAA+ head contains six ATP binding motifs, four of which are conserved and hydrolyse ATP with the first pocket being highly conserved (Figure 1.7). Beyond the heavy chain, dyneins are known to interact with other regulatory polypeptides—a light chain, light-intermediate chain, and intermediate chain. These accessory chains are diverse and play regulatory functions for dyneins [58]. Therefore, dyneins by themselves are known to work as monomers or oligomeric forms such as dimers or trimers.

Besides the size, another interesting feature of dyneins is their ability to form huge complexes with other proteins, on top of the basic scaffold described above in the cytoplasm as well as in the axoneme. A few necessary adaptors of dyneins are dynactin, hook2, hook3, and BicD2. Dynactin itself can provide a scaffold for attachment of further proteins including kinesins. These adaptors provide robust dynein function and enable modulation of cellular processes. Such level of complexity makes it even harder to reconstitute such systems *in vitro* and thereby understand dynein regulatory and mechanistic functions.

Single molecule studies suggest that dyneins walk in a hand-over-hand manner but there are irregularities in their stepping behaviour [56, 59]. Studies of yeast cytoplasmic dynein have demonstrated its weak directional bias and variable step sizes (8–32 nm) [58]. The heads of this homodimeric dynein are not coordinated with each other during stepping. In general, how dynein translocates on the microtubule in detail compared to kinesin is still not well understood. Interestingly, dyneins are not present in higher plants [60]. Instead,

minus-end-directed kinesin-14 family has expanded tremendously and might have taken the role of retrograde transport.

1.2.3. Myosins

Myosins are the founding cytoskeletal motors that are actin-based and harness ATP hydrolysis to generate motility and forces. They were discovered in 1864 in Heidelberg by Willy Kühne in muscle extracts [61]. Muscle myosin II or conventional myosin has been a popular example of the actin-myosin based contraction in muscle cells. Most of our understanding of myosins comes from this conventional motor.

After the discovery of kinesins, they were thought to be quite different molecular motors, however, later and in recent years, the basic engine module has proven to be the same [62]. The myosin heavy chain contains the motor domain (80 kDa), which consists of a conserved catalytic core and the neck linker (Figure 1.8) [63]. The motor domain contains actin and ATP binding sites. The neck linker in many myosins serves as a stabilisation point by binding of calmodulin (calcium modulating protein) or calmodulin-like proteins (Figure 1.8). This is quite an interesting aspect of myosins. Beyond the neck region, the C terminal chain makes them very diverse. It can serve as oligomerisation domain, cargo-binding domain, and anchoring sites for actin filaments.

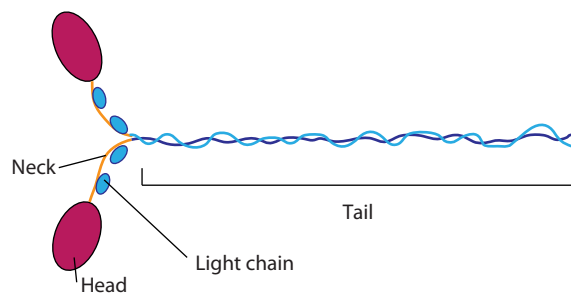


Figure 1.8.: Schematic representation of Myosin. A dimeric myosin-II belonging to conventional myosin family is depicted here. Similar to kinesins, myosin contain a head (violet) that includes an actin binding domain, ATP hydrolysing motif and a huge neck region. The heads are separated from each other with the help of an extended coiled-coil neck region (orange). This neck region serves as prime site for light chain interaction (cyan) and calcium-binding. The neck region is followed up by lengthy coiled-coil domains referred as tail (blue). This tail region also offer interacting sites for the light chains and other molecules. Compared to kinesins, the tail regions in myosins are quite large.

Myosin has been called a superfamily comprised of basically two groups—conventional and unconventional myosins—with many classes among them [63]. Conventional myosins, after myosin II in muscle and non-muscle cells, form a bipolar thick filament that together produces contraction by moving towards the growing end of the actin filaments (Figure 1.8). The well-known examples are muscle contraction, periodic contractile waves during embryogenesis, and cleavage furrow mediated cytokinesis. Interestingly, higher plants are completely devoid of the myosin II family [60]. Unconventional myosins do not form bipolar thick filaments but do move towards the plus and minus-end of actin. The walking mechanism of conventional myosins is a hand-over-hand mechanism coupled to ATP hydrolysis [64]. Myosin motion on the actin filaments has been described as processive or diffusive based on the motor [64, 65].

Myosins are also capable of exerting forces about 3-4 pN depending on the actin tension [66–68].

Myosins are known to regulate several processes using actin filaments—transport of cargo, anchoring or tethering, tension sensing, and actin cytoskeletal organisation.

1.2.4. The design plan of cytoskeletal motors

Kinesins, dyneins, and myosins are specialized cytoskeletal motors that differ from their protein sequence to structure, to size, to walking mechanisms, and of course cytoskeletal type. However, there are certain parallels. One can imagine different vehicles being driven on distinct tracks. In such a case, the tyres and engines of the vehicles might differ but the fundamental principles of designing, running the engine and translation by the tyres remain similar.

Unlike kinesin and myosin, where the microtubule and actin-binding interfaces, respectively, are located in the ATPase surfaces, dyneins have their microtubule binding site located about 15 nm far from the ATPase ring on the edge of a coiled-coil stalk [59]. Considering only the microtubule binding domain and comparing kinesin and dynein, it is apparent that there is not much amino acid sequence similarity. Yet, using the dynein microtubule stalk head and kinesin motor domain it was shown that they both bind to the same binding site on the tubulin lattice [69]. However, the dissociation constant for both are different with low for kinesin (stronger binding) and high for dynein (weaker binding) [69]. It is fascinating that kinesins and dyneins belong to separate families of ATPases yet both bind the same region of tubulin that accounts for only 10-15% of the outer surface area. Kinesins and myosins have evolved from an ancestral G-protein coupled receptor, while dyneins originated from the AAA+ family. Since binding site plays a crucial role in motility, this overlapping binding site can be attributed to convergent evolution [69].

Myosins and kinesins, on the other hand, are motors that bind to different cytoskeletal filaments altogether and share negligible sequence similarity (below 20%). The minimal kinesin motor domain capable of motility *in vitro* is about 350 amino acids long and is much smaller compared to the myosin, i.e. about 850 amino acids long. However, the catalytic core of kinesins shares similarities with myosin [36, 62, 70, 71]. Interestingly, the structure of kinesin also shares this structural similarity to the G-protein family [71]. This similarity is striking in the nucleotide binding site consisting of three motifs—the P-loop, switch I, and switch II [36]. The P-loop is not an unusual motif [72]. It is a phosphate binding motif that is found in many GTP/ATP binding enzymes such as motor proteins, AAA proteins, RecA, transducin, mitochondrial F1-ATPase, adenylate kinases and condensins (SmC—structural maintenance of chromosomes) [72, 73]. The switch motifs work in assistance with the P-loop and realize the binding of nucleotides in the active site. The switches can undergo changes in their confirmation owing to the presence of nucleotide triphosphate (NTP) or nucleotide diphosphate (NDP). This nucleotide dependent conformation change is transmitted to the neighbouring regions of the protein that may alter the binding affinity. Besides this catalytic core, the G-protein and motor structure superimpose poorly. Remarkably for myosin, there is a good superimposition in the three-dimensional (3D) structure in addition to the catalytic core, despite a very low sequence similarity [71]. Considering the conserved function, topology, and ternary structure, G-proteins and the two motor protein families of kinesins and myosins have been attributed to have a common ancestor [70]. The fact that different

group of amino acids are positioned in an identical way in a 3D space, supports that these three families originated from one common ancestor. In the course of evolution, they adopted specialized functions, thus serving as an example of divergent evolution.

2. Plant cytokinesis

Cytokinesis is the last step of cell division. Following chromosome segregation the dividing cell is partitioned into two daughter cells. This process requires a symphonic activity of the cell cytoskeleton, molecular motors, membrane trafficking and dynamics and signalling pathways. In animals, cytokinesis is achieved by cleavage, where an actomyosin contractile ring forms at the division site and separates the daughter cells by abscission (Figure 2.1) [74]. The abscission itself is assisted by the microtubule based structure called midbody (Figure 2.1). Due to the presence of a solid cellulosic cell wall surrounding the plant cells, cytokinesis in plants is strikingly different from animals. Therefore, plant cytokinesis is achieved by physical insertion of a cell plate that is later called the cell wall in the dividing parent cell (Figure 2.1) [75]. Although acentrosomal, plants have evolved unique molecular mechanisms and cytoskeletal apparatus such as the preprophase band and phragmoplast. These structures predict/organize the division site/cell wall insertion site and foster the dynamic formation of the developing cell plate.

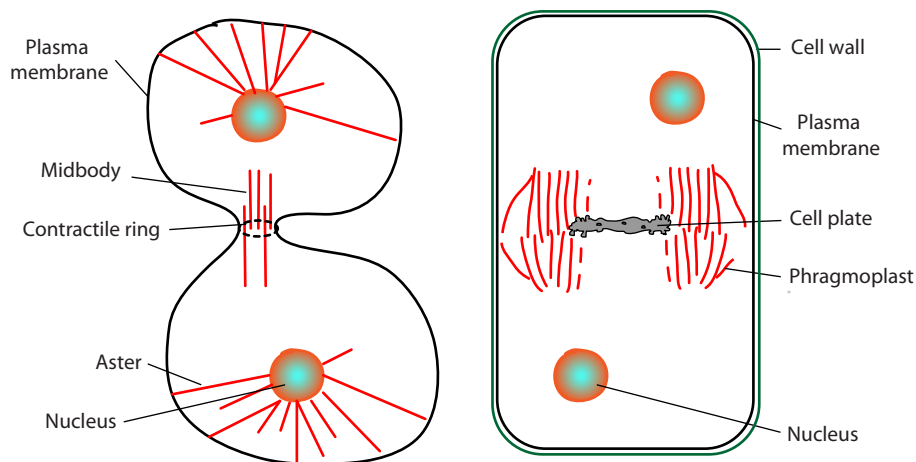


Figure 2.1.: Cytokinesis overview in animals and plants. (*Left*) In animals, cytokinesis is achieved by formation of the actomyosin based contractile ring (black dashed). The two daughter cells are abscised with the help of midbody—microtubule based structure (red). Nucleus positioning in the daughter cells is done via centrosomal asters (red). (*Right*) In plants, cytokinesis is achieved by the physical insertion of the cell plate in the dividing parent cell. The cell wall, present in plants, poses a physical challenge for cleavage-based separation. The cytokinesis is accomplished by plant-specific microtubule enriched organelle called the phragmoplast (red).

How do higher plants select their appropriate division plane? How does the machinery depositing cell plate components form and work dynamically? These developmental questions are vital to our understanding as plant development and morphology relies on the accurate

insertion of the rigid cell walls. Once cell walls are formed, cells are spatially locked in the tissues. This chapter addresses these questions in a concise manner.

2.1. Division plane selection and the preprophase band

How plants select their division plane has been a question that has been lingering around for centuries. Over the years people have demonstrated and suggested mechanisms that can dictate the division plane. However, these mechanisms vary based on cell geometry, internal or external stimuli such as mechanical stress or polarity cues, location of the cell within tissues, and the developmental stage [60, 76–80].

Considering a simple geometric shaped cell, one of the earliest and prominent hypothesis has been that the shortest path length dictates the division axis. This short-axis rule defines the division plane as the minimal-area axis [76, 77, 81]. Recent studies utilizing mathematical modelling and computer simulations support this short-axis rule, albeit for simple shapes or isolated cells. Another school supported by simulation and models suggests the division axis can be faithfully predicted along the maximum-tension axis of the cell [81]. However in both cases, how cells sense their own shape, area, or tension is not understood so far. Both of these theories rely upon the underlying cytoskeletal, which is amenable to quick rearrangements. Cortical microtubules are the favourite candidates as they can sense stress and alter their dynamics. One recent study utilizing computer simulations in *Arabidopsis thaliana* embryo established an intricate dependency between cortical microtubules, cell shape, polarizing cues, and cell division plane positioning [80]. Hence, the cell division plane determination may not be governed by one universal factor but relies upon various inputs that eventually trigger the cytoskeleton.

The division plane in higher plants can be faithfully predicted by the preprophase band (PPB) (Figure 2.2). The PPB forms during the gap2-mitotic (G2/M) phase transition, following the cortical microtubule reorganisation. The TTP signalling module—[TONNEAU1-(TON1), TONNEAU1 RECRUITING MOTIF (TRM), PROTEIN PHOSPHATASE 2A]—including heterotrimeric protein phosphatase (PP2A) complex, is a key player in cortical microtubule reorganisation and PPB assembly [82–84]. The preprophase band consists of ring-shaped parallel bundles of microtubules and filamentous actin localized right under the plasma membrane. This cortical site is called the division site, where the cell plate will fuse during cytokinesis (Figure 2.2) [84]. Over the years, many proteins have been discovered that localize at the division site throughout mitosis and cytokinesis [60, 85–89]. Interestingly, the PPB is transient in nature, i.e it disassembles upon prophase exit (Figure 2.2). These observations and mutant analysis of division site residents in different plants have prompted researchers to believe that PPB is the establisher of the division site in plants. Recently, characterization of a triple mutant in *Arabidopsis*, TRM6, TRM7, and TRM8 resulted in plant cells with a regular organized cortical microtubular array but were lacking the PPBs [90]. Surprisingly, the division plane orientation was on average unaltered although a bit more variable. This study has questioned the widely accepted role of the PPB as the organizer. Such uncoupling of the PPB from interphase cortical microtubule dynamics has also opened a new inquest to understand if the division site is established in an independent and exclusive manner or via a refined model of the PPB’s contribution to the division site establishment process.

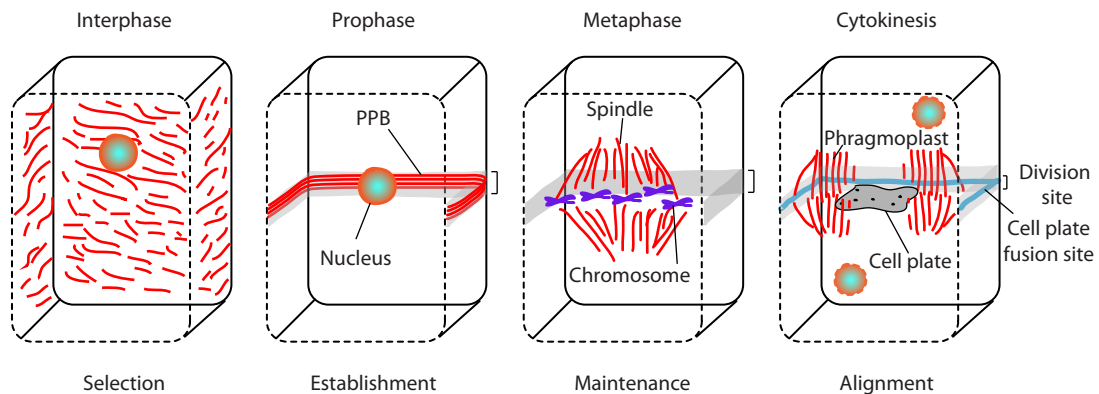


Figure 2.2.: Overview of the plant cell division cycle with focus on the division site. The rear halves of plant cells are shown from interphase till the cytokinesis in a pseudo 3D rendering. The cell wall/outline is represented in black and is solid in the back plane and dashed towards the lateral and front for visibility purposes. The cortical microtubules (red) undergo reorganisation during interphase thus initiating the selection phase for the division site. During this time the cell's nucleus is also centred. PPB forms during late G2/M phase. During prophase, the PPB (shown in red) is distinctly visible at the cortex. The plasma membrane region, under which the PPB forms, is called the division site and is depicted in grey. This stage marks the appropriate establishment of the division site. The width of the division site is marked by a bracket outside the cell. Following the establishment of the division site, the PPB is disassembled and chromosomes (purple) are split with the mitotic spindle (red). This phase is referred to as maintenance of the division site as the molecular memory persists despite PPB disassembly. Ultimately, the cell plate (grey) is oriented with the expanding phragmoplast (red) towards the division site. During late cytokinesis, the width of the division site is reduced and is referred to as cell plate fusion site (cyan). The figure is adapted from [60]

2.2. Division site and the molecular memory

Irrespective of PPBs role, its transient presence at the division site holds a spatial relationship with the division site. Such spatial relationship can be viewed as defining, refining, or reinforcing the molecular memory at the division site that persists till the end of cytokinesis and paves the way for accurate cell plate insertion by the phragmoplast.

As mentioned in the previous section, many proteins have been discovered that decorate the division site. The founding member of the division site is TANGLED (ATN), a microtubule-binding protein found in maize [85]. The localization of tangled in *Arabidopsis* and maize is ring-shaped, similar to the PPB, but persists throughout the mitosis and cytokinesis. Post-cytokinesis, ATN mutants have misoriented cell walls [85]. Phragmoplast orienting kinesin 1 (POK1) and phragmoplast orienting kinesin 2 (POK2) are kinesin-12 class members that also localize at the division site in a similar manner to ATN [91, 92]. Interestingly, POK1 and POK2 act redundantly at the division site as the simultaneous disruption in *pok1 pok2* double mutants show abnormal cell wall positioning and misaligned phragmoplasts. Ran GTPase-Activating Protein 1 (Ran GAP1) is another protein that dis-

plays a similar localisation pattern and phenotype upon disruption [89]. Interestingly, POK1 and POK2 maintain the presence of ATN and Ran GAP1 at the division site, as impairment of *pok1 and pok2* leads to loss of both ATN and RanGAP1 after preprophase band disassembly. However, the accumulation of POKs, ATN, and RanGAP1 at the division site is independent of each other. Two pleckstrin homology (PH) domains on their N-terminus are interactors of POK1. They are localized at the plasma membrane during interphase and from metaphase onwards home at the division site [86]. These PHGAP1 and PHGAP2 also hold a certain connection with POKs as the PHGAP localisation rings are misaligned in *pok1 pok2* double mutants. Apart from this POK network, KCBP, a kinesin-14 member, is also localized at the division site throughout mitosis and cytokinesis [88]. KCBP contains Myo-FERM domain, by which KCBP directly interacts with the lipids and thereby is anchored at the division site. Recently, MAP65-4 has been also shown to persistently localize at the division site [93].

There are also myosin members such as Myosin VIII and Myosin XI shown to be present at the division site in moss *Physcomitrella patens* and *Arabidopsis*, respectively [94, 95]. This indicates the involvement of actin at the division site. Indeed F-actin is a component of the preprophase band, yet microtubules serve as a robust readout for the PPB. It is accepted that upon PPB disassembly, the division site is depleted of actin and therefore, the division site is sometimes referred to as 'actin-depleted zone' [96]. There are pharmacological studies that support this notion of an actin-depleted zone, although in different cell types [60, 96]. This actin-depleted zone is presumed to serve as a negative memory at the division site, but direct proof of the division site being deprived of actin is not yet established [96].

It is definitely intriguing if this plethora of molecules at the division site serves as a spatial memory for future cell plate insertion or if they dynamically guide the phragmoplast.

2.3. Phragmoplast and the kinesin-12 family

To fulfil the specialized cytokinetic demands, plants have evolved a unique and dynamic structure called the phragmoplast (Figure 2.3)[97]. The phragmoplast derives from the remnants of the mitotic spindle located between the daughter nuclei in late anaphase/early telophase [97, 98]. It consists of endoplasmic reticulum, filamentous actin, and a bipolar microtubular array arranged perpendicular to the division plane. The growing end (plus-end) of the microtubules faces the division plane and defines the proximal phragmoplast midzone while the nucleating end (minus-end) faces away from the division plane and is referred to as the distal phragmoplast zone (Figure 2.3). The microtubules and actin filaments serve as tracks for the transport of Golgi/trans-Golgi derived vesicles loaded with cell plate/wall material. This vesicular transport is towards the phragmoplast midzone and is mediated by motor proteins such as kinesins and myosins. When these vesicles arrive in the division plane, they fuse together to progressively form a membranous cell plate (Figure 2.3). The continuous formation and expansion of the cell plate is primarily fuelled by tubulin turnover. Therefore, the dynamics of microtubule turnover is regulated in such a way that the outward expanding phragmoplast guides the centrifugally growing membranous cell plate [99]. The outward polymerizing microtubules serve as tracks for the supply of new cell wall material and are called the leading zone (Figure 2.3). Inwards, microtubules depolymerize continuously making way for the membranous cell plate. This region is referred as lagging zone

[99].

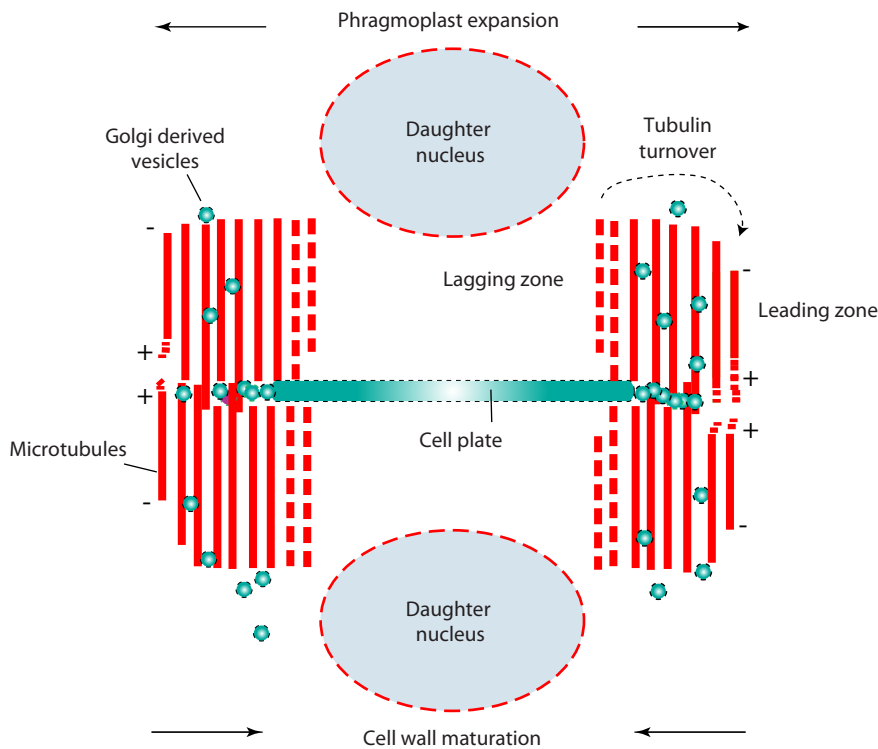


Figure 2.3.: Cross-section of the phragmoplast structure and cell wall synthesis. The phragmoplast is composed of a bipolar microtubular array (red) with microtubule plus-ends facing each other in the equatorial plane. Here, microtubules partially overlap. The phragmoplast initially starts as a donought where microtubules serve tracks for Golgi-derived vesicles (green with dashed black outline). The vesicles fuse together in the equatorial plane to form the cell plate (green). The phragmoplast expands centrifugally towards the cell cortex by virtue of the tubulin heterodimer turnover, as microtubules on the inner side depolymerizes (lagging zone). This process derives polymerization of new microtubules on the outer side (leading zone). The cell plate (green) develops and expands simultaneously with the phragmoplast. The direction of phragmoplast expansion (top) and cell wall maturation (bottom) is shown by the arrows. The daughter nuclei are marked in grey-blue with a red dashed outline. The figure is adapted from [98]

The phragmoplast expansion linked to tubulin turnover relies upon intricately coordinated microtubule nucleation, dynamic instability, and other stabilizing and destabilizing factors [97]. γ -TURC complexes have been shown to nucleate on the existing microtubules [100, 101]. Once polymerized, the new microtubules are transported by the concerted action of kinesin-14 motors towards the microtubule minus-ends to maintain the constant length of the phragmoplast [102, 103]. The phragmoplast width is governed by the extent of midzone. The midzone serves as the meeting point of vesicles and anti-parallel microtubule ends. There are microtubule crosslinking proteins such as MAP65-1, MAP65-2, MAP65-3, MAP65-4 in *Arabidopsis* that create a strong structural scaffold for proper vesicle release and fusion [60, 93, 104, 105]. Complementary, there are motor proteins such kinesin-4 in *P. patens* that restrict the extent of this overlap to optimize cell wall thickness [106].

Most of our knowledge about the phragmoplast and its expansion stems from its struc-

tural organisation and vesicular trafficking pathways. How the phragmoplast is accurately guided for cell plate fusion at the predestined site remains elusive. What is the molecular mechanism that facilitates the attachment of phragmoplast microtubules and cell plate with the parental cell membrane is still unclear. Recent studies from our collaborator, Dr. Sabine Müller, provide vital information into these questions. Dr. Müller's group has reported that peripheral microtubules emanate from the phragmoplast leading edge and reach out towards the division site [91]. Although the division site maintains an actin-depleted zone throughout mitosis, there have been propositions of actin in that region during late cytokinesis [94, 95]. Such observations advance the molecular underpinnings of phragmoplast guidance.

Among the motors, the kinesin-12 family in *Arabidopsis* is a key player during cytokinesis. Generally, kinesin-12 family members in animal kingdom play key roles during cell division. Humans have one kinesin-12 called hKIF15 that is partially redundant with tetrameric kinesin-5 Eg-5. hKif15 is required to maintain spindle bipolarity by assisting the formation of parallel microtubule bundles [12, 13]. Interestingly, *Arabidopsis* has an extended kinesin-12 family with six members [107]. Two of these members Kinesin-12A/PAKRP1 and Kinesin12-B/PAKRP1L are involved in vesicular trafficking in the male gametophyte and localize at the antiparallel-ends of the microtubules [108]. This phragmoplast midzone localisation is MAP65-3 dependent [104]. POK1 and POK2 are shown to localize at the division site and are key components in redundantly maintaining the molecular memory in this region [91, 92]. A recent study shows that apart from the division site, POK2 also localize at the phragmoplast midzone. At the midzone, POK2 interact with MAP-63 via two distinct domains and might provide structural stability to the expanding phragmoplast [92]. Both POK1 and POK2 are enormous in size with POK2 being the largest kinesin known so far [87]. The remaining kinesin-12 motors—Kinesin-12 E/POK-like and Kinesin-F—have been uncharacterised so far. Why the kinesin-12 family has expanded in higher plants is an intriguing question.

2.4. Evolution of cell division in plants

Higher plants have developed remarkable cytoskeletal structures to assist cell division. It is exciting how few of the cytoskeleton-based molecular motor families have also diversified compared to animals and basal plant lineages [107, 109]. Quite striking, for example, is the absence of dyneins in land plants [60]. Instead there is quite an expansion of the minus-end-directed kinesin-14 family, presumably co-evolved with the specialized cytokinetic demands. Moreover, higher plants have also lost centrosomes, one of the cytoskeletal organizing and signalling hubs [110].

Tracing back these meticulous structures such as the preprophase band and phragmoplast to basal plant lineages, it turns out they were devoid of them (Figure 2.4). The early ancestors of land plants commonly referred to as **Streptophytes** algae, divided cells by virtue of centripetal cleavage (evident in *Klebsormidium*, *Chlorokybus*, and *Mesostigma*) (Figure 2.4) [110]. They also formed spindles using centrosomes, very much like animal systems. Following the current phylogenetic tree available, Charophyceae—derived algae—first had a phragmoplast, however, subsequently phragmoplast was found to be operating along with cleavage for cytokinesis (Zygnematophyceae). After such initial elimination generations, the phragmoplast structure seems to have evolve as a striking features in all land plants. Thus,

the phragmoplast mediated cytokinetic mechanisms arose from the last common ancestor of land plants most likely via cycles of adaptive evolution.

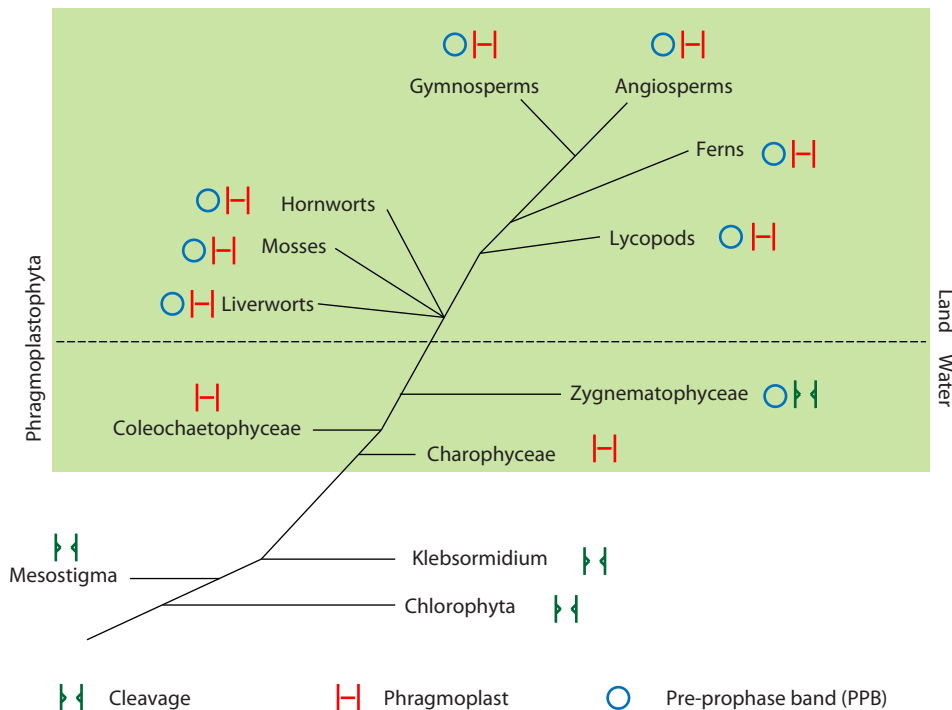


Figure 2.4.: Phylogenetic tree of the cell division. Phylogenetic tree representing the evolution of higher land plants from Streptophyte algae—common ancestors of land plants. The green box depicts phragmoplastophyta and the dashed line in the box marks the water-land transition. This diagram describes how Streptophytes including *Chlorophyta* and *Mesostigma* utilized cleavage (green H) to Chara and other land plants utilizing the phragmoplast (red H) to achieve cytokinesis. Some Zygnematophytes show both cytokinetic mechanisms. The tree also depicts the origin of the preprophase band (PPB, blue rings) that is evolutionary almost confined to the land plants. The figure has been adapted from [110]

Intriguingly, also the preprophase band, believed to be the hallmark of land plant cytokinesis, also has resembling structures in Streptophytes [60]. Some genus in Zygnematophyceae and Charophyceae display ring-like cortical microtubular arrays reminiscent of the preprophase band. However, its appearance seems to be coinciding with the loss of centrosomes or organizers in the cells. There are many studies that suggest a correlation of PPB appearance with appropriate division plane selection in complex plant cell shapes and 3D growth [110–112]. Recently, the accepted view of the PPBs function at the division site was challenged [90].

Nevertheless, the simultaneous (or co-) evolution and integration of the PPB and the phragmoplast in land plant cell division raises the question if the associated cytoskeletal proteins adapted or co-evolved. The absence and diversification of kinesin and myosin families might correlate with the development of these complex microtubule-based structures.

3. The power of reconstituted assays in cell biology

Over the centuries, cell biologists have been inquisitive about the principles and molecular mechanisms that define a physically functional cell—from its shape and size to organisation of individual molecules and organelles, to gene expression, to translation, to motility, and to its own deconstruction. The idea of creating a cellular phenomenon outside the cell from its purified components, in simpler isolated conditions, has been an audacious vision. The discovery of cargo transport in squid neurons and actin-myosin based force generation are impeccable examples enriching our fundamental knowledge [34, 66]. Ever since Hooke’s and Leeuwenhoek’s work on cells using first optical microscopes, biologists have embraced and continued to develop and employ the state-of-the-art technologies [113]. The advent of X-ray crystallography [114], electron microscopy [115], fluorescence proteins [116], fluorescence microscopy [117], recombinant DNA technology [118], optical tweezers [119], precisely computer-controlled electronic devices, stable temperature controllers, and microfluidics [120] have pushed the barriers to understanding cellular events.

The purification of cellular components assembled *in vitro*—Latin meaning within the glass—offers a less crowded environment and more focussed attention to the molecules of interest. Bulk measurements have thrived mainly in biochemistry and have provided average information about a molecule or process, for example, binding-unbinding kinetics of two purified proteins. Bulk measurements are also robust due to the proportional relationship between measured signals and number of molecules in the reaction (often large). The last 50 years have downsized these problems to individual molecules and revolutionized the field of single-molecule biology. It offers a fantastic advantage, i.e. enables understanding the properties of individual molecules that might be different or over/under estimated in ensemble measurements. Most of our understanding of how cellular machines work is courtesy of single-molecule investigations. Although such techniques have penetrated to all the research areas mentioned in the previous paragraph, its contribution to the field of cytoskeletal biophysics is vast.

The ability to purify actin and tubulin from the brain of animals, assemble them *in vitro* and monitor them in real-time, has enabled detailed comprehension of filament assembly and dynamics. Moreover, these assembled filaments can be used as tracks and quantify how molecular machines work in the cell. One prominent example is that of how a kinesin motor walks and delivers cargo in cells. Studies have been able to measure and quantify single-steps, speed, walking distance, binding and unbinding kinetics, ATP dependence of stepping, and force exerted by individual kinesin molecules [36, 59, 121]. Moreover, using recombinant technology researchers have identified single as well as stretches of amino acids that ultimately confer and affect motility. These techniques can provide enormous data about full probability distributions, fluctuations, intermediate states, and different populations of the molecule. These data have been corroborated with more measurements to understand the

exact gait of a kinesin molecule [44, 122]. To mimic the cell systems further, studies have reconstituted these assays to understand how individual kinesins coordinate with each other while delivering a cargo and measure forces on them [123]. Together, such *in vitro* reconstituted systems can help understanding the behaviour of cellular components that can not be fully comprehended from *in vivo*—within the living—localisation studies alone. Therefore, an ideal and profound way to investigate a cellular phenomenon is to complement information from single-molecule *in vitro* assays with *in vivo* localisation data that is amenable to manipulation.

4. Aim of this work

The objective of this thesis is to functionally characterize two members of the kinesin-12 family and their molecular role during cytokinesis in *Arabidopsis thaliana*. These two members are phragmoplast orienting kinesin 1 and 2 (POK1 and POK2). POKs have been shown to be recruited at the division site early in mitosis overlapping with the preprophase band. POKs redundantly maintain at least two other positive markers—ATN and Rho GAP1—of the division site until the end of cytokinesis. Thus, POKs serve as components of molecular memory at the division site. *pok1 pok2* mutant analyses display plants with severe cellular defects. The cell walls are dramatically misaligned. Furthermore, phragmoplasts are titled en route expansion process. These observations suggest that POKs might serve more than a static memory scaffold at the division site. One logical and strong hypothesis is their key role in properly guiding the expanding phragmoplast to the division site. In particular, the phragmoplast guidance might be executed by POKs interaction with the peripheral microtubules emanating from the phragmoplast leading edge. This thesis is an investigation towards this hypothesis using state-of-the-art single-molecule assays reconstituted *in vitro*. The first goal is to express and purify these two POK proteins fused with a fluorescent tag. The second goal is to assemble a cell-free system from purified proteins, to decipher the activity and to characterize these microtubule-associated motors. Total internal reflection fluorescence microscopy (TIRF-M) and optical tweezers are used to achieve the second goal. The experiments will enable to understand the molecular behaviour of single POK motors on the microtubule lattice and how much force they exert on microtubules. The ultimate intent of this project is to complement these *in vitro* findings with *in vivo* localisation experiments, wherever possible, to propose a molecular mechanism underlying POK1 and POK2 mediated accurate cell plate insertion during cytokinesis.

Part II.

Methods

5. The genes: construct designing and preparation

5.1. Whole RNA isolation

To extract RNA/DNA from the mitotic cells, young whole plants (*Arabidopsis col-0*), young leaves, and floral parts were pluck using sterile forceps. These tissues have a high mitotic index. The plant tissue was put in a 1.5 ml eppendorf tube, weighed and snap-frozen in the liquid nitrogen.

RNA isolation was done using RNeasy Plant Mini Kit (Qiagen, 74904). The grinding method of tissue lysis was used. *It is important to clean the work space and use sterile eppendorf tubes, tips, pipettes, and pestle and mortar before beginning the procedure as RNA is easily degradable. During the procedure, all the tubes, pestle and mortar were pre-cooled using liquid nitrogen to prevent any heat generation during grinding. Heat would thaw the tissue that will cause its loss and RNA degradation. Pipetting was done on ice and gloves were changed frequently throughout the protocol.* The pestle and mortar were cleaned with 0.2 M NaOH, rinsed with deionised water (Milli-Q water with resistivity 18.2 MΩcm), ethanol and water in the same order. After cleaning, pestle and mortar were autoclaved and baked overnight at 160 °C. 100 mg of plant tissue was used in each round as it was recommended by the kit. The tissue was grinded using pre-cooled pestle and mortar and transferred to a pre-cooled 1.5 ml eppendorf tube. Following tissue lysis, the exact protocol from the kit was followed except the RNA in the final step was eluted in sterile-filtered RNase free water. The concentration of the RNA was measured using nanodrop (ND-1000 spectrophotometer, peqlab; from now onwards referred as nanodrop). RNA was stored at -80 °C.

Alternatively, the plant tissue can be lysed using a tissue lyser machine with RNAase free beads.

5.2. Whole genomic DNA isolation

The plant tissue was lysed as mentioned in the above section. 100 mg of plant tissue was used. The grinded plant tissue was resuspended in 65 °C pre-heated extraction buffer (1 % RNAase H, 0.2 M Tris/HCl pH 7.5, 0.25 M NaCl, 25 mM EDTA and 0.5 % SDS). It was incubated for 30 min at 65 °C with 1000 rpm on a thermomixer. Afterwards, it was mixed with 500 µl of pure chloroform and vortexed thoroughly until homogenization. Subsequently, it was centrifuged for 5 min at 13,000 rpm. After centrifugation, there was a phase separation in the liquids. The top layer containing the DNA was poured into a new sterile tube, while the pellet containing cell debris and protein was discarded. The DNA was mixed with 1 ml of 100 % isopropanol and inverted a few times by hand. It was then centrifuged for 5 min at 13,000 rpm and the DNA-pellet was resuspended in 1 ml of 70 % ethanol. It was centrifuged

again for 5 min at 13,000 rpm and the pellet was dried at the room temperature. Finally, the DNA pellet was resuspended in 100 μ l of sterile-filtered water. DNA concentration was measured using the nanodrop. DNA was stored at -20°C .

5.3. Complementary DNA or cDNA synthesis

All the incubation steps during cDNA synthesis were carried out in a polymerase chain reaction (PCR) machine and using a PCR tube. All pipetting and rest of incubation steps were carried out on ice. Before cDNA synthesis, the RNA was subjected to DNase treatment using DNase I (Invitrogen, Amplification Grade, 18068015). A 10 μ l reaction was set up that consisted of 2 μ g of RNA, 1 \times DNase reaction buffer, 5U DNase I and nuclease free DEPC treated water. The reaction was incubated at 37°C for 30 min. To inactivate the reaction, 1 μ l of 25 mM EDTA was added and incubated at 65°C for 10 min. The cDNA synthesis was carried out using Superscript IV Reverse Transcription Kit (Invitrogen, 18091050). cDNA synthesis can be done using a gene specific primer or a random hexamer or an oligo dT primer depending on the purpose. Here, two parallel reactions were used one using a gene specific primer (preferably reverse primer) and a random hexamer. To the DNase-treated reaction tube with 11 μ l reaction volume, 1 μ l of 10 μ M desired primer and 1 μ l of 10 mM dNTP mix were added. The reaction was then incubated at 65°C for 5 min. It was then quick chilled on ice for 5 min. After a brief centrifugation, 4 μ l of 5 \times first strand buffer and 2 μ l of 0.1 M DTT, 1 μ l of RNase inhibitor were added and gently mixed by pipetting. The reaction was then incubated for 2 min at 42°C for gene specific primer and 2 min at 25°C for the random hexamer. Afterwards, 1 μ l or 200 U of Superscript IV RT was added, gently mixed and then incubated at 42°C for 50–60 min. The reaction was inactivated by incubation at 70°C for 15 min. In the end, the synthesized cDNA was treated with RNase H and addition of 1 μ l/2 U RNase H and incubation at 37°C for 20 min. The cDNA was stored at -20°C .

5.4. Agarose gel electrophoresis

1% agarose (Carl Roth, 3810.3) in TAE buffer (40 mM Tris, 40 mM acetate, 1 mM EDTA) was used throughout the thesis. A standard 1 Kb DNA ladder was used (Thermo Scientific, SM0311 or New England BioLabs, N0552L). Gels were run at 100 mV until the loading/tracking dye (6 \times TriTrack, Thermo Scientific, R1161) indicated the desired run. To visualize the DNA, Ethidium bromide was added to the gel (0.5 μ g/ml final concentration) during casting before it solidifies. The gel stained photos were taken by a gel-doc system from Peqlab using auto-exposure function.

5.5. Polymerase chain reaction (PCR)

Three types of PCR reactions were used in this thesis primarily depending on the DNA polymerase used. Phusion polymerase (Thermo Scientific, F520S), Prime Star GXL (Takara, R050A) and in-house purified taq (obtained from Prof. Gerd Jürgens lab, ZMBP), referred in the text as home-made taq. The Phusion PCR reaction consisted of 1 \times High Fidelity buffer,

250 μ M dNTPs, 0.2 μ M forward and reverse primer each, few ng (2–10 ng) of template DNA, 0.4 U Phusion polymerase filled up to 20 μ l with deionized water. The Prime Star reaction was consisted of 1 \times GXL buffer, 200 μ M dNTPs, 0.2 μ M forward and reverse primer each, few ng (2–10 ng) of DNA or about 200 μ g cDNA and 1.25 U polymerase. The reaction mix was filled up with deionized water up to a final volume of 50 μ l. The primer annealing temperature was set to 55 $^{\circ}$ C for all reactions with melting temperature below 60 $^{\circ}$ C. The home-made taq reactions consisted of 1 \times Taq buffer (also home-made), 4 mM dNTPs, 0.5 μ M forward and reverse primers each, 0.3 μ l taq, filled up to 20 μ l with deionized water. In case of colony PCR, an individual bacterial colony was picked using 200 μ l tip and used as a DNA template. *PCRs for most of the constructs were done using the Phusion polymerase. Amplification reactions for the POK2C terminus, POK2 full-length cloning, and Tangled (ATN) were done using Prime Star polymerase. Other standard amplification reactions that do not require proof reading were done using home-made taq.* The list of all primers used during cloning are provided in the appendix. The annealing temperature of the primer pair was calculated using the web calculator of ThermoFisher and occasionally reconfirmed using Northwestern University web calculator [124, 125].

5.6. DNA purification—gel extraction and PCR clean-up

After visualizing the DNA bands on the agarose gel, if needed, the desired DNA band was sliced under short exposure of UV light. The gel piece was weighed and if not used right away, was stored at -20° C. To extract the DNA, QIAquick gel extraction kit (Qiagen, 28706) was used. The exact protocol was used except the elution in the final step was carried out in 55 $^{\circ}$ C heated sterile filtered water. To remove enzymes and other proteins in the DNA samples, the Qiagen PCR clean up kit (Qiagen, 28106) was used. The exact same protocol was followed except the elution was done in 55 $^{\circ}$ C warm sterile filtered deionized water. The concentration of the DNA was measured using the nanodrop after each preparation. The DNA was stored at -20° C.

5.7. Restriction digestion and ligation

The desired digestion of PCR amplified fragments and the vector backbone was conducted in accordance with the restriction enzymes used. All the digestion reactions in this thesis were carried out by enzymes from Thermo Scientific. Restriction enzymes work in specific buffers and in case double digestion was carried out, the buffer compatibility was checked using Double Digest Calculator from Thermo Scientific [126]. The main restriction digestion reaction in this thesis relies on two sites AscI/SgsI (FD1894) and NotI (FD0593). The reaction conditions for this double digest consisted of upto 2 μ g DNA, 1 \times fast digest buffer, 1 μ l of each enzyme per 1 μ g of DNA, filled upto 20 μ l with sterile water and incubated for 30 min at 37 $^{\circ}$ C. The reaction was inactivated at 80 $^{\circ}$ C for 10 min. Before ligation, the vector was treated with FastAP Alkaline Phosphatase (Thermo Scientific, EF0654) to prevent auto-ligation of the backbone by dephosphorylation. The dephosphorylation reaction mix contained 1 μ g of digested vector, 1 \times AP reaction buffer, 1 U FastAP phosphatase. It was incubated on 37 $^{\circ}$ C for 10 min and then inactivated at 75 $^{\circ}$ C for 5 min. The ligation reaction

was carried out using the Quick ligation kit (New England BioLabs, M2200). The ratio of the vector and insert was 1:4 or 1:5. The corresponding molar weights were calculated by the NEB online calculator [127]. In experience, 100 ng of the vector with calculated insert weight gave good results. The ligation reaction was set up on ice and consisted of 10 μ l of Quick Ligase Buffer, desired DNA concentrations of vector and insert, filled up to 20 μ l with sterile water. Finally, 1 μ l of Quick Ligase was added and the reaction was incubated in a PCR machine for 30 min at 25 °C. The reaction was inactivated by cold incubation on ice for 5 min. 5 μ l of this reaction was used directly for bacterial transformation. The rest of the ligation reaction was kept at 4 °C for a couple of days in case the transformation did not work.

5.8. Chemically competent cell preparation

50 ml of desired bacterial strain was inoculated overnight in Luria Bertini (LB) media without antibiotics in a 250 ml Erlenmeyer flask with baffles on 37 °C with shaking. The optical density at wavelength of 600 nm (OD600) was measured in the morning of the next day using a cuvette and standard UV-VIS spectrophotometer or a cuvette compatible nanodrop. The OD600 is generally more than 1. 500 μ l of this grown culture was inoculated in 50 ml of fresh LB media to subculture. The culture was grown at 37 °C with shaking and the OD600 was measured every 2 h to reach a desired OD600 of 0.4–0.6. After the culture reached the desired OD range, it was cooled on ice for 15 min in the cold room. The culture was transferred into 50 ml sterile and pre-chilled falcon tubes and centrifuged at 3000 rpm at 4 °C. All subsequent steps were carried out in the cold room. After centrifugation, the supernatant was discarded and the cell pellet was resuspended in 5 ml of 3 mM pre-chilled calcium chloride (CaCl₂) solution. *Cells were slightly vortexed at this stage but were not pipette mixed.* These cells were then incubated on ice for 20 min. The resuspended pellets were then distributed in 1.5 ml pre-chilled and sterile centrifuge tubes and centrifuged for 10 min at 3000 rpm at 4 °C. The supernatant was discarded and pellets were finally resuspended into 30 mM pre-chilled CaCl₂ solution supplemented with 30% glycerol. The final solution was distributed into 1.5 ml pre-chilled and sterile centrifuge tubes as 100 μ l aliquots, eventually snap frozen in liquid nitrogen and stored at –80 °C.

5.9. Bacterial transformation using chemically competent cells

Competent cell aliquots were taken out of –80 °C and thawed on ice for about 20–25 min. Desired amount of DNA (preferably few nanograms) was carefully added to the tube without mixing it further with a pipette. The tube was gently flicked 4–5 times and was incubated on ice for 30 min. Afterwards, cells were given a heat shock at 42 °C (using a pre-set thermomixer or water bath) for exactly 1 min. For commercial competent cells (NEB, Invitrogen) the time was reduced to 40 s. After the heat shock, cells were incubated back on ice for 10 min. Subsequently, 950 μ l of LB media was added to the competent cells and they were incubated at 37 °C with shaking for 60 min. 50–100 μ l of this culture was plated onto bacterial plates with desired antibiotic resistance using autoclaved glass pearls (Carl Roth, A556.1) and

incubated overnight at 37 °C or in some cases at 30 °C.

In this thesis, various competent cells were used depending on the purpose. The transformation of original pOCC8 vector was done in ccdB resistant bacteria (Thermo Scientific, A10460) that have the presence of ccdB cassette. The transformation of most of the other constructs POK₂₁₋₅₈₉, POK₁₁₋₅₆₄, POK₂₁₈₃₋₅₈₉, POK₁₁₋₅₈₉, POK₂₂₀₈₁₋₂₇₇₁, and ATN was carried out in NEB high efficiency (NEB, C2987H), NEB stable (NEB, C3040H), NEB 10 Beta (NEB, C3019H), Top 10 (Thermo Scientific, C404003). For POK2 cloning apart from the above mentioned cells— attempts were made using steller competent cells (Takara, 636763) that might reduce recombination problems.

5.10. Luria Bertini (LB) media for bacterial growth

Composite LB media (premixed Tryptone, NaCl and yeast extract, Carl Roth, X968.1) was used as liquid and solid media. 25 g of the composite media was put into 1 l of distilled water in a Schott bottle and autoclaved for 20 min to use as liquid media. For solid media, along with composite media, 20 g of Agar (Sigma, A7002) was added into 1 l of distilled water and autoclaved. After autoclaving the media was stored at the room temperature. For sensitive experiments, pH was also monitored and adjusted to 7.0 with NaOH. For the preparation of bacterial plates, sterile media with agar was put into the microwave for a few min until all agar was dissolved. The media was cooled down in a laminar flow hood. The antibiotic (Ampicilin 100 μ g/ml final, Sigma, A0166) was added when the media was considerably cooled down but not solidified. The plates were stored in the cold room or at 4 °C and were good for about 6 months.

5.11. Plasmid preparation Mini and Midi

For isolating plasmid DNA from the desired bacterial colonies, Qiagen kits were used. For the Mini-kit (12125) and Midi-kit (12145), the procedure was followed as suggested, except the final step, where DNA was eluted in sterile-filtered water that was heated up to 50 °C.

6. The proteins: expression and purification of proteins

6.1. Protein expression using SF9 insect cells

After cloning the desired gene of interest in the destination expression vector (in this thesis pOCC8), it was sent to MPI-CBG, Dresden protein facility for baculovirus production. The destination vector pOCC8 has recombination sites called Lef-2 and ORF1625 that are compatible with the *flashBAC* Oxford Expression Technologies baculovirus system. The bacmid, destination vector pOCC8, and SF9 insect cells were co-transfected and recombination took place in the insect cells. The positive transformants were screened with GFP fluorescence cassette also present in the vector. While the baculovirus production was underway, the insect cell culture was started and continuously monitored and split. After the P2 or titer 2 stock of viruses were received, cells were maintained in 500 ml flasks at a volume of 100 ml and a cell count of 0.5 million cells per ml and infected with 1 ml of baculoviruses. For one expression, four parallel flasks and infections were created and, upon expression, were pooled. The cultures were left untouched for 48 h and then monitored for GFP fluorescence under UV light in the hood and cell health/viability under a light microscope. Finally, cells were harvested between 72–96 h by centrifugation. This period was the recommended window, however, if starting a new culture, a time-course of protein expression should be established. The insect cell cultures were spun down at 3000 g at room temperature and the cell pellets were quickly washed with 1× PBS and re-spun. Finally, the cell pellets were thrown into liquid nitrogen using a 1 ml sterile pipette to create pearls. The pearls were stored at -80°C . Ideally, they should be stored in the vapour phase of liquid nitrogen or at -140°C .

6.2. Protein purification

Proteins were purified via sequential chromatography. Cation exchange chromatography (HiTrap SP HP 1 ml, GE Healthcare) followed by desalting (HiTrap desalting 1 ml, GE Healthcare) and subsequently affinity chromatography (HisTrap HP 1 ml, GE Healthcare) was performed. Cells were thawed on 37°C in a water bath and lysed in 50 mM HEPES, 150 mM NaCl, 5 % glycerol, 0.1 % Tween 20, 1.5 mM MgCl_2 , 3 mM EGTA, 1 mM DTT, 0.5 mM ATP and protease inhibitors, at pH 7.5. The cation wash buffer consisted of 20 mM HEPES, 150 mM NaCl, 5 % glycerol, 1.5 mM MgCl_2 , at pH 7.5. The cation elution buffer consisted of the same composition except the concentration of NaCl (600 mM) at pH 7.5. The desalting column was used to exchange the buffers to proceed towards metal affinity. The metal affinity wash buffer consisted of 50 mM phosphate buffer (pH 7.5), 300 mM NaCl, 10 mM imidazole, 10 % glycerol, 1 mM MgCl_2 , 20 μM ATP, and protease inhibitors at pH 7.5. The metal affinity elution buffer consisted of the same except for the concentration

of imidazole (300 mM) at pH 7.5. Protein stability was confirmed from the SDS-PAGE and western blotting using anti-GFP antibody (mouse, Roche, Cat. 11814460001). The purified protein concentration was determined using a Bradford assay and nanodrop. Finally, the protein aliquots were snap frozen in liquid nitrogen and stored at -80°C . The protein concentrations were measured using a nanodrop. The concentration for the co-localisation experiment was validated with a western blot.

6.3. SDS-PAGE electrophoresis

To monitor the purification, protein fractions were run and analysed on sodium dodecyl sulfate polyacrylamide gels using Mini-PROTEAN TGX gels (Bio-Rad, 456-1094) and a Mini-PROTEAN Tetra Vertical Electrophoresis Cell (Bio-Rad, 1658004). The samples were mixed with $1\times$ protein loading dye (0.2 M Tris HCl, 0.4 M DTT, 0.28 M SDS, 6 mM Bromophenol blue, 32 % glycerol) and denatured at 90°C for 7 min. Afterwards, samples were shortly centrifuged using a table-top centrifuge. The samples were loaded on the gel and run in $1\times$ SDS-running buffer (25 mM Tris, 192 mM glycine, 0.1 % SDS). The gel was run for 15 min at 80 V and 3 A for stacking the proteins. For resolving the protein bands, the gel was run for 1 h at 100 V and 3 A or until the tracking dye reached the gel bottom. A PageRuler Plus Prestained Protein Ladder (Invitrogen, 26619) was used as the marker.

6.4. Coomassie brilliant blue staining

To stain proteins after the electrophoresis, gels were immersed in coomassie staining solution (0.1 % coomassie brilliant blue R-250, 40 % ethanol, 10 % acetic acid) for 30 min. Alternatively, for accelerated results, gels were boiled in a microwave at 800 W for 1 min. Afterwards, the gel was left in distilled water overnight and washed with distilled water the next day, until the desired band intensity was reached.

6.5. Native-PAGE electrophoresis

To analyse the oligomeric state of the proteins in their native state without the influence of denaturing agents, native-PAGE electrophoresis was conducted. 4–16 % Native PAGE Bis-Tris gels (Invitrogen/Thermo Scientific) were used. After loading the desired concentrations of the proteins, the gel was first run at 150 V for 1 h, followed by 200 V for 1 h. NativeMark Unstained protein standard (Thermo Scientific, LC0725) was used as the protein weight reference. Note that native PAGE is not only based on the molecular weight of the protein but also on the charge. After the complete run, the gel was shortly rinsed with water. 100 ml of fix solution (For 500 ml: 200 ml methanol, 250 ml distilled water, 50 ml acetic acid 99.9 %) was added to the gel. Then, it was heated in the microwave for 1 min at 800 W. Afterwards, the gel was incubated at the room temperature with shaking. This fixation step was repeated once again. After decanting the fixative, 100 ml of staining solution (For 500 ml: 0.1 g Serva Blue R coomassie, 150 ml methanol, 300 ml water, 50 ml acetic acid 99.9 %) was added and the gel was heated in the microwave for 1 min at 800 W. This was followed by incubation at the room temperature for 30–60 min with shaking. After decanting the staining

solution, 100 ml of destaining solution (For 500 ml: 460 ml water, 40 ml acetic acid 99.9%) was added to the gel and heated as mentioned above. The gel was then incubated at the room temperature for 15–30 min with shaking. The destaining cycles were repeated roughly 3–4 times until the background was clear.

6.6. Western blotting

Western blotting was done to confirm if the protein bands corresponding to the correct molecular weight on the coomassie stained gels were indeed the desired proteins. The assay relies on antibody-antigen interactions. After the SDS-PAGE gels were finished, instead of treating them for coomassie, they were processed for blotting where proteins in the gel were transferred onto a PDVF membrane. This transfer was achieved by using the Trans-Blot Turbo Transfer System (Bio-Rad, 1704150) equipped with two cassettes. The gels were carefully placed onto the membrane in the Trans-Blot Turbo Mini PVDF Transfer Packs (Bio-Rad, 1704156). All air bubbles were removed using the blot roller. The transfer packs contains the blot sandwich in requisite buffers and instructions for proper transfer. After the blot sandwich was achieved, the proteins were blotted at 2.5 V for 3 min using the 1 Mini TGX in-built selection or sometimes another selection based on the protein weight. After the transfer, the membrane was transferred to a washing box where it was washed quickly with 1× Pierce wash buffer (Thermo Scientific, 37577). Subsequently, the blot was processed for antibody reaction using the Pierce Fast Western Kit, SuperSignal West Pico Mouse (Thermo Scientific, 35060). The blot was immersed in 7 ml of antibody diluent provided in the kit and 3.5 μ l (1:2000 dilution, stock 0.4 mg/ml) of anti-GFP antibody (mouse IgG, Roche, 11814460001) was added. The blot was incubated in the cold room while shaking overnight. To avoid any evaporation, the box was wrapped in a cling-film. Next day, the blot was quickly washed with 1× wash buffer and immersed in 6 ml antibody diluent and 600 μ l of secondary antibody (1:1000 dilution), and incubated at room temperature for 1 h on a shaker. The secondary antibody was an anti-mouse and coupled to horse radish peroxidase that was provided in the kit. After secondary antibody incubation, the blot was washed 4 times with 1× wash buffer for 10 min each. For detection, 1:1 mixture of 3 ml enhancer solution and 3 ml of peroxidase solution was used. The membrane was placed in a clean incubation box and the detection mixture was poured. The blot was incubated for 90 s while being shaken by hand. The blot was transferred onto a clean transparency sheet and chemiluminescence was detected for 5–15 min depending on the signal using the FusionFX7 imaging system (Peqlab).

7. The lens: microscopic techniques and sample preparation

7.1. Optical tweezers

Optical tweezers are sensitive instruments that use lasers to manipulate (*hold, rotate, move, join, separate, stretch etc.*) micro or nano sized dielectric particles at its focus with an ultra-precision, sub-nm resolution. It was invented in 1986 by Arthur Askin at Bell Labs, with the aim to trap and cool single atoms [119]. Immediately after, its powerful applicability was realized by Arthur Ashkin in trapping and manipulating whole cells and organisms such as bacteria and viruses [128]. Since then, optical tweezers have been used to understand fundamental molecular and mechanistic problems in biology beginning with flagella [129], single kinesins [42], myosins [66], dyneins [56], actin [130], microtubules [131], DNA [132], RNA polymerases [133], helicases [134], to more complicated mechanisms such as protein folding [135], DNA packaging by viruses [136], and quite recent CRISPR/Cas9 action [137]. The applications of this instruments are tremendous and are not limited to biology. In 2018, Arthur Ashkin was awarded with the Nobel Prize in Physics for inventing optical tweezers and its application to biological systems.

7.1.1. Working principle

The basic principle of optical tweezers rely on formation of an optical trap by tightly focussing a laser beam with a high numerical aperture (NA) objective lens. When a dielectric particle is present near the focus, it experiences an optical force due to momentum transfer from the scattering of incident photons. *Light carries momentum that is proportional to its energy and in the direction of propagation. Any change in the direction of light caused by reflection or refraction from an object in the path, results in a change of momentum of light. Due to conservation of momentum, the object must also experience an equal and opposite momentum change, thereby giving rise to a force acting on it.* This optical force can be decomposed into two components for convenience and intuitive understanding of the overall force. The first component, the scattering force, as 'Neuman and Block' suggests, can be viewed as a *fire hose* pushing the particle in the direction of light propagation (Figure 7.1) [139]. Although the incident light reaches the particle from one direction, the scattering can take place in a variety of directions and some of the incident light might be absorbed too. Therefore, there is a net momentum transfer from the incident light to the particle (Figure 7.1). This transfer becomes important near the focus of the laser, where there is a steep intensity gradient and thus the second component should be considered. The second component, the gradient force, acts in the direction of the spatial light gradient (Figure 7.1). The gradient force originates because a dipole experiences a force in the direction of the electric field gradient [139]. These

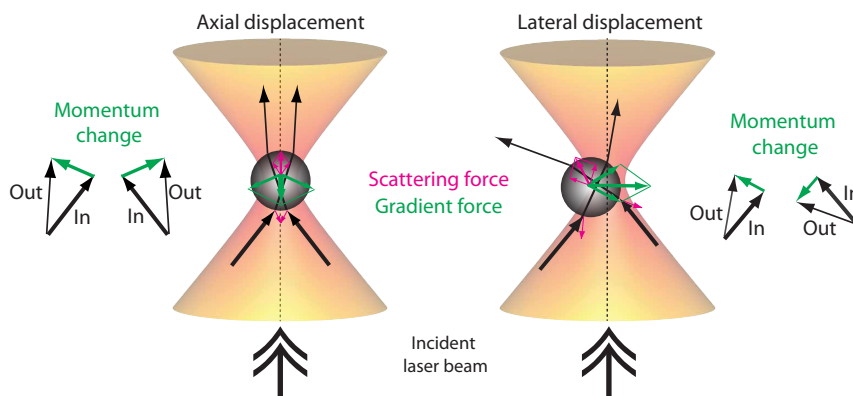


Figure 7.1.: Simplified depiction of forces experienced by a microsphere in an optical trap. When incident light rays hit the microsphere (grey), they undergo refraction and therefore, there is a net change in the momentum of light. Due to conservation of momentum, the microsphere experiences an equal momentum change and in the opposite direction. This momentum change is represented in two cases here. *Left*, a microsphere is displaced axially and *Right*, the bead is displaced laterally. The overall forces can be split in two components: gradient and scattering forces (see Section 7.1.1). The figure is adapted from [138]

dipoles are induced in the dielectric particles by the laser. The gradient force is proportional to the optical intensity gradient as well as the polarizing ability of the particles. For a stable trap, the axial gradient force component pulling the particle towards the focus must exceed the scattering force component that pushes it away. The balancing of these two forces results in an axial equilibrium position where the trapped particle is located a bit away from the focal point. For small displacements (about 150 nm) of the particle from the equilibrium position, the optical trap acts as a *Hookean spring*, where the spring constant or so called trap stiffness is proportional to the laser power. The restoring force is given by $F = \kappa \cdot x$, where x is the displacement from the trap centre.

It is important to note that the size of the trapped particle matters and dictates how the forces should be calculated correctly. When the size of the trapped object α is much larger than the wavelength of light λ , the forces can be calculated from ray optics. When α is much smaller than λ , the conditions for Rayleigh scattering are met and the forces can be computed by approximating the particle as a single dipole. When α is comparable to λ , neither ray optics nor dipole assumptions are valid and the detailed electromagnetic Mie theory might describe the acting forces. Nevertheless, in all cases, over a certain extent the trap behaves as a *Hookean spring* and therefore forces can be deduced from the displacement of the particle.

7.1.2. Design

The basic components of an optical tweezers setup are a trapping laser, a high NA objective lens, beam expansion, and steering optics combined with some means of specimen visualisation such as differential interference contrast (DIC) microscopy. However, precise steering requires lenses, mirrors, and electro/acoustic-tunable devices along with highly sta-

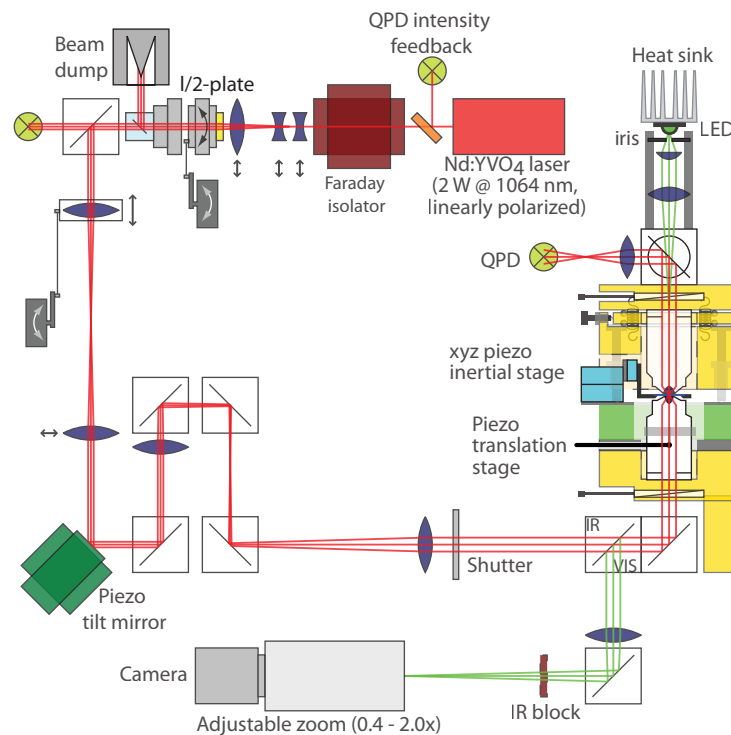


Figure 7.2.: Schematic of the optical tweezers setup. An infrared laser is focussed on the sample that is mounted on the stage (cyan) by passing through a set of lenses and mirrors and eventually a high NA objective. The piezo-tilt mirror (dark green) and piezo translation stage (light green) play a major role in beam steering relative to the sample. The condenser objective collects the light and reflects it onto a QPD. For microscopy, the sample is illuminated by a blue LED (mounted on top of the tower) and imaged by a zoom adjustable CCD camera. The figure has been adapted from [140]

ble infrared lasers for high trap stiffness while causing minimal phototoxicity to biological samples.

In this thesis, a single-beam custom made optical tweezers was used. The setup was constructed by Dr. Mohammed Mahamedeh [140] and is shown in Figure 7.2. The setup is placed in a vibration isolation chamber detached from the foundation of entire building and is equipped with a 5 W infrared laser ($\lambda = 1064 \text{ nm}$) and a milliKelvin-precision temperature control [140]. Together, this set up provides high stability and a high spatial resolution. The temperature feedback is connected to the objective and is continuously maintained at $29.200 \text{ }^\circ\text{C}$. The laser is focused by an oil immersion $100\times/0.7\text{--}1.3 \text{ NA}$ objective from Nikon. The presence of piezo-tilt mirrors allows the lateral movement of the trap, while a piezo-translation stage enables movement of the sample in 3D. The displacements in all axes are detected via a quadrant photodiode (QPD) mounted at the top of the optical tower. The samples are visualised using DIC illuminated by a blue light emitting diode (LED). A CCD camera allows light detection with a maximum frame rate of 26 Hz and pixel size of 50 nm.

7.2. Total internal reflection fluorescence (TIRF) microscopy

TIRF microscopy is a fluorescence based near surface illumination and detection method. This method enables study of molecules and processes at or near the cell surface (Figure 7.3). TIRF has a decreased background signal emanating in the bulk or cytosol, which limits traditional microscopy techniques like epifluorescence and confocal microscopy. Therefore, variety of membrane related protein interactions and membrane proximity cytoskeletal re-organisations have been studied in live cells [141]. TIRF microscopy has been key in the single-molecule fluorescence microscopy where individual behaviour of the molecules has been observed and characterized.

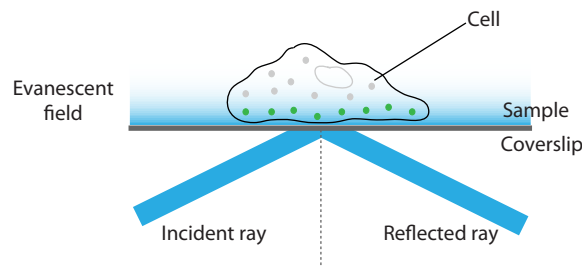


Figure 7.3.: Schematic illustrating TIRF microscopy. When incident rays beyond a critical angle hit the glass-water or coverslip-sample interface, the light rays undergo total internal reflection. This reflection leads to the creation of an evanescent field at the interface with an exponentially decaying intensity. This enables excitation and detection of fluorophores at or near the interface or cell periphery with a higher signal to noise ratio. The figure is adapted from [141].

7.2.1. Working principle

The physics behind TIRF microscopy relies on total internal reflection of light and requires a refractive index mismatch at the interface. When a light ray leaves the objective lens, it passes through a matching refractive index zone created by the immersion oil and glass surface (refractive index of both $n_2 = 1.51$). This incident light ray reaches the glass-water interface (refractive index $n_1 = 1.33$) and undergoes refraction according to Snell's law. When the angle of incidence θ_i , is more than a critical angle θ_c , light rays reflect back in the glass-oil medium and, therefore, do not propagate in the sample. The critical angle can be computed as

$$\theta_c = \sin^{-1}(n_1/n_2), \quad (7.1)$$

This phenomenon is called total internal reflection (TIR). During TIR, a standing wave known as evanescent field is created. This field illuminates the sample (Figure 7.3). The strength of the evanescent field given by the intensity I decays exponentially from the interface to a distance z in the aqueous medium. This relation is expressed as follow:

$$I = I_0^{-z/d}, \quad (7.2)$$

where I_0 is the intensity of the field at $z = 0$. The distance d termed as depth of the field is usually up to 100–150 nm from the surface and depends on the incident angle, wavelength

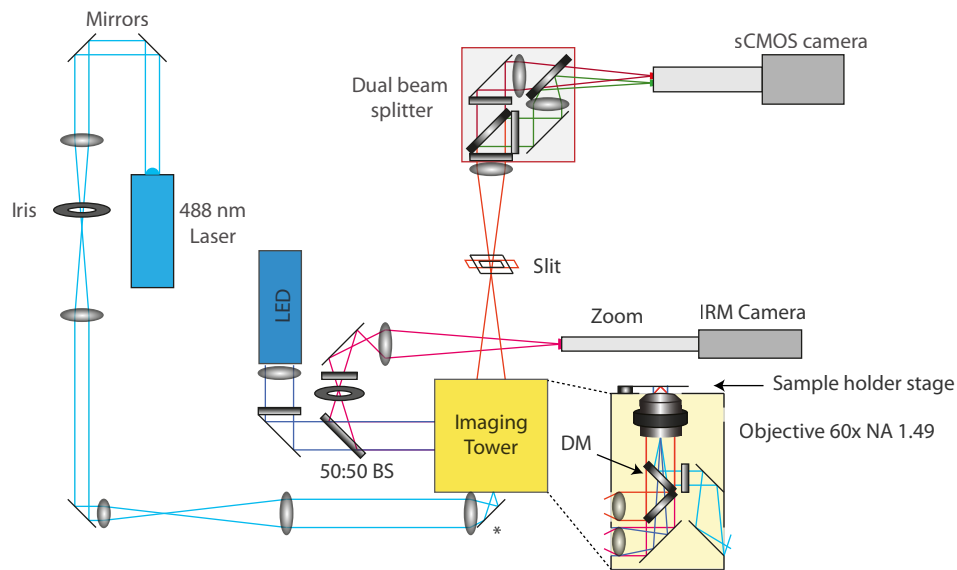


Figure 7.4.: Schematic of the TIRF setup used. A 488 nm laser is focussed on the back focal plane of the TIRF objective. Sample is mounted on the sample holder on top of the tower. The emission signal is collected by the same objective and channelled via a slit to a dual-beam splitter that enables imaging in two colour channel separated by the wavelength [142, 143]. The image is projected onto a sCMOS camera. The sample can also be visualised via a blue LED illumination and image projection onto a monochrome camera. * denotes moveable lens for angle adjustment. DM: dichroic mirror, BS: beam splitter.

of light, and refractive indices of the sample and glass. Therefore, in an experimental setup, varying the angle of incidence is enough to vary the depth of the evanescent field.

7.2.2. Design

In this thesis, a home-built TIRF setup was used (Figure 7.4). The microscope also allows epifluorescence and interference reflection (IRM) microscopy. The setup is located in a vibration isolation chamber that is separated from the building foundation to achieve high stability. The fluorescence part is equipped with a 488 nm Omicron, LuxX 488–100 diode laser that focusses on the back focal plane of an oil immersion 60× NA 1.49 Nikon objective lens. The emission part consists of a dual-beam splitter combined with two bandpass filters, 500–540 nm and 570–640 nm to allow two channel imaging. A sCMOS camera (Hamamatsu, ORCA Flash4.0) is used for detection, that is cooled to reduce the noise during imaging. The IRM is powered by a blue LED. The IRM image is captured using a Lumenera Lm135M camera.

7.3. Microscopy assays

To prepare samples for imaging, a flow cell was prepared (Figure 7.5). The flow cell is a sandwich of a spacer (here parafilm) between two glass coverslips. The coverslips used in all the microscopy assays were 22×22 mm (Corning, 2850-55) and 18×18 mm (Thermo

Scientific Menzel, 15757572) and were cleaned thoroughly (see glass cleaning below) and surface treated (see silanisation below) for binding of biological substrates while delivering high signal-noise ratio.

7.3.1. Glass cleaning

Coverslips were loaded into coverslips racks and racks were placed in a glass container that can withstand heat, low pH, and ultrasonic waves. The container was filled with 20 % Mucosal in distilled water (University Tübingen chemical store) till all coverslips were fully covered and was sonicated for 15 min. Afterwards, the racks were placed in a clean glass box and washed thoroughly under running water to remove all the detergent for about 3–4 min. The rack was then placed in another clean glass box and filled with ethanol (99 % technical University Tübingen chemical store) and sonicated for 10 min. The coverslips were rinsed with running water as described above. This full cycle was repeated 3 more times before coverslips were dried under the hood using pressurised and filtered air.

7.3.2. Silanisation

To attach biological substrates such as enzymes, antibodies etc., to the glass surface and avoid denaturation of these proteins, a hydrophobic surface was created using methytrichlorosilane (MTS, Sigma, M85301). This protocol uses easy-cleaned coverslips (described in Section 7.3.1) cleaned on the same day. Instead of drying, the coverslips were immersed into 1 M HCl for 1 h at 75 °C while being sonicated. Afterwards, the glass box was carefully removed and cooled at room temperature for about 15 min. The coverslip racks were placed in a clean box and were rinsed quite thoroughly with running water for about 7–10 min. The coverslips were then air-dried thoroughly under the chemical hood. To remove any remnants of water on the coverslips, the racks were placed in a desiccator under vacuum for about 30 min. Afterwards, a 1.5 ml eppendorf tube was placed in a 5 ml glass beaker at the base and centre of the desiccator, while the racks rested on the ceramic sieve platform. Quickly, 500 μ l of MTS was pipetted into the eppendorf tube and the desiccator was closed. MTS is highly volatile and harmful when inhaled, so mask was used while handling it. After the desiccator was closed, vacuum was applied while quickly closing the valve so that not all MTS was evaporated. The valve was tightly adjusted in such a way that some MTS started to evaporate into the desiccator chamber for about 30 s to 1 min. The valve was then closed tightly, allowing all MTS in the chamber to react with the coverslips. After about 10 min, the valve was opened a bit to increase the vacuum and evaporate more of the MTS. This process was repeated until all MTS was evaporated. Afterwards, the hydrophobicity of the coverslips was checked by placing a 50 μ l droplet of water on them and visually observing water-glass contact angle (preferably 90° or less). If the angle is too small, more MTS can be added and the process can be elongated until the desired hydrophobicity (contact angle of about 90 or less) is achieved. However, leaving the coverslips overnight in the desiccator with valve closed in the last step of silanisation gave the best results and is recommended.

7.3.3. Flow cell preparation

Easy cleaned and silanized coverslips were used to create a sandwich with parafilm (Figure 7.5). This flow cell was quickly heated on the hot plate on 120 °C for about 1 min and then allowed to cooled down at the work desk.

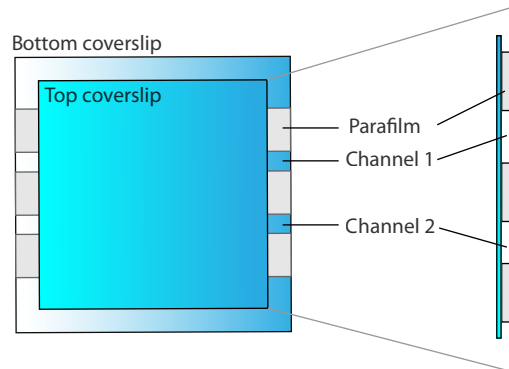


Figure 7.5.: Schematic illustration of a flow cell. A flow cell consisting of two channels is shown here in two views. It is a sandwich of 22×22 mm coverslip (bottom, white-blue), parafilm (separator, grey), and 18×18 mm coverslip (top, cyan-blue).

7.3.4. Microtubule polymerization—taxol stabilisation

A 10 % rhodamine labelled tubulin aliquot (4–6 mg/ml) was taken from the –80 °C freezer and thawed in the hands and then placed on ice. A microtubule mixture consisting of 1 μM tubulin, 1 % DMSO, 1 mM MgCl₂, 1 mM GTP (all final concentrations) brought upto 7 μl with 1× PEM buffer (80 mM PIPES, 1 mM MgCl₂, 1 mM EGTA, 100 mM KOH, the pH was adjusted to 6.9 with KOH). The microtubule mix was given a short spin on the table-top centrifuge and incubated at 37 °C for about 30–45 min. For longer microtubules, incubation was 1 h. Afterwards, the mix was resuspended in 400 μl of PEM supplemented with 10 μM taxol that will stabilise the polymerised microtubules. This mixture was then centrifuged in a pressurized air-driven ultracentrifuge (Beckman Coulter) at 22–24 psi for 5 min, to remove remnant free tubulin. Next, supernatant was discarded and pellet was resuspended in 200 μl of PEM supplemented with taxol (10 μM). Taxol stabilized microtubules were stored at 37 °C until used and can be stored for a couple of days.

7.3.5. Microtubule polymerization—GMP-CPP stabilisation

Similar to taxol stabilized microtubules, a microtubule polymerisation mixture was made but by using GMP-CPP—a less hydrolysable GTP analogue—instead of GTP. The mixture consisted of 2 μM 10 % rhodamine-labelled tubulin, 1 mM MgCl₂, 1 mM GMP-CPP (Jena Bioscience, NU-405S) filled up to 50 μl with PEM and was incubated on ice for 5 min. After a short spin, the mix was incubated for 2 h at 37 °C. It was spun down as mentioned above and final pellet was resuspended in 200 μl of 1× PEM. The microtubules can be stored for couple of days at 37 °C. To stabilize them for about a week, they were resuspended in 1× PEM supplemented with 10 μM of taxol.

7.3.6. Polarity marked microtubules

Polarity marked microtubules were used to mark the ends of the microtubules and therefore discern the directionality of motors. There were two methods.

First method: GMP-CPP-stabilised microtubule seeds were prepared using 2–3 μM unlabelled tubulin, 1 mM MgCl_2 , 1 mM GMP-CPP and $1\times$ PEM. This mixture was incubated for 1 h at 37°C. Afterwards, microtubules were spun down and the pellet was resuspended in the same constituents using 1–2 μM of 10% rhodamine-labelled tubulin. This reaction was incubated further for 1 h at 37°C. Then, 1–2 μM of 10% rhodamine-labelled tubulin was added and incubated for another hr before they were spun down and re-suspended in $1\times$ PEM.

Second method: Microtubule polymerisation mixture was made similar to regular GMP-CPP microtubules (see above) except that the tubulin concentration was 3 μM and 20% rhodamine labelled tubulin was used. This mixture produces highly labelled microtubule seeds. The solution was incubated for 1.5 h. It was then centrifuged as mentioned previously and pellet was resuspended in 40 μl of 37°C, warm preheated $1\times$ PEM. For growing ends on highly labelled seeds, 5% rhodamine labelled tubulin 2 μM , 1 mM MgCl_2 , 1 mM GMP-CPP, 8 mM N-Ethylmaleimide (NEM), 50% $1\times$ PEM volume-wise was filled up to 29 μl and incubated on ice for 1 min. 1 μl of β -mercaptoethanol(20% in PEM) was added and incubated at 37°C. 20 μl of seed-mix with 20% rhodamine-labelled tubulin, grown at the beginning of this protocol was added. This 50 μl of total reaction mixture was incubated at 37°C for 30 min. After centrifugation, the final pellet was resuspended in PEM-taxol as described earlier.

7.3.7. Microscopy assay and imaging conditions

The flow channels were washed 4–5 times with sterile filtered buffer $1\times$ PEM. This was followed by incubation with anti- β tubulin (Sigma Aldrich, T7816) for 15–20 min at room temperature. Afterwards, the channels were washed once with PEM and blocked using 1% Pluronic F-127 (Sigma-Aldrich, P2443) in PEM for 20–25 min. This step was followed by 5 times washing with PEM and incubation with 10% rhodamine-labelled, taxol-stabilised microtubules for 15 min. The assay buffer (PEM, 0.08 mg/ml casein, 1 mM ATP, 20 mM D-glucose, 250 nM glucose oxidase, 134 nM catalase, 0.5% BME) containing the protein was added after a quick wash of the channel. Samples were imaged at 25°C on a custom built total-internal-reflection-fluorescence (TIRF) microscope describe in Section 7.2.2. To visualize motor movement, 40 s time-lapse videos were recorded at 10 frames per second (fps) using a continuous image acquisition mode with 100 ms exposure. The data was acquired using 10 mW laser power.

7.3.8. Photobleaching assay

The photobleaching assay was conducted in the same manner as the rest of the *in vitro* preparations, except for the assay buffer. The assay buffer consisted of 0.08 mg/ml casein, 1 mM AMP-PNP, 10 mM DTT and PEM, pH 6.9. In the presence of AMP-PNP, motors bind with both heads in a strongly bound state. GMP-CPP stabilised microtubules were used. The data was acquired at the same conditions mentioned earlier but using a higher excitation

laser power of 10–30 mW. Post-acquisition, kymographs were generated and intensity values were extracted from them, followed by an analysis via a custom-written, MATLAB-based step-finding algorithm [144]. Note: This assay also serves as a co-localisation assay when using laser intensities.

7.3.9. Microsphere preparation and force measurements

Microsphere functionalization and protein-microsphere coupling was performed as reported previously [39]. The sample preparation and assay buffer for optical tweezers experiments were the same as mentioned in Section 7.3.7. All measurements were performed on a custom-built, single-beam optical tweezers setup [140, 145] described earlier (Section 7.1). The experiments were conducted with a trap stiffness of 0.01 pN/nm and recorded with a sampling rate of 4 kHz. Calibration was performed by analysing the height-dependent power spectral density combined with a drag-force method as reported earlier [146, 147].

7.3.10. PIP strip assay

The PIP strip (Echelon Biosciences) were blocked overnight in 7 ml blocking solution at 4 °C while shaking. The PBST blocking buffer consisted of 0.1 % Tween 20 and 3 % non-fat bovine serum albumin in phosphate buffer saline (PBS). Next day, the buffer was replaced with 5 ml of fresh blocking buffer and 40 μ l of purified protein was added. It was incubated for 1 h with shaking at room temperature. The PIP strip was then washed 3 \times with the PBST buffer for 7 min while shaking. The PIP strip was immersed in 7 ml of blocking buffer and 3.5 μ l (1:2000 dilution, stock 0.4 mg/ml) of anti-GFP antibody (mouse IgG, Roche, 11814460001) was added. It was then incubated for 1 h 20 min at room temperature while shaking. The PIP strip was then washed 3 \times with the PBST buffer for 7 min while shaking. The strip was then immersed in 6 ml blocking buffer and 600 μ l of secondary antibody (1:1000 dilution provided in SuperSignal West Pico Mouse kit, Thermo Scientific, 35060), and incubated at room temperature for 1 h on a shaker. The secondary antibody was an anti-mouse and coupled to horse radish peroxidase that was provided in the kit. After secondary antibody incubation, the blot was washed 4 \times with PBST buffer for 17 min each. For detection, 1:1 mixture of 3 ml enhancer solution and 3 ml of peroxidase solution was used. The membrane was placed in a clean incubation box and the detection mixture was poured. The blot was incubated for 90 s while being shaken by hand. The blot was transferred onto a clean transparency sheet and chemiluminescence was detected for 5–15 min depending on the signal using the FusionFX7 imaging system (Peqlab).

Part III.
Results and Discussion

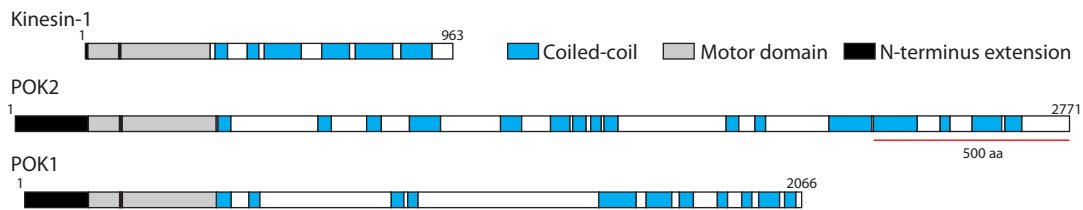
8. The kinesin motor domains of POK2 and POK1

POK2 and POK1 are the largest members of the *Arabidopsis* kinesin-12 family with respect to their molecular weights, with POK2 being the largest kinesin known across taxa. To understand their lengthy protein structure, the domain organisation of POK1 and POK2 was created using bioinformatics toolkit (Figure 8.1) [35]. The motor domain is highly conserved among the kinesin-12 family with a closest relative outside plants being human kinesin-12, hKif15. The motor domain is located at the N-terminus consistent with other kinesin-12 family members and kinesin classification. Interestingly, despite being enormous in length, the motor domain region is about 340 amino acids long comparable to the motor size of the entire kinesin family. Unusually, POK1 and POK2 have an extraordinarily long and disordered N-terminus preceding their motor domain (160–190 amino acids as compared to 7 amino acids in conventional kinesin) [87]. Besides the conventional motor domains, both of the kinesins contain coiled-coil domains and unstructured/unannotated regions.

The hypothesis of an active role of POK2 and POK1 during cytokinesis in guiding the phragmoplast implies a motile interaction of the motors with the peripheral microtubules. Therefore, investigating the motile behaviour of POKs was performed. and Due to their large size, truncated constructs of these motor proteins were created. The following sections detail the findings for the motor domains of POK2 and POK1. Parts of this chapter have been published in *Biophysical Journal* [148] and are direct excerpts from the same [148].

8.1. POK2_{1–589}-GFP is a plus-end-directed dimeric motor

POK2 has been the prime focus of this thesis. To focus on the motor functionality, a POK2_{1–589} minimal motor construct was generated (Figure 8.2). This construct contains the N-terminal extension, motor domain and the first predicted coiled-coil and is about 94 kDa. POK2_{1–589} was fluorescently tagged with green fluorescence protein (GFP) after the coiled-coil towards the C-terminus, followed by a 6× His-tag. To test if the coiled-coil was sufficient for dimerisation of the truncated motor, *in vitro* photobleaching assays were conducted on a custom-build TIRF setup [143]. The taxol-stabilized and rhodamine-labelled microtubules were immobilised on the surface of the flow channel using an anti-tubulin antibody (see Section 7.3.7). Purified POK2_{1–589}-GFP molecules were flushed into the channel in the presence of AMP-PNP. AMP-PNP is a non-hydrolysable analogue of ATP that enables the kinesin motorheads to interact with the microtubule in a strongly bound and non-motile state. Co-localisation of POK2_{1–589}-GFP with the rhodamine-labelled microtubules was observed. The fluorescence intensity of the POK2_{1–589}-GFP molecules was measured as a function of time with a high laser intensity. It was found that most GFP-tagged kinesin molecules bleached in one or two steps. For the single-step bleaching events, the step-



Kinesin	Motif	Location
Kinesin-1	Motor domain	8-325
Kinesin-1	Neck linker	326-338
POK2	Motor domain	193-527
POK2	Neck linker	528-532
POK1	Motor domain	168-503
POK1	Neck linker	504-509

Figure 8.1.: Size and domain comparison among kinesin-1, POK2, and POK1. (*Top*) The full length protein domain organisation for POK2 and POK1 in comparison to conventional kinesin-1 (hKif5b). The colour key depicts associated domains, while white regions represent unstructured or unidentified domains. Coiled coil annotation was achieved using PCOILS and MARCOILS with window size 28 [35]. Coiled coil probabilities of 0.99–1 were considered. aa: amino acids. (*Below*) Table annotating the location of domains in the respective amino acid sequences.

amplitude was in accordance with twice the amplitude in two-step bleaching, suggesting that two GFP molecules bleached simultaneously (Figure 8.3a). This oligomeric state of the POK2_{1–589}-GFP (monomeric molecular weight 94 kDa) was also validated using a native-PAGE gel. The native-PAGE shows two distinct bands for POK2_{1–589}-GFP (Figure 8.3b). Since native gels rely on the net charge of the native protein itself than the molecular weight, it is difficult to determine the molecular weight and nevertheless, this approach was chosen to complement the photobleaching assays and support a dimeric state of POK2_{1–589}-GFP. Upon corroborating POK2_{1–589}-GFP nature on the gel with the truncated rat kinesin (rk430—it is a kinesin-1 construct that is also truncated after the first coiled-coil; monomeric molecular weight 80 kDa), which might have roughly similar structure in contrast to bovine serum albumin (BSA) that is a fully globular protein, it is believed that these two bands denote monomers and dimers (Figure 8.3). Together, these data suggest that POK2_{1–589}-GFP binds to microtubules and is a dimeric motor. This observation is consistent with previous studies demonstrating that the first coiled-coil after the kinesin motor domain is sufficient for its dimerisation [149].

dimerisation of kinesins has been shown to facilitate processive motion [38]. Therefore, POK2_{1–589}-GFP was tested for its motility in the presence of 1 mM ATP in a TIRF microscopy assay. It was found that POK2_{1–589}-GFP molecules robustly translocated on the microtubule lattice (Figure 8.4d,f). To discern the directionality of the motor, polarity-marked microtubules were polymerized. When POK2_{1–589}-GFP molecules were flushed onto the polarity-marked microtubules in the presence of 1 mM ATP, it was found that on average POK2_{1–589}-GFP move towards the microtubule growing-end (Figure 8.4e,f). Any preference

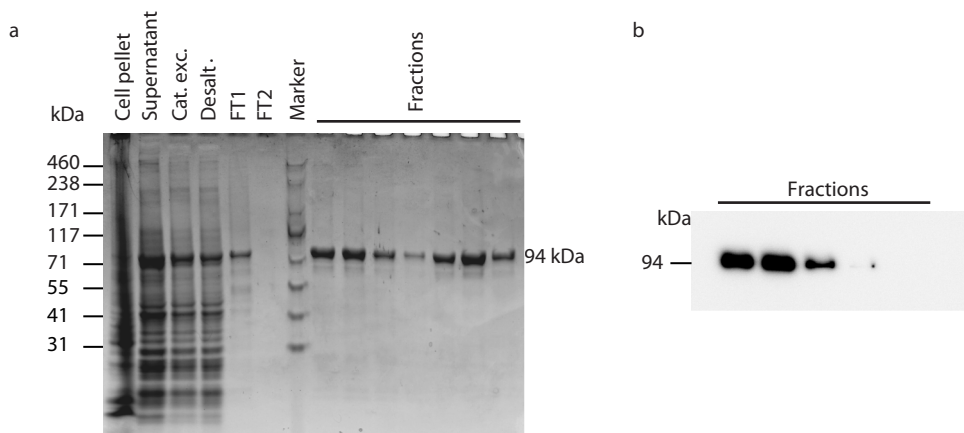


Figure 8.2.: Quality control of POK2₁₋₅₈₉-GFP after purification. (a) 4–20% Tris-Glycine SDS-PAGE gel coomassie stained for protein fractions. (b) Anti-GFP western blot for purified POK2₁₋₅₈₉-GFP fractions. Cat. exc.: cation exchange, Desalt.:desalting, FT: flow through. The figure is modified from [148].

or extended dwell times for the microtubule plus-ends were not observed. This experiment shows that POK2 is a plus-end-directed motor as expected for kinesins with an N-terminally located motor domain. Motility of POK2₁₋₅₈₉-GFP *in vivo* was validated by Dr. Sabine Müller’s group using a transient expression in *Nicotiana benthamiana*.

8.2. POK2₁₋₅₈₉-GFP motor switches between processive and diffusive modes

Using motility assays, it was clearly observed that POK2 is an active motor. Upon analysing the trajectories of single POK2₁₋₅₈₉-GFP molecules using kymographs, it was noticed that although the overall motion was directed towards the microtubule plus-end, there were recurrent episodes of random, forwards and backwards motion (Figure 8.4d,f). These forwards and backwards motion are suggestive of diffusive motion, i.e. weak electrostatic interactions between the motorheads and the microtubule lattice. Thus, POK2₁₋₅₈₉-GFP is capable of switching between processive and diffusive modes.

For a single motor, processive and diffusive motion are mutually exclusive. During processive motion, kinesins step in an ATP-dependent hand-over-hand fashion and directed manner along microtubules, whereby the kinesin heads alternate between strongly and weakly bound states. During diffusion, an ATP independent process, both heads are thought to be in a weakly bound state: the motor takes many random forward and backward steps [144]. Since the heads are weakly bound, the stepping rate is typically much higher compared to the one during directed motion. Having discovered POK2₁₋₅₈₉-GFP switches motility modes was exciting but not unusual compared to other kinesins. Diffusive behaviour as an intermittent part of processive motion has been earlier observed for *Drosophila* kinesin-14 Ncd under low-ionic buffer conditions [49, 50], *Xenopus* kinesin-7 CENP-E [18], human kinesin-5 Eg5 [51], human kinesin-8 Kif18B [150] and human kinesin-12 Kif15 [52]. There are also instances of purely one-dimensional (1D) diffusive motion, such as human kinesin-13 MCAK [48] and

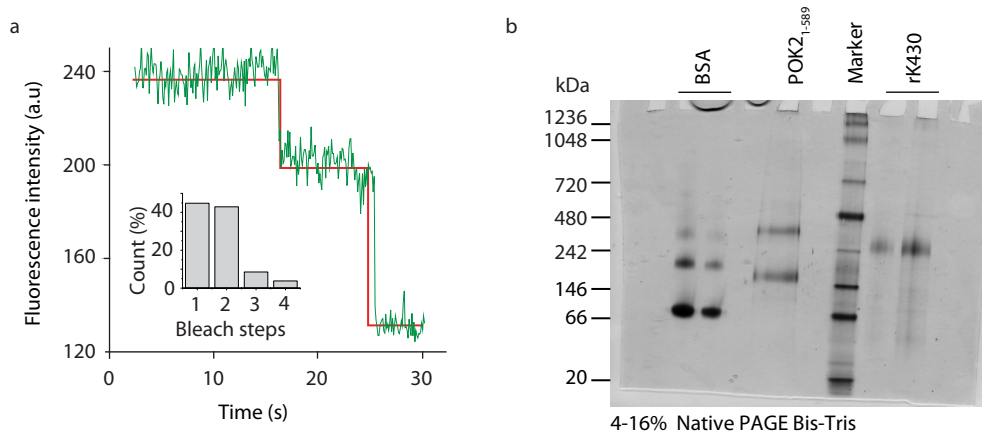


Figure 8.3.: POK2₁₋₅₈₉-GFP is a dimeric kinesin. (a) An example trace of the fluorescence intensity over time for a single POK2₁₋₅₈₉-GFP bound to the microtubule in the presence of 1 mM AMP-PNP. The relative frequencies of bleaching steps are represented in the inset ($N = 105$). (b) A 4–20 % Native PAGE gel depicting monomeric and dimeric state of POK2₁₋₅₈₉-GFP (94 kDa monomer) along with dimeric rK430 (80 kDa monomer) and oligomeric bovine serum albumin (BSA, 66 kDa monomer). The figure is modified from [148].

kinesin-3 Kif1A [151]. In both above-mentioned scenarios and in comparison to directed motion, over short length scales, diffusion allows faster, direction- and energy-independent targeting, e.g. of microtubule ends.

How does a motor capable of switching motility modes might guide the phragmoplast? To address this question, it was crucial to understand two aspects. A) The molecular structure of the motor. B) The relative time motor spends on the microtubule lattice in an ATP-dependent directed mode versus ATP-independent diffusive mode.

To address the first aspect, it was hypothesized that the disordered region preceding the POK2 motor domain, might cause the diffusive behaviour. This region, roughly 190 amino acid long, is distinctive to POK2 (Figure 8.1). This N-terminal extension (Nt_e) might cause the diffusive behaviour by interacting with the microtubule lattice in a weak electrostatic manner. Therefore, a truncated POK2 construct lacking Nt_e , POK2₁₈₃₋₅₈₉-GFP, was generated, expressed and purified the same way (Figure 8.5). Conducting motility assays in the presence of rhodamine-labelled microtubules and 1 mM ATP, it was found that POK2₁₈₃₋₅₈₉-GFP interacted with the microtubules for a much longer time 11 ± 1 s (mean \pm standard error (SE), $N=38$) compared to 1.9 ± 0.1 s for POK2₁₋₅₈₉-GFP (Figure 8.6). The kymographs displayed diffusive motion of POK2₁₈₃₋₅₈₉-GFP (Figure 8.6b). Surprisingly, the microtubule binding affinity of the POK2₁₈₃₋₅₈₉-GFP was also reduced compared to POK2₁₋₅₈₉-GFP under similar concentration conditions (Figure 8.7a). When looked into the protein sequence of POK2- Nt_e in detail, a similarity to 80 amino acid long Nt_e of BimC was found (Figure 8.7b). BimC is the founding member of the kinesin-5 subfamily and a native of *Aspergillus*. The Nt_e of BimC has been reported to contain a secondary microtubule binding site [152]. The loss of the Nt_e in BimC also shows reduced microtubule affinity [152], however the structural contribution is not known. Together, these data suggest that the N-terminus of the POK2 promotes motor processivity and a higher microtubule affinity. Presumably, the N-terminus of POK2 enables efficient capturing or binding of microtubules.

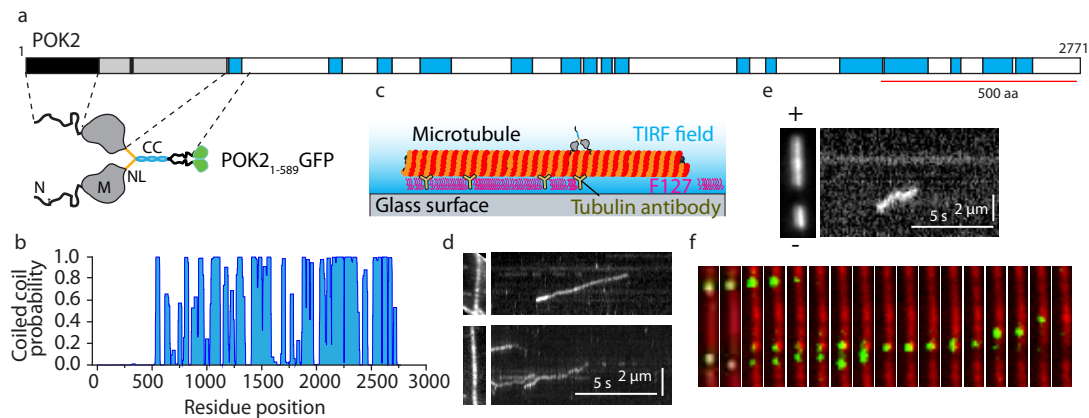


Figure 8.4.: POK2₁₋₅₈₉-GFP is a plus-end-directed motor. (a) Structural cartoon representation of the POK2₁₋₅₈₉-GFP used for *in vitro* experiments in comparison to the full length POK2. The N-terminal extension (*black*) precedes before the motor domain (*grey*). The motor domain contains an ATP binding site (*black strip in grey*). The motor domains are continuous with the neck linker (*orange*) and subsequently first coiled coil (*cyan*). *Green* towards the end represents fused GFP. (b) Predicted coiled-coil probability plot for POK2 (refer Figure 8.1). (c) Schematic of the *in vitro* reconstituted experimental set up. (d) Kymographs representing POK2₁₋₅₈₉-GFP motility on the microtubules represented on their left. (e) Polarity-marked microtubule denoting plus-end-directed motion of POK2₁₋₅₈₉-GFP. (f) An example montage illustrating POK2₁₋₅₈₉-GFP motility. Microtubules are labelled in red and green represents POK2₁₋₅₈₉-GFP. Images are 4.75 μm high. Time between frames is 0.5 sec. The figure is modified from [148].

Once bound, a conformational change might facilitate ATP-dependent directed motion.

Interestingly, using a yeast-2-hybrid (Y2H) assay, our collaborator Dr. Sabine Müller showed that MAP65-3 interacts with the POK2-Nt_e region [92]. Moreover, POK2₁₋₅₈₉ and MAP65-3 *in planta* localize at the phragmoplast midzone, presumably promoting microtubule-cross-linking there [92]. Hence, POK2-Nt_e seems true to its disordered protein region and might mediate binding of different partners. The N-terminus might allow POK2 to land efficiently on the microtubule lattice and undergo processive motion to catch up with growing microtubule ends. Once it reaches near the developing cell plate, where MAP65-3 is localized, POK2 might be stabilized there by interaction between MAP65-3 and POK2-Nt_e. This stabilisation through supported cross-linking might provide stability to the phragmoplast microtubules at the midzone.

8.3. MSD analysis of POK2₁₋₅₈₉-GFP motility modes

To understand how much time POK2 spent in the processive or diffusive state, this molecular behaviour was objectively quantified. After acquiring data in the motility assays, single POK2₁₋₅₈₉-GFP molecules were tracked on individual microtubules using an automated data analysis pipeline. This data analysis pipeline was based on 2D Gaussian models [154]. Histograms of total interaction time of the motor on the microtubule lattice and motor displacements were plotted (Figure 8.8a,b). The histograms showed peaked distributions, which are indicative of multiple underlying processes such as directed and diffusive modes

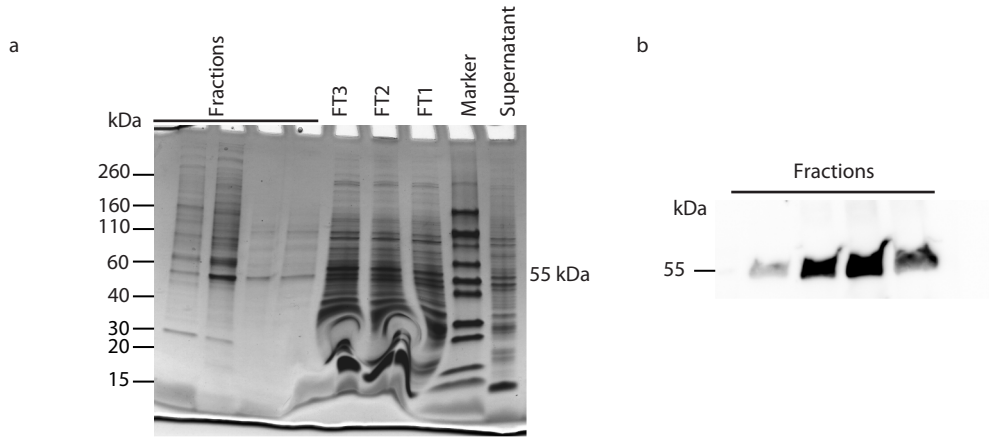


Figure 8.5.: Quality control of POK2₁₈₃₋₅₈₉-GFP after purification. (a) 4–20% Tris-Glycine SDS-PAGE gel coomassie stained for protein fractions. (b) Anti-GFP western blot for purified POK2₁₈₃₋₅₈₉-GFP fractions. FT: flow through. The figure is modified from [148].

(Figure 8.8). In contrast, exponential distributions are indicative for a single rate-limiting step [155]. To quantify this behaviour, a statistical approach was used to measure the spatial extent of motion over time: a mean-squared-displacement (MSD) analysis. The MSD of a single POK2₁₋₅₈₉-GFP motor as a function of lag time was best fitted by a parabola with significant linear and parabolic coefficients (Figure 8.8c). The presence of both terms confirmed that POK2₁₋₅₈₉-GFP indeed has two motility modes. While the linear term is related to diffusion, the quadratic term is due to directed motion [156, 157]. Diffusion can occur simultaneously with directed motion, for example, when a particle is freely diffusing in 3-D and subjected to a flow or drift. However, in this case, POK2₁₋₅₈₉-GFP was exclusively either in the processive or the diffusive state. Surprisingly, this scenario has not been addressed with respect to single molecular machines interacting with filaments in a one-dimensional diffusive system previously. Therefore, Dr. Basudev Roy and Prof. Erik Schäffer assisted and derived the expected MSD as a function of lag time τ for a motor being either in the diffusive or in the processive state [148].

$$\text{MSD}(\tau) = \phi^2(v_0^2 + \sigma_v^2)\tau^2 + 2D(1 - \phi)\tau + 2\varepsilon^2, \quad (8.1)$$

where ϕ is the fraction of the total interaction time the motor spends in the directed mode, v_0 and σ_v the mean speed and its standard deviation, respectively, D the diffusion coefficient, and ε an offset related to the tracking precision and image acquisition [158]. Equation 8.1 accounts for the exclusive character of the states and the amount of time in the respective states avoiding an underestimation of both the speed and the diffusion coefficient [150]. The derivation of this equation is given in Section 8.3.1 and in [148].

The Equation 8.1 accounts for the exclusive states of the POK2₁₋₅₈₉-GFP, but as five parameters enter Eq. 8.1, namely ϕ , v_0 , σ_v , D , and ε , and a fit of Eq. 8.1 to the data only results in three independent coefficients of the parabola, the system is under-determined. Thus, a MSD analysis alone cannot provide all the parameters. Therefore, in addition to the MSD, a speed correlation index (SCI) analysis was used to quantify relative times and complement MSD analysis.

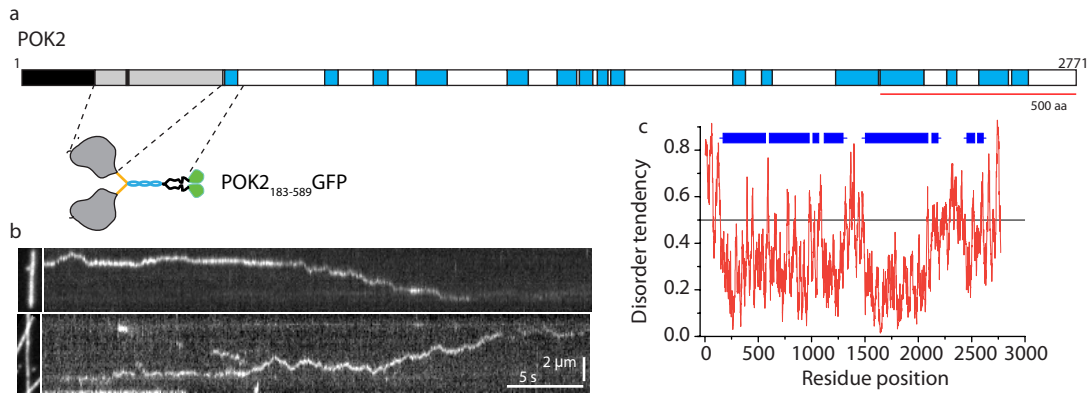


Figure 8.6.: POK2₁₈₃₋₅₈₉-GFP is a diffusive motor. (a) Structural cartoon representation of N-terminal truncated POK2₁₈₃₋₅₈₉-GFP. (b) Exemplary kymographs of POK2₁₈₃₋₅₈₉-GFP diffusive motility on the microtubules represented on their left. (c) Disordered probability plot for POK2 full length. The plot was obtained from IUPRED under default parameters [153]. The blue bars indicate predicted globular/structured regions, while the red line represents disorder tendency estimated from pairwise amino acid energy content. The black line indicates the threshold below which polypeptides are predicted to be structured. The figure is modified from [148].

8.3.1. Derivation of MSD equation

The average MSD was plotted against lag time and fitted with a parabola because the motor exhibited diffusive as well as directed motion. For *simultaneous* 1D diffusion and directed motion, the MSD as a function of lag time τ is given by the well-known equation:

$$\text{MSD}(\tau) = v^2\tau^2 + 2D\tau + 2\epsilon^2. \quad (8.2)$$

The first term refers to the directed motion, where v is the speed. The second term is the contribution by the diffusive motion, where D is the diffusion coefficient. The last term is a constant related to the tracking precision and image acquisition [158]. Although this equation yields the parameters D and v , the motion occurs simultaneously. An example for such simultaneous motion is a particle diffusing in a liquid with an applied flow. However, such simultaneous motion is impossible for a molecular motor taking discrete steps. Steps are exclusively either directed or random. Furthermore, for kinesins, the average stepping rate in the diffusive mode is typically much larger compared to the directed mode. For example, a kinesin moving with a directed speed of 400 nm/s takes about 50 steps per second. Assuming the motor takes 8 nm steps during diffusion [144] and has a diffusion coefficient of $0.032 \mu\text{m}^2/\text{s}$, the diffusive stepping rate is $2D/\delta^2 = 1000$ steps per second ($\delta = 8$ nm), $20\times$ higher compared to the directed state. Thus, the motor has distinct and different properties in the two modes. To account for the switching behaviour, a modification to the Eq. 8.2 is required. Therefore, the MSD equation that accounts for a motor being exclusively either in a diffusive or directed mode is derived in the following.

The motion of a motor that switches between the different modes is described by the Fokker-Planck equation

$$\frac{\partial p}{\partial t} + \eta(t)v\frac{\partial p}{\partial x} = [1 - \eta(t)]D\frac{\partial^2 p}{\partial x^2}, \quad (8.3)$$

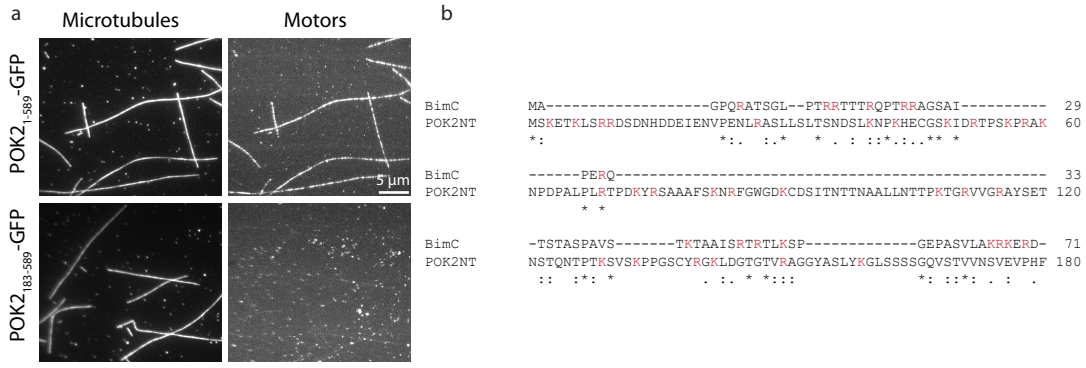


Figure 8.7.: Reduced affinity of POK2_{183–589}-GFP with the microtubule lattice. (a) Maximum projections representing the co-localisation of motors onto the microtubule lattice in 1mM AMP-PNP. Images were acquired using TIRF microscopy under the same conditions and contrast. Even though the concentration was about twice that of POK2_{183–589}-GFP based on the western blot and nanodrop quantification, much less POK2_{183–589}-GFP bound to the microtubules during the same amount of time. (b) Multiple sequence alignment (MSA) of the POK2 N-terminal extension (Nte) with BimC. The MSA was performed using Clustal Omega with default parameters [35]. Asterisks signify conserved residues, colons represent conservation among amino acids exhibiting strongly similar properties, and periods mark conservation among amino acids exhibiting weakly similar properties. Positively charged residues that may interact with the negatively charged tubulin e-hooks are indicated in red. The figure is modified from [148].

where $p(x, t)$ is the probability density of the motor being at a position x at time t . $\eta(t)$ is either 0 or 1, randomly switching between the two values as a function of time. The number indicates whether the particle is diffusing ($\eta = 0$) or translating ($\eta = 1$). Equation 8.3 is for one realisation of $\eta(t)$ and also assumes that the average switching rate is small compared to the stepping rate of the molecular motor, i.e. the time between switches is long compared to the time per step. The Fourier transform of Eq. 8.3 yields

$$\frac{\partial \tilde{p}}{\partial t} + ik\eta v \tilde{p} = -k^2(1 - \eta)D \tilde{p}, \quad (8.4)$$

where \tilde{p} is the Fourier transform of p , k is the spatial frequency corresponding to the Fourier transform of x , and i is the imaginary unit. Separating variables, Equation 8.4 can be written as

$$\frac{\partial \tilde{p}}{\tilde{p}} = -(k^2(1 - \eta)D + ik\eta v) \partial t. \quad (8.5)$$

Integration of both sides of Eq. 8.5 yields

$$\ln \frac{\tilde{p}}{\tilde{p}_0} = -(k^2(1 - \phi)D + ik\phi v)(t - t_0), \quad (8.6)$$

where \tilde{p}_0 is an integration constant, t_0 is the initial time and the time interval $t - t_0$ can be set to the time lag τ . The parameter ϕ is the time average of $\eta(t)$ over the time interval $t - t_0$ and, thus, represents the time fraction the motor spends in the directed state. For $\phi = 1$, the motor is purely in the directed mode and for $\phi = 0$ only diffusing. The equation holds for times large compared to the switching time, for which case the variance of ϕ is small.

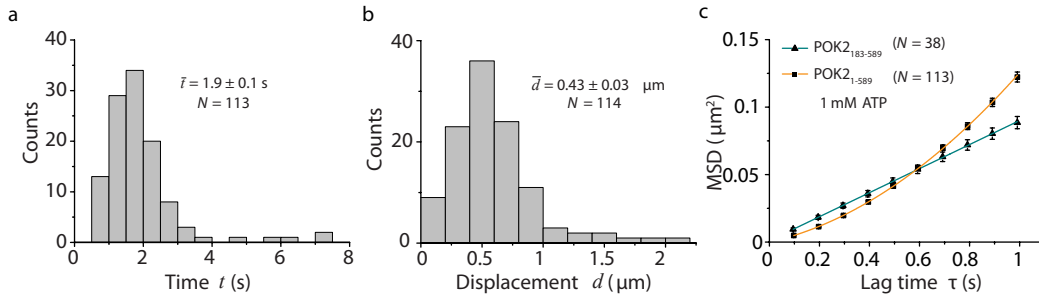


Figure 8.8.: POK2₁₋₅₈₉-GFP switches between processive and diffusive modes. Distributions of total interaction time (a) and overall displacement (b) of POK2₁₋₅₈₉-GFP on the microtubule lattice are shown. Mean values, \pm SE, and total number of molecules are indicated. (c) The mean-squared-displacement (MSD) of POK2₁₋₅₈₉ and POK2₁₈₃₋₅₈₉ in 1 mM ATP plotted against the lag time is shown. The orange line is a fit of the Eq. 8.3.1 to the POK2₁₋₅₈₉-GFP data, whereas the green line is a linear fit to the POK2₁₈₃₋₅₈₉ data. The error bars are SE of squared-displacement values. The figure is modified from [148].

The last equation can be rewritten as

$$\tilde{p} = \tilde{p}_0 \exp \left[-(k^2(1 - \phi)D + ik\phi v)\tau \right], \quad (8.7)$$

for which the inverse Fourier transform results in the probability density

$$p(x, \tau) = \frac{1}{\sqrt{4\pi(1 - \phi)D\tau}} \exp \left[-\frac{(\phi v\tau + x)^2}{4(1 - \phi)D\tau} \right]. \quad (8.8)$$

The mean-squared displacement is then defined by

$$\langle x^2(\tau) \rangle = \text{MSD}(\tau) = \int_{-\infty}^{+\infty} p(x, \tau) x^2 dx, \quad (8.9)$$

which results in

$$\text{MSD}(\tau) = (\phi v\tau)^2 + 2(1 - \phi)D\tau, \quad (8.10)$$

where, as pointed out above, ϕ is the fraction of the time spent in the directed motion.

If the speed of an individual molecular motor is constant for an individual run but changes from molecule to molecule and run to run, then the average MSD of the individual MSDs of the individual runs differs from Eq. 8.10. The difference arises because of the non-linear, i.e. quadratic, contribution of the speed to the MSD. It is assumed that the speed is normally distributed with a mean speed v_0 and standard deviation σ_v . If the various MSDs are denoted for different runs as $\langle x^2 \rangle(\tau)_n$, where n is the index of the run, the expectation value of the average MSD for large n is calculated according to

$$\langle \langle x^2 \rangle(\tau) \rangle_n = (1 - \phi)2\langle D \rangle_n \tau + \phi^2 \langle v^2 \rangle_n \tau^2. \quad (8.11)$$

The second moment of the speed, i.e. the mean-squared speed, is $\langle v^2 \rangle_n = v_0^2 + \sigma_v^2$ (note that the variance is $\sigma_v^2 = v_0^2 - \langle v^2 \rangle$). If the mean diffusion coefficient is denoted by $\langle D \rangle_n = D$ then the final result of the modified Eq. 8.10 is

$$\text{MSD}(\tau) = \phi^2(v_0^2 + \sigma_v^2)\tau^2 + 2D(1 - \phi)\tau + 2\epsilon^2, \quad (8.12)$$

where the offset $2\epsilon^2$ related to the tracking precision and image acquisition has been added again. Because the MSD has a linear dependence on the diffusion coefficient, a distribution in the diffusion coefficients does not affect the equation. For a small variance in speed relative to the mean, Equation 8.12 reduces to Eq. 8.10. Equation 8.12 is identical to stated in the last section.

If the mean speed and standard deviation are known, the parameters D and ϕ can be calculated from a parabolic fit, $\text{MSD} = A^2\tau^2 + B\tau + C$, to the overall MSD (Figure 8.8) by the following relations

$$D = \frac{B/2}{1 - \frac{A}{\sqrt{v_0^2 + \sigma_v^2}}} \quad (8.13)$$

and

$$\phi = \frac{A}{\sqrt{v_0^2 + \sigma_v^2}}. \quad (8.14)$$

8.4. SCI analysis of POK2₁₋₅₈₉-GFP

The speed-correlation-index (SCI) analysis was used to complement the MSD-analysis of the single-POK2 motor trajectories and to discern and complement the motility switches [159]. It relies on the temporal correlations of the speed of individual molecules. This correlation exists and persists for directed motion but disappears for Brownian motion. The data acquired from single-molecule tracking experiments was used for the SCI analysis.

A MATLAB script was written Dr. Michael Bugiel to analyse the trajectory of each molecule. This script calculates the speed of single POK2 molecules and the correlations in certain time windows. The SCI parameter is a normalised average over an optimal time window, which provides a local analysis whether speeds are correlated or not. In particular, the switch times between diffusive and directed segments were analysed by defining a threshold for temporal correlations. The SCI analysis cannot distinguish between diffusive and stationary events. Thus, the latter was identified by comparing the root-mean-squared positional noise σ_x of the segments with that of stationary motors taken from immotile POK2 bound to microtubules. For a threshold of $\sigma_x < 32$ nm, segments were classified as being stationary.

For the experimental frame time of 0.1 s, a window size of 4 data points with an SCI threshold of 0.8 was used. From 113 original POK2 trajectories, 95 traces were long enough for the SCI analysis. The algorithm found 65 diffusive, 114 directed, and 21 stationary segments. The relative time POK2 spent in the diffusive, directed, and stationary mode were 29%, 63% and 8%, respectively. All diffusive and directed segments are shown in Figure 8.9b and c, respectively. The mean duration of the diffusive and directed segments were 0.8 ± 0.1 s and 1.1 ± 0.1 s, respectively (Figure 8.9d,e). The mean speed and standard deviation of directed segments weighted by their number of data points was 430 ± 170 nm/s (Figure 8.9). A Shapiro-Wilk test confirmed a normal distribution of speeds.

A MSD analysis of only the diffusive segments yielded a diffusion coefficient of $0.015 \pm 0.001 \mu\text{m}^2/\text{s}$ (Figure 8.10a). However, the mean displacements of diffusive segments still showed a significant bias over time (Figure 8.10b). Such a bias is inconsistent with pure diffusion and indicates that the SCI analysis did not fully separate directed and diffusive segments. This bias remained for all tested combinations of SCI parameters, i.e. variations

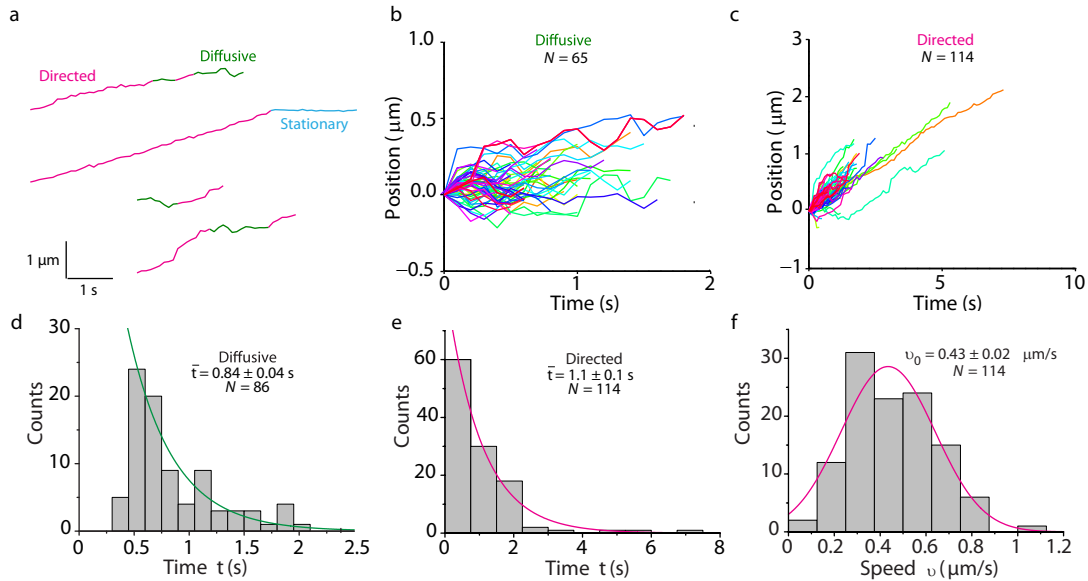


Figure 8.9.: SCI analysis can faithfully distinguish motility switches. (a) Example traces of few POK2₁₋₅₈₉-GFP trajectories for better visulation. Trajectories of (b) all diffusive and (c) all directed segments from tracked single POK2₁₋₅₈₉-GFP molecules. All segments are offset such that they start at zero. Time distributions for (d) diffusive and (e) directed segments single exponentials are plotted as a guide to the eye). (f) speed histogram of directed segments has a Gaussian distribution (magenta line). Mean speed, \pm SE and number of molecules are indicated. The figure is modified from [148].

of window size and thresholds. Thus, the time resolution and tracking precision was not sufficient for the segmentation. Therefore, it was concluded that POK2 sometimes switched between modes faster or on time scales comparable to the data acquisition time. An observation consistent with this conclusion is the lack of short diffusive segments due to the SCI algorithm when comparing the distribution to the expected exponential distribution (Figure 8.10). Apart from the cut-off at short times, segments containing very short periods of directed and diffusive motion are identified as diffusive segments by the algorithm. As a consequence, the diffusion coefficient obtained from the MSD analysis of the diffusive segments is underestimated because during short directed periods, the motor takes far fewer steps compared to when it is in its diffusive mode (see Section 8.3.1). Yet, it is expected that long directed segments and their parameters are reliably detected. One indication for reliable directed parameters, is that the speed was normally distributed. The mean speed also corresponds to the mean speed that one obtains by manually analysing the slopes of the kymographs. Thus, Eqs. 8.13 and 8.14 can be used to determine the diffusion constant D and relative time in the directed mode ϕ . The derivation of Eq. 8.12 did not account for the possibility of a stationary state. However, such a state only adds a constant to the MSD and is effectively adsorbed in the constant parameter. Thus, using Eq. 8.13, the diffusion constant was calculated to be $0.056 \pm 0.008 \mu\text{m}^2/\text{s}$ and, using Eq. 8.14, the relative time in the directed state excluding stationary segments was determined to be $62 \pm 2\%$.

To assess how the diffusion coefficient and speed depends on the relative time spent in the states, Eq. 8.13 as a function of the effective speed (Figure 8.10c) was plotted. Not accounting for the standard deviation in speed of 170 nm/s, changes the time fraction to about 67% with

an increase in the diffusion coefficient of about 10%. The equation is expected to slightly underestimate the speed because the SCI algorithm misses short diffusive segments. In this case, ϕ -values might be higher and the diffusion coefficient lower. Because the parameters fell into the range of effective speeds, for which Eq. 8.13 flattens out, it was not expected a large difference in the true diffusion coefficient of the motor.

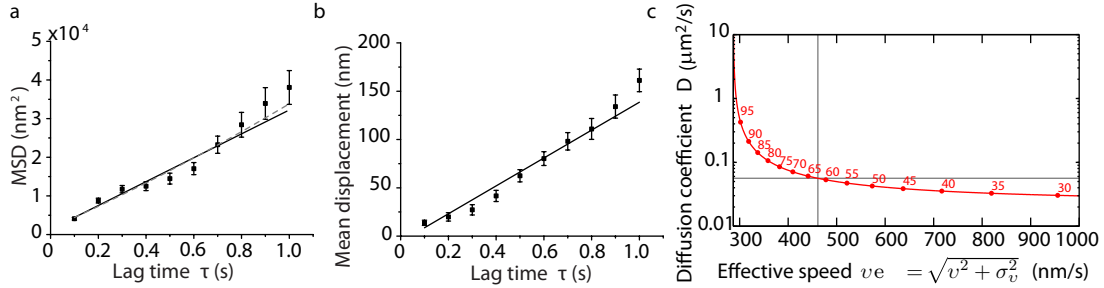


Figure 8.10.: System validation for POK2₁₋₅₈₉-GFP diffusive trajectories. (a-b) represent bias in the POK2₁₋₅₈₉-GFP diffusive segments. Mean-squared displacement (MSD) and (b) mean displacement versus time lag τ for diffusive segments (mean \pm SEM). A linear fit (black line) in (a) resulted in a diffusion coefficient of $0.015 \pm 0.001 \mu m^2/s$. A parabolic fit (grey dashed line) did not result in a significant speed. A linear fit (black line) in (b) resulted in a directed bias of $140 \pm 10 nm/s$. All fits were weighted by the error bars. (c) Relation between diffusion coefficient and effective speed. Dependence of the diffusion coefficient on the effective speed according to Eq. 8.13 (red line) for a set of fit parameters resulting from a parabolic fit to the MSD relation. Specific directed-mode time fractions ϕ (Eq. 8.14) are indicated by the red circles and numbers. Grey lines indicate the values for POK2₁₋₅₈₉-GFP. The figure is modified from [148].

In summary, the novel MSD equation Eq. 8.1, complemented with the SCI analysis provides a robust and quantitative understanding of single POK2 motor behaviour, on the microtubule lattice. The approach enabled identification of the motility switches and a reliable quantification of the separated trajectories that may otherwise cause errors in motility parameters. The diffusion constant was calculated to be $0.056 \pm 0.008 \mu m^2/s$ and the motor spends roughly 60% of its time on the microtubule undergoing an ATP-dependent processive motion.

Having observed diffusive character of POK2₁₈₃₋₅₈₉-GFP on the microtubule in the kymographs, these molecules were also tracked and processed in an identical pipeline. In contrast to POK2₁₋₅₈₉-GFP, the Nt_e truncation MSD was best fit by a line (green line in Figure 8.8c) with no significant parabolic coefficient. Thus, the truncation of the Nt_e switched POK2 to a purely diffusive mode with a diffusion coefficient of $0.040 \pm 0.001 \mu m^2/s$ not significantly different from the value for POK2₁₋₅₈₉-GFP.

8.5. POK2₁₋₅₈₉-GFP is a weak motor

The previous two sections established that POK2₁₋₅₈₉-GFP spends about two-thirds of its time in the processive manner, walking in a directed state along the microtubules. Moreover, the Nt_e of POK2 might enable efficient capturing of microtubules. *In vivo*, POK2 molecules that are present at the division site, might capture peripheral microtubules reaching towards

them from the leading edge of the phragmoplast. Since motors spend more time in an ATP-dependent processive state, they might be able to do some work in the form of pushing or pulling, depending on the polarity of the microtubules.

To assess if POK2₁₋₅₈₉-GFP molecules can bear loads, force measurements were conducted on a custom built optical-tweezers setup [140, 160]. An artificial cargo in the form of a microsphere was coupled to POK2₁₋₅₈₉-GFP via an anti-GFP antibody, ensuring functional activity of the motor (Figure 8.11) [39]. This motor coupled to the cargo was trapped and displaced the microsphere from centre of the trap in the presence of ATP (Figure 8.11a). Under such conditions, the trap behaves like Hookean spring, i.e, the motor displaces the microsphere with a force proportional to the displacement. In contrast to conventional kinesin, POK2₁₋₅₈₉-GFP did not exhibit a stalling behaviour for extended periods [39] (Figure 8.11b). Rather motor-coupled microspheres showed sudden and fast movements back to the trap centre. This observation is consistent with the motor detachment from the microtubule or switching into a diffusive state and slipping back on the microtubule [44, 161]. The maximum force before such events occur was measured. An average maximal force of 0.34 ± 0.02 pN (mean \pm SE, $N = 67$) was measured (Figure 8.11b). Since the motor without the long N-terminus did not show any directed motion, no force measurements were performed. Interestingly, despite the fact that POK2₁₋₅₈₉-GFP spends most of its time in a directed manner, the motor was unable to generate large forces. However, under multimotor conditions, the motors were able to generate forces exceeding 1 pN (Figure 8.11). Irrespective of the number of motors, such weak force generation by a kinesin motor is unusual. Compared to kinesin-1 with a stall force of 5–6 pN [39], POK2₁₋₅₈₉-GFP is one of the weakest kinesin reported so far. Reported weak motors belong to the kinesin-8 family with the members Kif18B, Kif18A, and Kip3 reaching maximum forces of about 0.6 pN, 0.8 pN and 1.1 pN, respectively [150, 161]. For POK2₁₋₅₈₉, such low forces can be attributed to the motor switching to a diffusive state similar to Kip3 that switches into a slip state [161]. Since motors are weakly bound to the microtubules in the diffusive state, they can slide along the microtubule lattice with little resistance, but without detachment when a force is applied [44, 144, 161]. Thus, the function of the diffusive state and low force production could be to provide a means of attachment to microtubules allowing for a relative sliding motion with little resistance. Interestingly, quite recently its human counterpart, Kif15 has been reported to stall and exert forces up to 6 pN (as tetramer) or 2 pN (as dimer) [162, 163]. Kif15 detached quickly under assisting loads, despite being locked in an AMP-PNP state [162]. This suggests a non-canonical stepping behaviour on the microtubule lattice. Moreover, *Arabidopsis* orphan kinesin PAKRP2 has recently been shown to undergo unconventional stepping behaviour [47]. Therefore, it would be interesting to see how POK2 steps on the microtubule lattice. However, currently the spatial precision under these low forces is insufficient to resolve steps.

Although the minimal POK2 motor construct is enough to establish the intrinsic mechanism of the kinesin, the enormous tail domain might have regulatory functions. There are certain obvious questions that prevail such as if the full-length POK2 would still be a weak motor or whether POK2 would be motile at all? Would it still switch motility modes? Would it be able to form higher order oligomeric states as observed for hKif15 [52]? Force exerted by the kinesins is assumed to be not altered, for example, minimal kinesin-1 as well as full-length kinesin-1 have the same maximum (5–6 pN). The maximum force is thought to be determined by the intrinsic behaviour of the motorheads. Thus, it is assumed that full-length POK2 is still a weak motor. To investigate how the full-length POK2 behaves, several

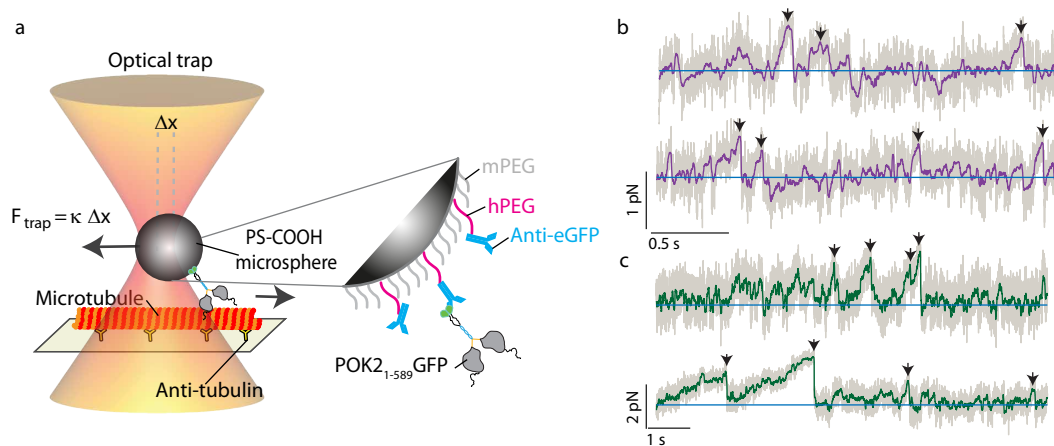


Figure 8.11.: POK2_{1–589}-GFP is a weak motor. (a) Schematic representation of the force measurement. (b) Representative traces depicting the force of single POK2_{1–589}-GFP molecules as a function of time (grey line, running median filter over 500 data points: purple line). The blue line marks zero force. Maximal forces are marked by black arrows. (c) Force traces under multi-motor conditions. Force traces of microspheres powered by multiple POK2_{1–589}-GFP as a function of time. A 10× higher incubation concentration of POK2_{1–589}-GFP with microspheres was used compared to the single-molecule assays resulting in the motility of 5 out of 6 microspheres. The blue line marks zero force. Arrow heads point to the maximum force prior to detachment events. The figure is modified from [148].

attempts were made to clone POK2. There were two hurdles. First, it was difficult to get the full-length cDNA of POK2 (8.4 Kb) from an already impoverished pool of POK2 mRNA. Second, it was hard to clone in a bacterial-compatible vector for downstream processing. Both of these tasks were attempted. The attempts to get POK2 cDNA included overlapping PCRs, Gibson assembly or Infusion techniques that are both based on recombineering, and single-stretch PCRs. Eventually, it was possible to get the full-length POK2 cDNA, however, the prime difficulty was their compatibility in bacteria. Every bacterial transformation failed. This might suggest some cryptic promoter or toxic sequence, most likely present in the middle part of the POK2 cDNA. This special sequence might be recognized as a threat and initiate self-destructive signalling in bacteria. Such a scenario might explain absence of colonies when compared to the control transformation. A reasonable approach would therefore be, to commercially synthesize POK2 cDNA right into an insect cell vector that can be used directly to transfect the insect cells with the bacmid. This would avoid the bacterial step completely, however, to what extent this might work is still questionable. Having said that, POK2 as genomic DNA was successfully cloned by Dr. Sabine Müller's group and, recently, they reported that full-length POK2 is motile *in planta* [92]. Yet, the operating mechanism of full-length POK2 remains highly fascinating due to its colossal size.

8.6. POK1_{1–564}-GFP is a plus-end-directed motor

POK1 and POK2 redundantly maintain the division site memory in *Arabidopsis* [91]. In the previous sections, the POK2 motor domain has been characterized. In the following sections, a minimal construct of POK1 is analysed in analogy to POK2, to understand its role in phragmoplast guidance mechanism.

To understand the motor characteristics, POK1₁₋₅₆₄-GFP (Figure 8.12a-c) was cloned and expressed by Maja Reißner, a former master student in our laboratory. Using rhodamine-labelled and taxol-stabilized microtubules immobilized on the surface and in the presence of 1 mM ATP, she had reported immobile behaviour of the POK1 motor domain. To reason this behaviour, the motility conditions of POK1₁₋₅₆₄-GFP were optimized. Ultimately, it was found that POK1₁₋₅₆₄-GFP is a rather sensitive motor that easily degrades. Therefore, all motility assays were performed as fast as possible once the purified protein was added.

Under optimized motility conditions, it was observed that POK1₁₋₅₆₄-GFP also robustly translocated on the microtubule lattice (Figure 8.12d-f). To discern the polarity, POK1₁₋₅₆₄-GFP was flushed onto polarity-marked microtubules. It was found that on average POK1₁₋₅₆₄-GFP moved towards the plus-end of the microtubules (Figure 8.12f). This result is in accordance with the POK2 and kinesins with N-terminally located motor domains. Interestingly, POK1 stayed at the microtubule ends for short periods. The oligomeric state of the POK1₁₋₅₆₄-GFP could not be determined due to limited amounts of purified protein. It is assumed that POK1 also forms dimer similar to the POK2 motor domain. The coiled coil-dimerisation observations, data for the POK2 motor domain, and native gels support this hypothesis.

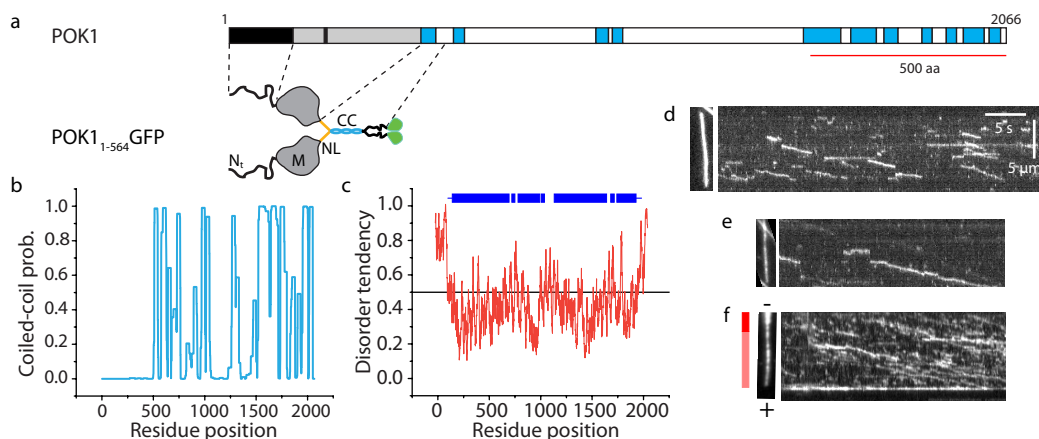


Figure 8.12.: POK1₁₋₅₆₄-GFP is a plus-end-directed motor. (a) Structural cartoon representation of the POK1₁₋₅₆₄-GFP used for *in vitro* experiments in comparison to the full length POK1. (b) Predicted coiled-coil probability plot for POK1. (c) Disordered tendency index for POK1 based on the pair wise amino acid energy content (red line). The blue bars represent globular/structured regions, while the black line indicated the threshold (d-e) Kymographs representing POK1₁₋₅₆₄-GFP motility on the microtubules shown on the left. (f) Polarity-marked microtubule displaying POK1₁₋₅₆₄-GFP motility towards microtubule plus-ends. The schematic on the left indicates dark red as the nucleating end and dim red as the growing microtubule end.

POK1 is also a large kinesin, however a bit smaller than POK2. Full-length POK1 cDNA was cloned by Caroline Wall in Dr. Sabine Müller's group. The purification of POK1 full-length might answer some of the questions already posed for the POK2 (Section 8.5). As POK1 and POK2 act redundantly on the division site during mitosis and cytokinesis, insights into the operating mechanisms of one full-length motor might provide understanding of the phragmoplast guidance mechanism. To this end, the full-length POK1 was expressed in insect cells and purified using sequential chromatography (Figure 8.13). Unfortunately, on

independent expression cycles, it was observed that the protein did express but clusters inside insect cells. Upon purification and analysing the protein fractions on SDS-PAGE gels it was observed that the POK1 protein was cleaved (Figure 8.13b-c). There might be problems in either proper protein folding, or the protein is toxic to the cells, leading to its degradation. This observation also demonstrates the challenges faced in obtaining a full-length POK molecule, probably due to a difficult sequence organisation. Therefore, further experiments and data analysis were carried out using POK1₁₋₅₆₄-GFP construct.

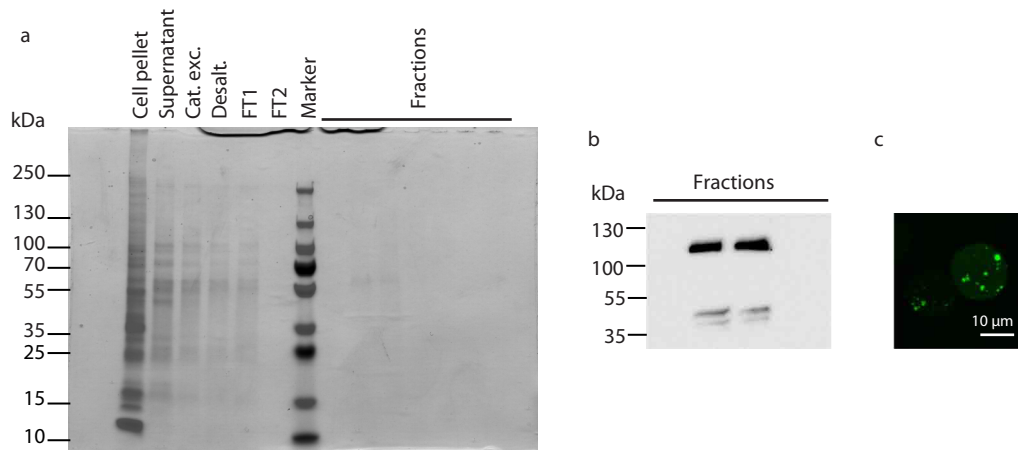


Figure 8.13.: Purification trials of POK1 full-length. (a) Coomassie stained 4–20% Tris-Glycine SDS-PAGE gel showing the protein fraction after the purification. (b) The anti-GFP western blot detects the protein at the wrong size and partially degraded. (c) Fluorescence image of insect cells expressing full-length POK1 shows inclusion-like bodies or aggregates instead of expected cytoplasmic green fluorescence. Cat. exc.: cation exchange, Desalt: desalting, FT: flow-through.

8.7. POK1₁₋₅₆₄-GFP also switches motility modes

The kymograph analysis of POK1₁₋₅₆₄-GFP showed that it is also capable of switching between processive and diffusive modes (Figure 8.12). This observation was not as prominent for POK1₁₋₅₆₄-GFP as it was for POK2₁₋₅₈₉-GFP. However, in a manner similar to POK2 motor, the single-POK1 molecules were tracked on individual microtubules using an automated data analysis. The data obtained from tracking was analysed by the new MSD analysis (see Equation 8.1). The mean interaction time for POK1₁₋₅₆₄-GFP, 2.06 ± 0.07 s (mean \pm SE) on the microtubule lattice was similar to the observed interaction time for POK2₁₋₅₈₉-GFP of 1.9 ± 0.1 s (Figure 8.14a, Figure 8.8). The observed mean speed was 260 ± 9 nm/s, which is about half the observed speed for POK2₁₋₅₈₉-GFP, 430 ± 30 nm/s (Figure 8.14b, Figure 8.9). The mean-squared analysis of the POK1₁₋₅₆₄-GFP was also best fitted by a parabola with significant contributions from processive and diffusive modes. The diffusion coefficient was calculated as per equation 8.1 for POK2₁₋₅₈₉-GFP, was $0.059 \pm 0.002 \mu\text{m}^2/\text{s}$, compared to $0.056 \pm 0.006 \mu\text{m}^2/\text{s}$ for POK2₁₋₅₈₉-GFP. The relative time spent by the motor in the directed state ϕ was about 0.81 ± 0.02 , which is also consistent with estimate based on the kymographs. The error in ϕ and D was calculated

from by error propagation. Thus, POK1₁₋₅₆₄-GFP spends about 80 % of its time in the processive mode, but with a comparable diffusion coefficient to POK2₁₋₅₈₉-GFP.

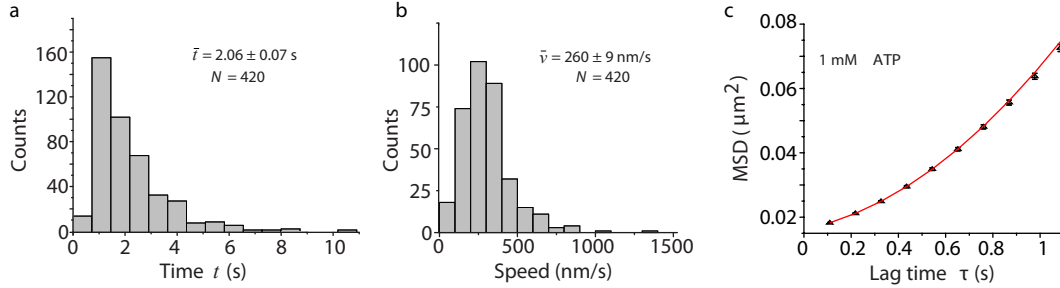


Figure 8.14.: POK1₁₋₅₆₄-GFP also switch motility modes. Distributions of total interaction time (a) and speed for selected trajectories (b) of POK1₁₋₅₆₄-GFP on the microtubule lattice are shown. Mean values \pm SE and total number of molecules are indicated. (c) The mean-squared-displacement (MSD) of POK1₁₋₅₈₉ in 1 mM ATP plotted against the lag time is shown. The red line is a parabolic fit to the POK1₁₋₅₆₄-GFP data. The error bars are SE of squared-displacement values.

Table 8.15.: Comparative summary of POK1 and POK2 motility quantification

<i>Kinesin motor</i>	v	t	D	ϕ
POK2	430 ± 30 nm/s	1.9 ± 0.1 s	0.056 ± 0.006 $\mu\text{m}^2/\text{s}$	60 %
POK1	260 ± 9 nm/s	2.06 ± 0.07 s	0.059 ± 0.002 $\mu\text{m}^2/\text{s}$	81 %

8.8. Multiple POK1₁₋₅₆₄-GFP motors generate higher forces than multiple POK2₁₋₅₈₉-GFP

POK2₁₋₅₈₉-GFP was observed to be the weakest kinesin motor known. However, multiple motors together were capable of generating forces more than 1 pN. To investigate the force generation of POK1₁₋₅₆₄-GFP, it was coupled to the anti-GFP nanobody coated microspheres (Figure 8.16a). Similar to POK2, it was observed that POK1 motors did not exhibit stalling behaviour, but detached from the microtubule after processive motion and snapped back to the trap centre. Interestingly, under multi-motor conditions, on average forces up to 10 pN were observed (Figure 8.16b). The forces are about 10 times higher compared to the ones recorded under POK2₁₋₅₈₉-GFP multi-motor conditions (Figure 8.16b, Figure 8.11b). The high forces could be attributed to the different protein-microsphere coupling—anti-GFP nanobody instead of an antibody. Due to limited amounts of proteins, single-molecule force measurements could not be performed, yet it appears as if forces are higher than those of POK2 motors. These observations are interesting and raise the question of what makes them different, albeit siblings of the same kinesin family and functionally redundant.

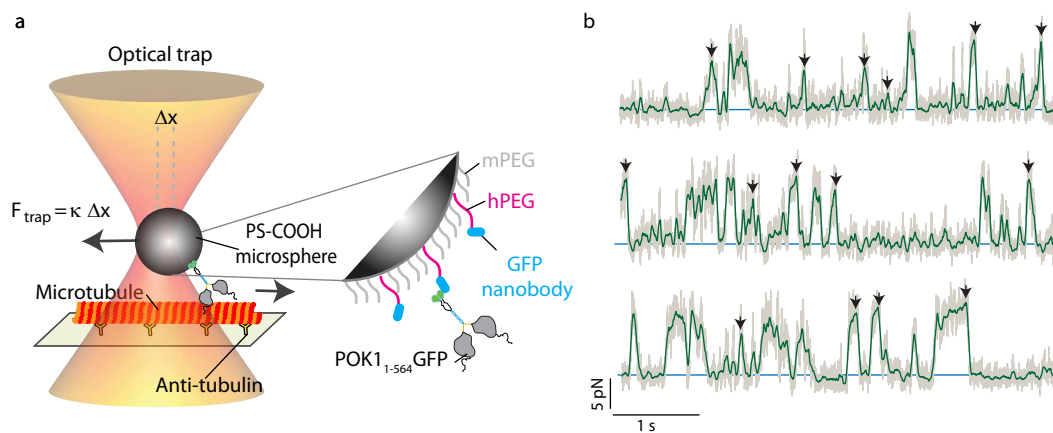


Figure 8.16.: Multiple POK1₁₋₅₆₄-GFP generate high forces. (a) Schematic representation of the force measurement. (b) Representative traces depicting the force of POK1₁₋₅₆₄-GFP molecules as a function of time (grey line, running median filter over 500 data points: green line). The blue line marks zero force. Maximal forces are marked by black arrows.

8.9. Plus-ends of peripheral microtubules point towards the division site

The preceding sections demonstrate that POK1 and POK2 are active, plus-end-directed motors. This finding was also validated for POK2 *in vivo* by Dr. Sabine Müller's group [92]. This leads to speculation that active POK1 and POK2 might arrive at the division site in a microtubule-dependent manner. Since the recruitment time and spatial extent of these POKs overlaps with that of the preprophase band, recruitment is presumed to be PPB dependent. POKs might anchor themselves at the division site by interacting with adaptor (peripheral or transmembrane) proteins or via direct interaction with lipids or both. The long tail domain of POKs might facilitate or regulate this division site anchoring. Assuming that the motor-heads are protruding from the division site, how do these POKs then guide the phragmoplast that is expanding towards the division site?

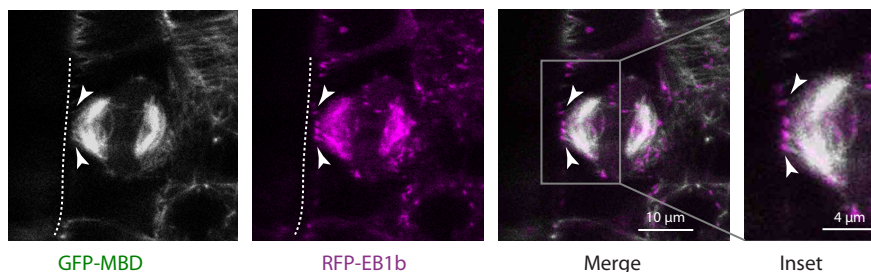


Figure 8.17.: Directionality of the phragmoplast peripheral microtubules. *Arabidopsis* root meristem stably expressing 35S:GFP-MBD and pUBQ:RFPEB1b during late cytokinesis. Plus-ends (RFP-EB1b) marked with arrow heads of peripheral microtubules (GFP-MBD) from the leading edge of the phragmoplast reach out towards the putative division site. The cell boundary is marked with a dashed line. MBD: microtubule binding domain. The figure is modified from [148].

Recent studies have highlighted the presence of peripheral microtubules that emanate from the leading edge of the phragmoplast [89, 91, 164]. Based on this observation, one hypothesis is that POKs at the division site might catch these peripheral microtubules and apply forces to orient the expanding cell plate towards the correct destination. To understand how this molecular mechanism of orienting the cell plate might work, it is instructive to know the polarity of the peripheral microtubules. The majority of microtubules facing the division site including the ones at the leading edge of the phragmoplast suggests that these peripheral microtubules might face the division site with their plus-ends. Two studies based in tobacco and moss do demonstrate the polarity of peripheral microtubules [94, 164], however, a direct proof with a substantial resolution has been missing in *Arabidopsis*. To confirm that, an *Arabidopsis* transgenic line was created with GFP-labelled microtubules and RFP-labelled Eb1—a microtubule +TIP. 4–5 day old seedlings were imaged on a confocal microscope. It was found that the leading edge of the phragmoplast indeed sends out peripheral microtubules with their plus-ends pointing towards the division site (Figure 8.17). However, the presence of plus-ends does not rule out the presence of minus-ends of microtubules in the vicinity. Yet, based on these observations and overall structure of the phragmoplast it is assumed that there is not much abundance of minus-end microtubules facing the division site (Figure 2.3). This polarity suggests that POK1 and POK2 push against the peripheral microtubules approaching the division site.

8.10. Pushing model for the phragmoplast guidance

The *in vitro* and *in vivo* data gathered in this thesis support a phragmoplast guidance model for accurate cell plate insertion during plant cytokinesis. The phragmoplast guidance model is based on pushing forces, in which POK2 and POK1 localized at the division site push against the peripheral microtubules of the expanding phragmoplast.

As the disk-shaped phragmoplast expands centrifugally with the maturing cell plate in the centre, the leading edge of the phragmoplast sends out microtubules facing the division site (Figure 8.18). The Eb1-microtubule localisation experiments in the root meristem of *Arabidopsis* during late phragmoplast stages demonstrate this event. The peripheral microtubules from the leading edge certainly have microtubule +TIPs at their growing ends. As mentioned in the introduction, +TIPs enable the binding of several other MAPs to form networks that execute various functions such as signalling, microtubule guidance and attachment to cellular substrates. Here, POK2 and POK1 molecules are present at the division site as cellular substrates (Figure 8.18). Assuming that these peripheral microtubules probe the cortex with their growing-ends, POK molecules may capture them. The long N-terminus of POK molecules might assist in efficient capture of the microtubules by enhancing microtubule affinity and processivity. The capturing ability of POKs might also be strengthened by their enormous size and contour length. Upon capture, they being plus-end-directed motors, walk towards microtubule growing ends in an ATP-dependent processive mode.

As POKs walk towards the microtubule plus-ends, microtubules are pushed away from the division site with their minus-ends pushing against the expanding phragmoplast (Figure 8.18). Pushing may seem counter-intuitive for phragmoplast guidance but together with the unusual mechanics of these kinesin-12 motors provide insight into the guidance mechanism. As POK2_{1–589} and POK1_{1–564} motors exert little force, forces of the expanding phragmoplast

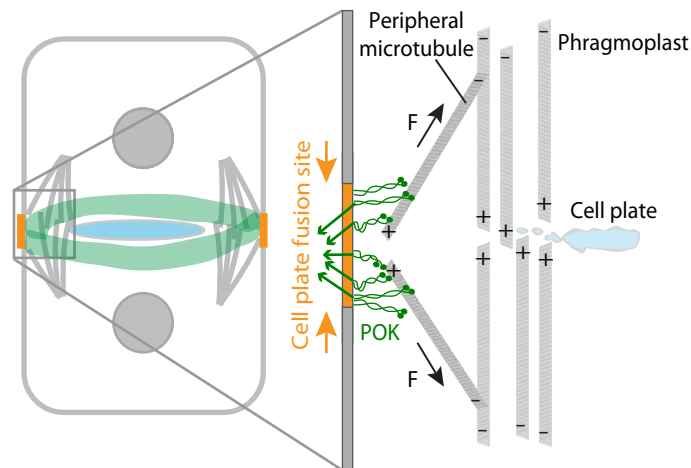


Figure 8.18.: Proposed model for phragmoplast guidance. POK motors (green) localized at the division site push against the leading edge of the expanding phragmoplast by capturing the peripheral microtubules and walking towards their plus-ends. The black arrow marks the direction of the pushing force. This model also supports the narrowing of the division site (orange) to the cell plate fusion site by a mechanical process. POK motors experience a counter force (green arrows). This force focusses the POKs to a precise spot, i.e., the cell plate fusion site. The figure is modified from [148].

likely exceed the opposing pushing force of POK motors when they are in the processive state. Once the motors switch to the diffusive state, they can then slide along the microtubule lattice without detachment. The switching rate to the diffusive mode of the motors may even increase under load conditions as previously demonstrated for kinesin-8 Kip3 [161].

Such dynamic linking of kinesins with the growing microtubules during cell plate orientation draws interesting parallels with the microtubule attachment to the kinetochores ensuring appropriate alignment and splitting of chromosomes at the metaphase plate. Kinesin-7 CENP-E, another huge kinesin molecule, whose size is comparable to the POKs, especially POK2. Looking into the molecular structure, it also possess an N-terminally located motor and an extended coiled-coil tail domain. This kinesin is part of a huge protein complex present at the kinetochores and can form heterodimers. It has been shown that such a molecular structure creates a 230 nm rod-like structure with globular domains in the end [18]. With the motor domains towards the microtubule growing ends, this kinesin dynamically links microtubules via diffusive attachments [165–167]. Since hKif is shown to form tetramers, POK2 and POK1 could form tetramers or heterodimers [52]. However, an answer to this question will require full-length molecules as oligomerization might be mediated by their coiled-coils tails.

Given the data here, the proposed pushing model for the phragmoplast has reasonable implications. According to Newton’s third law, pushing forces by POKs, even though small, have an important consequence. There is a net force of equal magnitude and opposite direction acting on the anchoring points of the motors. Furthermore, due to the geometry of the connected peripheral microtubules, these opposing forces will focus the motors to a central spot, assuming that their membrane anchors are mobile within the lipid bilayer (Figure 8.19). The small forces of a single motor are sufficient to drag an anchoring point through a fluid membrane. Also, when multiple motors interact simultaneously with a

microtubule, the pushing forces of the expanding phragmoplast and counteracting motor forces are expected to be sufficient for moving the anchoring points in the membrane. This mechanical focusing could explain the poorly understood narrowing of POKs and POK-dependent components from the division site to a definite cell plate fusion site during late cytokinesis [86, 89, 91, 168]. Whether POK motor motility itself is required for *in planta* guidance, whether a diffusive tethering is sufficient, how motors switch to the diffusive state, and if and how much force is necessary for division site narrowing are unknown at the moment.

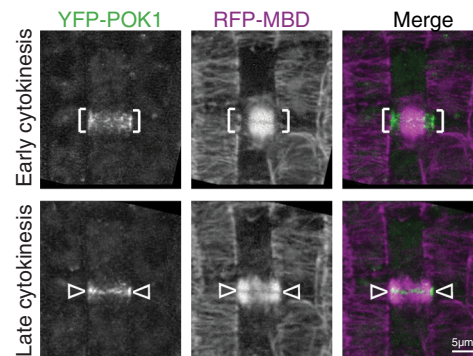


Figure 8.19.: Narrowing of the division site. *Arabidopsis* root meristem expressing YFP-POK1 and RFP-MBD indicating narrowing of the division site from early cytokinesis to the presumably cell plate fusion site during late cytokinesis. For experimental details see reference [91]. The figure is modified from [148].

8.11. Implications of the pushing model for the phragmoplast guidance

The accurate insertion of the cell plate at the division site or rather the cell plate fusion site is brought about by proper guidance of the phragmoplast to that site. The data presented in this thesis suggests a plausible pushing model of phragmoplast guidance by POK1 and POK2 localized at the division site. This model also provides mechanistic insights into the mysterious narrowing of the division site towards late cytokinesis, which has been previously observed many times but remains unexplained. Although pushing forces are a surprising phenomenon, but they exist in many positioning situations inside cells. However, if cellular forces for intracellular positioning and self-organisation are pulling, pushing, or sliding depends on the symmetry, geometry, and distances [14]. Pushing forces are considered more efficient for movements over small distances and centring of organelles in symmetric geometries [14]. Proper spindle alignment in *S. pombe*, for example, occurs by astral microtubules that push against the cell surfaces. The mitotic spindle itself is a stunning example of pushing forces. Apart from CENP-E, chromokinesin Kid bound at the chromosome arms, push against the microtubules by walking towards their plus-ends, which face away from the spindle pole, contributing to "polar ejection forces" that push the chromosomes away for proper alignment [14].

In the current scenario of the division site, POKs share the region with the kinesin-14 member KCBP. Kinesin-14 members are minus-end-directed kinesins. Although KCBP motility has not been shown in *Arabidopsis* or in *in vitro* experiments, it can still be assumed, that KCBP pulls on peripheral microtubules, thus supporting a pulling model for phragmoplast guidance (Figure 8.20). KCBP mutants do not show misaligned cell walls but this could be due to functional redundancy exhibited by unidentified kinesin-14 members at the division site. Therefore, it is reasonable to assume that in such a case, the phragmoplast might be guided to the division site as a virtue of push-pull forces or a tug-of-war mechanism (Figure 8.20).

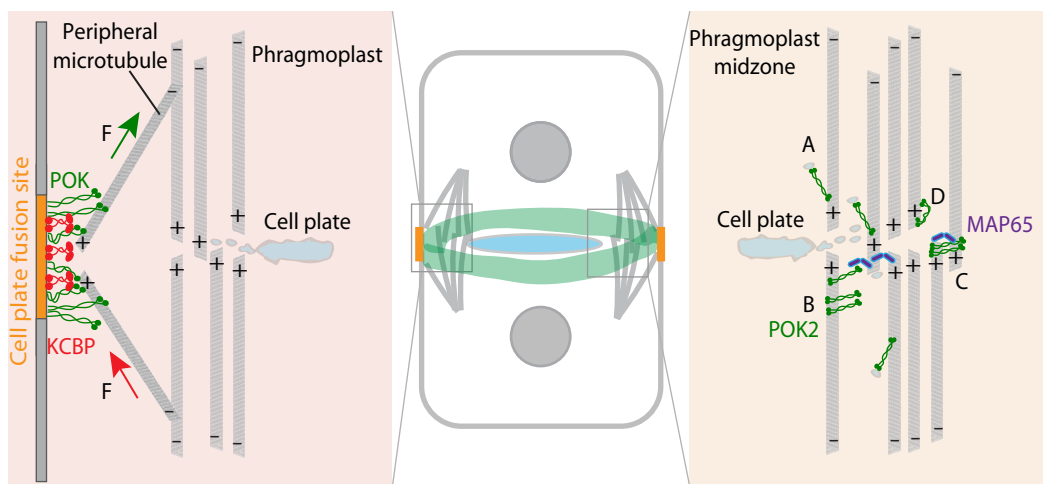


Figure 8.20.: Possible roles of POKs during cytokinesis. *Left* Possible tug-of-war mechanism mediated phragmoplast guidance to the cell plate fusion site. POKs (green) and kinesin-14/KCBP (red) both localize at the division site and might interact with the peripheral microtubules with opposite polarity, thus, enabling a push-pull mechanism for accurate cell plate insertion. *Right* Suggested roles of POK2 at the phragmoplast midzone based on this thesis and the current literature. (A) Transport of cytokinetic vesicles towards the cell division plane. (B) Parallel bundling of microtubules at the phragmoplast and interaction with MAP65-3. (c) Anti-parallel sliding or cross-linking of microtubules at the midzone and interaction with MAP65-3. (D) Regulation of microtubule plus-end dynamics.

The pushing model of phragmoplast guidance mediated by POKs in this thesis so far suggests the accurate insertion of the cell plate/cell wall at its destination. However, it is compelling to note that a recent study also showed POK2 being localized at the phragmoplast midzone apart from the division site [92]. Although, the POK2 interaction with MAP65-3 might support phragmoplast stability, the molecular mechanism is still unclear (Figure 8.20). Can POK2 when not anchored in the membrane form parallel bundles or promote anti-parallel microtubule sliding? Can POK2 transport vesicles towards the phragmoplast midzone? Being present only at the midzone and being a plus-end-directed motor, can POK2 regulate or alter the dynamics of the microtubule growing ends (Figure 8.20)? These questions require *in vitro* reconstituted assays with purified POK2 and dynamic microtubules.

It is doubtless that plant cytokinesis is propelled by microtubules. Interestingly, the role of actin during cytokinesis is undermined, possibly, due to the 'actin-depleted zone' that forms at the division site during mitosis. Since actin is also a part of the phragmoplast itself, its

dynamics and/or myosin motors might contribute to cytokinesis. Through this thesis, it is clear that the majority of the plus-ends of peripheral microtubules point towards the division site. Therefore, one might speculate that +TIPs with other MAPs might initiate signalling cascades, which alters local cytoskeletal dynamics in the vicinity of the division site. Of prime importance here is actin. The evidence that Ran GAP1 and PH-GAPs localize at the division site, indicate their presumptive role in actin remodelling [86, 89]. Recent studies have postulated the involvement of actin during late cytokinesis. Using *P. patens*, the involvement of Myosin VIII during phragmoplast guidance is suggested. If actin also contributes to phragmoplast guidance in *Arabidopsis* has not been investigated. However, the presence of Myosin XI at the division site, prior to cell plate insertion is worth mentioning as its loss leads to cell wall mispositioning [95]. Moreover, KCBP kinesin-14 that resides at the division site as well as phragmoplast microtubules contains a conserved myosin homology domain that binds F-actin [88]. Experiments also demonstrate that depolymerization of F-actin leads to misaligned cell walls and tilted phragmoplasts from the PPB predicted site. Together, it is apparent that accurate insertion of the cell walls requires an orchestrated interplay of motor proteins, microtubules, actin and their associated binding partners. Molecules that link both of these cytoskeletal elements together such as formins and specialized MAPs might provide exquisite insights into the cooperation mechanisms. Therefore, there is a need for such mining that will provide comprehensive understanding to plant cytokinesis and accurate cell wall positioning.

9. The POK2 tail contains a membrane binding domain and Xenosin—a new microtubule motor

The colossal size of phragmoplast orienting kinesins is very intriguing. This is because apart from the conserved motor domains, there are no obvious functional or globular domains located in the tail domain. Therefore, could this coiled-coil rich tail serve as a fishing rod to capture peripheral microtubules? Could the tail domain regulate the activity such as switching behaviour or force generation of the motor domains? Could this C-terminus serve as a scaffold for binding partners or signalling molecules? Or could it simply tether POKs to the division site membrane?

A recent study using a truncated POK2 C-terminal construct in *Arabidopsis* shows that POK2_{2083–2771}-GFP is enough for POK2 localisation at the division site and its maintenance there throughout mitosis and cytokinesis [92]. This study also demonstrates that POK2_{2083–2771}-GFP localisation at the division site is microtubule dependent. This result was also supported by faint localisation of POK2_{2083–2771}-GFP on cortical microtubules. Whether POK2_{2083–2771} interacts directly or via a binding partner with the microtubules is unclear. Once localized, POK2_{2083–2771}-GFP stays at the division site in a microtubule-independent manner. Moreover, POK2_{2083–2771}-GFP interacts with MAP65-3, very much like the N-terminal extension preceding the POK2 motor domain [92]. Together, these observations suggest that POK2_{2083–2771}-GFP might have a secondary microtubule binding site and either have an adaptor protein binding site or direct domain for interacting with lipids at the division site.

To get detailed insights, POK2_{2083–2771}-GFP was used as a model to discern the capabilities of the long C-terminus tails of POKs.

9.1. Bioinformatic analysis of the POK2 C-terminus

To investigate functions of the unannotated C-terminal tail of POK2, bioinformatics was used to identify domains using the protein sequence and structure similarity. The fasta sequence was retrieved from Uniprot [169]. Uniprot provides annotation of the motor domain and ATPase site and also the predicted coiled-coils. For robustness, manual annotation of coiled-coil prediction was conducted using P-coils and MARCOILS as mentioned in the previous chapter (Figure 8.1). Besides the basic annotation, there were no globular domains predicted. To address what could be the functionality of the coiled-coil regions after the motor domain, ELM (Eukaryotic Linear Motifs) was exploited. ELM is a computational biology resource that predicts functional motifs in a protein sequence based on the annotated/putative motif data and analytic tool for motif prediction. The ELM list curated for POK2 is long with

several interesting candidates such as motifs required for protein degradation (DEAD-box and KEN-box), signalling motifs (Protein kinase A, MAPK1) and two actin-binding sites (Figure 9.1). However, one has to be careful with predictions resource as it might result in over-prediction and, therefore, must be experimentally verified.

Motif	Sequence	Location
Actin binding site	ESQNTILIQEAVELRRI	937-953
Actin binding site	LAQELLSLCTSILKAA	2674-2689
KEN-box	SKENC	782-786
KEN-box	IKENY	953-957
KEN-box	KKENV	1963-1967
DEAD-box	LRASLLSLT	26-34
DEAD-box	SRKQLKSLE	614-622
DEAD-box	TRFALEWIR	716-724
DEAD-box	ARLFLEDIW	1631-1631
PKA	RRDSDNH	9-15

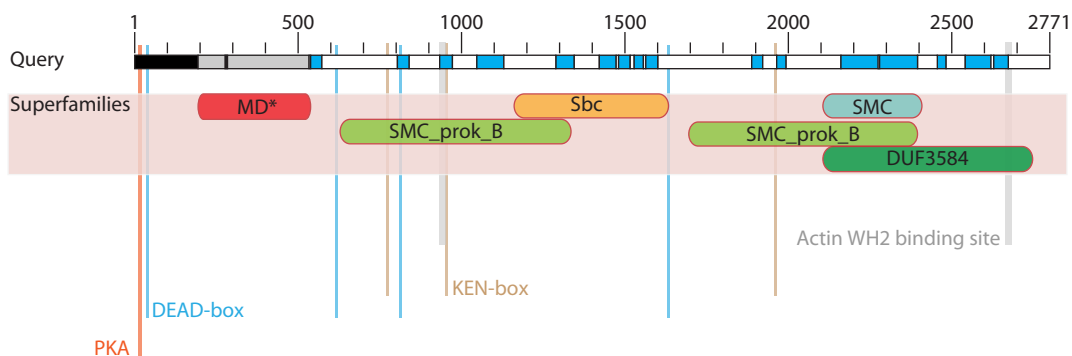


Figure 9.1.: Domain and motif analysis of POK2. Sequence analysis report of POK2 full-length with BLASTp and ELM [170, 171]. *Top* displays full-length POK2 with marked domains as presented in Figure 8.1. When used as query in BLASTp, the superfamilies that find specific and non-specific hits based on the sequence similarities are represented. * denotes the specific hit. Besides the superfamily similarities, selected ELM results are depicted as bars in the predicted regions in the protein sequence. The width of the bars represent the length of the motifs.

After the motif search, the entire sequence of POK2 was used for protein similarity search using non-redundant BLASTp. POK2 has most similarity with other kinesin-like proteins and many hypothetical kinesins in plants, presumably belonging to the kinesin-12 family. Interestingly, the sequence identity scores in these results were between 40–100% and the E-value was 0 or less. Apart from sequence hits, BLASTp also provides putative conserved domains and superfamily similarities. The specific hit in this category was kinesin motor domain and was clear (Figure 9.1). There were various non-specific hits in the tail region. These were domains that belong to the SmC superfamily (Structural maintenance of chromosomes) along the length of the tail (Figure 9.1) [172]. Towards the end of the protein sequence, the score for this domain is good. The SmC family, as the name suggests are responsible for DNA binding and members of this family such as condensin have been recently

shown to compact DNA into chromosomes during mitosis [173, 174]. These SmC proteins are conserved through bacteria and possess an ATPase domain [175]. Surprisingly, in the same region, another non-specific hit points to a conserved protein in bacteria and eukaryotes (Figure 9.1). This protein family, DUF3584, remains still elusive, however, possess a P-loop motif suggesting it is a nucleotide binding protein [72]. This bioinformatic analysis suggests that there might be some unconventional structural domains (globular or not) residing in the POK2 tail that may devise functional aspects to the tail.

It is interesting that none of the analyses above predict any membrane or microtubule binding domain as speculated based on the *in vivo* study [92]. Therefore, the best way to approach this problem was to devise experiments with the purified POK2_{2083–2771}-GFP and test its functionality.

9.2. POK2_{2083–2771}-GFP has a secondary microtubule binding site

To investigate if POK2_{2083–2771}-GFP interacts with the microtubule directly as postulated by the *in vivo* localisation. The POK2_{2083–2771}-GFP construct was provided by Dr. Sabine Müller's lab. This construct was expressed in yeast but purified in a similar manner to the POK motor domain constructs (Figure 9.2). Rhodamine-labelled, taxol-stabilized microtubules were immobilised on the coverglass surface as mentioned before and purified POK2_{2083–2771}-GFP was added. It was found that POK2_{2083–2771}-GFP co-localized with the microtubules, suggesting that POK2_{2083–2771}-GFP has a secondary microtubule binding site (Figure 9.3).

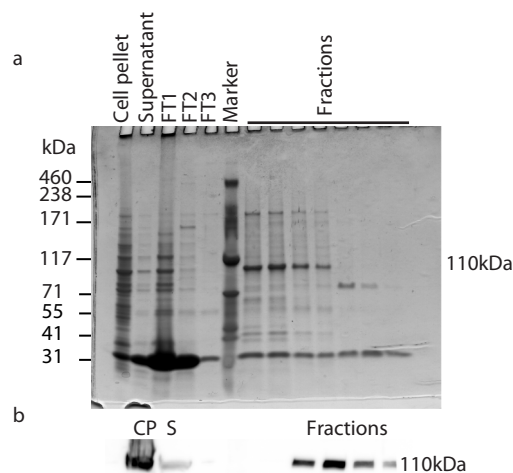


Figure 9.2.: Post-purification analysis of POK2_{2083–2771}-GFP. (a) Coomassie stained 4-20 % Tris-Glycine SDS-PAGE gel with protein purification fractions. (b) Anti-GFP western blot of the purification fractions detects the protein at right size, 110 kDa. CP: cell pellet, S: supernatant, FT: flow through.

This finding is very interesting as there are only a few known kinesins that carry a secondary microtubule-binding domain in their C-terminal tail. Kinesin-5, Kif15, and Chromokinesin Kid localize at spindle microtubules and are involved in proper spindle and chromosome alignment, respectively [13, 14, 51, 163]. These kinesins are shown to possess a non-motor

microtubule binding site in their tails that increases total microtubule affinity with the motor domain. This non-motor microtubule domain is insensitive to ATP or nucleotides but enables cross-linking or sliding of microtubules. Kinesin-8 Kif18A also localized at the mitotic spindle, is reported to regulate spindle length by its microtubule depolymerization ability [176]. Kif18A also possess an ATP-independent secondary microtubule binding domain in its tail region that affects the localisation of Kif18A at the microtubule plus-ends and therefore, its function. Interestingly, the presence of this additional microtubule binding does not affect motility in the above cases. In the case of Kif18A yeast homologue, Kip3, a second microtubule binding site increases processivity [177]. Excitingly enough, *Arabidopsis* kinesin-14 member KCBP, resident of the division site, harbours a nucleotide independent secondary microtubule binding site in its N-terminal tail [178]. This is fascinating because KCBP has a membrane binding domain that also sits in the N-terminal tail [88]. Thus, already two residents kinesin members of the division site possess a secondary microtubule binding site possibly to guide the expanding phragmoplast in an efficient manner.

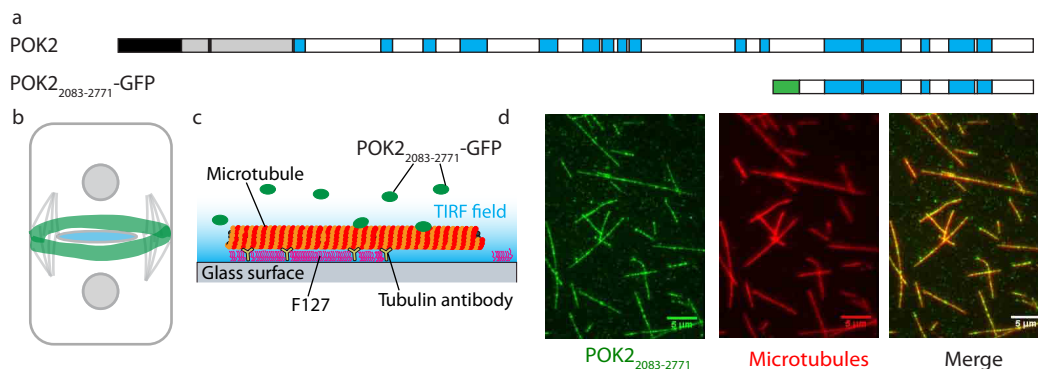


Figure 9.3.: POK2 C-terminus contains a secondary microtubule-binding site. (a) Schematic representation of the POK2_{2083–2771}-GFP construct relative to the full-length POK2. (b) *in vivo* localisation of POK2_{2083–2771}-GFP is marked in green. POK2_{2083–2771}-GFP localizes at the division site through mitosis and cytokinesis [92]. (c) Schematic of the *in vitro* experimental set up. (d) TIRF microscopy images depicting the co-localisation of POK2_{2083–2771}-GFP with the rhodamine-labelled microtubules.

9.3. POK2_{2083–2771}-GFP displays microtubule plus-end motility

The presence of a secondary-microtubule binding domain in the POK2 C-terminus along with the BLASTp derived SmC and DUF domain family similarity, suggest that POK2 tail-microtubule interaction might be nucleotide dependent. To investigate this dependence, an *in vitro* motility assay identical to the POK motor domains was set up. Purified POK2_{2083–2771}-GFP was flushed into the channels with immobilised and rhodamine-labelled microtubules in the presence of 1 mM ATP. Unexpectedly, it was found that POK2_{2083–2771}-GFP showed robust processive movements in a directional manner (Figure 9.4). Not all molecules showed processive motion. Some molecules landed on the microtubule lattice and did not move

(Figure 9.4). This could be attributed to the degraded protein or the inability to hydrolyse ATP.

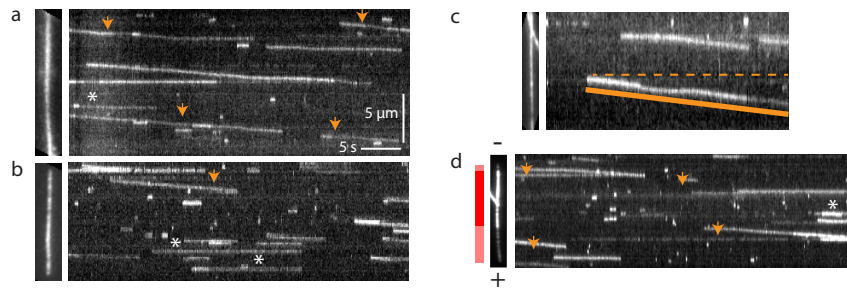


Figure 9.4.: POK2_{2083–2771}-GFP is a plus-end-directed processive motor. (a-b) Representative kymographs of POK2_{2083–2771}-GFP motility on the microtubule lattice. Respective microtubules are presented on the left. The orange arrow heads point processive trajectories. White asterisk (*) mark some immobile molecules. (c) Single molecule trajectory of POK2_{2083–2771}-GFP depicting the processive slope (orange line). Note that the intensity decreases with time. (d) Polarity-marked microtubule displaying plus-end-directed motility of POK2_{2083–2771}-GFP. The schematic on the left indicates dark red as the nucleating-end and dim red as the growing microtubule-end.

To determine the POK2_{2083–2771}-GFP directionality, polarity marked microtubules were polymerized. In an identical motility assay with polarity-marked microtubules in the presence of 1 mM ATP, it was confirmed that POK2_{2083–2771}-GFP showed motility towards the plus-end of the microtubules (Figure 9.4).

These findings are highly intriguing and perplexing. The behaviour of the POK2 C-terminus on the microtubule lattice is reminiscent of a processive kinesin but without a conserved or even a globular domain. Moreover, such a remarkable activity is present in the tail of a kinesin with an N-terminal conserved motor domain. Therefore, POK2_{2083–2771}-GFP protein sequence was closely examined and more experiments were performed.

9.4. POK2_{2083–2771}-GFP might be an unconventional microtubule motor

To examine the motor-like behaviour of POK2_{2083–2771}-GFP more closely, the first step was to rule out if these observations were an artefact. This motor-like behaviour was confirmed independently by two experimentalists. Therefore, the data acquired in the motility assays of POK2_{2083–2771}-GFP was analysed. POK2_{2083–2771}-GFP average speed was about 51 ± 1 nm/s with an average run length of 439 ± 1 nm, compared to the speed of POK2 motor at the N-terminus of 430 nm/s (Figure 9.5, Figure 8.9). This speed makes it a very slow motor but it is still enough to catch up with growing ends of the microtubules *in vitro*. The fraction of motors that did not show motility are presumably degraded or dead, were not included in the data analysis.

It is indeed fascinating that POK2_{2083–2771}-GFP exhibited features of a processive motor without the presence of any conserved cytoskeletal motor domain. Since BLASTp supported similarities with the SmC and DUF families, both of which has a P-loop or ATP hydrolysing

site, it was speculated that maybe the behaviour of POK2_{2083–2771}-GFP is nucleotide dependent. However, BLASTp did not suggest any presence of a P-loop. Although the P-loop is one of the most abundant and conserved motifs for nucleotide binding in the genomes, it is shown that there is no universal fingerprint that identifies nucleotide binding [72]. Regardless, it has been previously shown that the segments of amino acids in proteins might arrange in a way that resembles phosphate-loop function, despite their primary structures being clearly related to P-loops [72]. Such a structural similarity might confer motility to POK2_{2083–2771}-GFP.

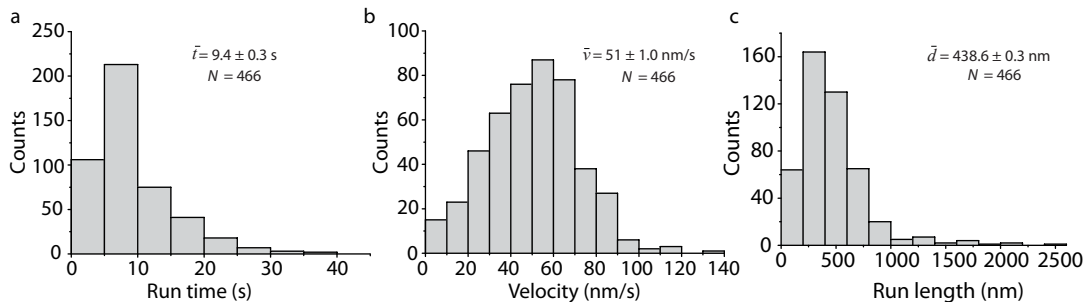


Figure 9.5.: POK2_{2083–2771}-GFP is a slow, processive motor. Distributions of total interaction times (a), speed calculated manually on the kymographs (b), run length (c) for POK2_{2083–2771}-GFP.

To investigate the local or global structure similarities of POK2_{2083–2771}-GFP, HHpred was used. HHpred is based on hidden Markov models and is used for remote protein homology detection and structural similarity for a query protein. Since the protein BLAST for POK2 did not yield significant homologies in the tail region, the sensitive HHpred server was used to detect remote homologies using a plethora of existing protein databases. The other advantage HHpred offers is that if a homologous protein is found, its structure can be used as a template to model the structure of query protein, thus providing 3D structural and functional insights. In the current case, the full-length sequence and truncated sequences of POK2 were analysed using HHpred. The results did not depend on the sequence length. Many homologues were reported for the full-length, albeit not for the entire sequence. Therefore, owing to the gaps in the sequence and especially with the presence of coiled-coils, a 3D model of the entire POK2 molecule was not generated. However, as expected, the kinesin motor domain of POK2 found, many kinesin homologues with excellent alignments were found. There were a few major hits with a probability of more than 95% also in the C-terminal region. These hits were myosin heavy chain, myosin light chain, and SmC proteins. Both myosin and SmC proteins have P-loops to bind and assist ATP hydrolysis. This intriguing structural similarity indicates that POK2_{2083–2771}-GFP indeed might possess an unconventional ATP binding motif that confers motility.

To investigate where exactly the POK2 sequence might map onto myosin or the SmC protein 3D structure, the aligned protein sequence of POK2 with these two proteins was mapped onto their 3D structures that have already been solved and are available for PyMOL. The POK2 homology with the myosin heavy chain primarily arises in the stalk region that is mostly coiled-coil structure. This homology could have been detected based on the coiled-coil occurring pattern between the two. Subsequently, when the 3D structure of full-length SmC protein was examined, striking similarities to the structure of a dimeric kinesin were found. Both SmC and kinesins have globular heads that possess ATP binding and hydrolysing site

with an extended coiled-coil tail [36, 172]. SmC proteins have globular domains on their N and C-terminus that together form an ATP hydrolysing unit. The globular domains are separated by the coiled-coil stalks that meet at the hinge region. Recent studies have demonstrated that the condensin complex constituted by the SmC proteins interacts with DNA and compacts DNA during mitosis to form chromosomes by DNA cis-looping in an ATP-dependent manner [173, 174]. Therefore, POK2 sequence was also aligned onto the SmC protein. It was found that the POK2 C-terminus mapped onto the hinge region of the SmC protein. SmC hinge region is very interesting. The hinge region is composed of positively charged amino acids that mediates interaction with other SmC hinges. There are studies that have directly shown and suggested that the hinge region interacts with the microtubule lattice [179, 180]. Hence, the analysis so far suggests that the POK2 C-terminus has a microtubule binding region that might be similar to those of the SmC proteins. However, for ATP-dependent motility, there must be an ATP binding and hydrolysis site.

```

2083   DKKDETKEIMVHVEALEKTLALKTFELEDVASHAQMLEVRLQESKEITRNLEVDTEKARKC   2143
      QEKLSAENKDIRAEAEDLLAEKCSLEEEMIQTKKVSSEMEMELFNLRNALGQLNDTVAFQTQ
2205   RKLNDAIDERDNLQDEVLNLKEEFGKMKSEAKEMEARYIEAQIAESRKYADEREEEVKLL   2266
      EGSVEELEYTINVLNKVNVVKDEAERQLRQREELEMELHTIRQQMESARNADEEMKRILD
2328   EKHMDLAQAKKHIEALERNTADQKTEITQLSEHISELNLHAEAQASEYMHKFKLEAMAEQ   2388
      VKPEIHVSQAIDSSLSKGSGKPRGSGSPFRCIGLGITQQMRSEKDEELAAARLRIELET
2449   VVSTRQKEIFLLNSKLAKVDSMTHDINRVLLGVKQNVNTCASFLDSQQVLKIAEMLQHNSS   2509
      DSRERDLEVSHLKQQLNEYNEKROQWIEEIEGKQTELVTQAIKLEEHRQYQQLLKKENELKK
2573   ENFSHKIKVMELEGEVKKLSSHQNPWRTRDQARIKEENNVLKQLDELNKLRRADVSVSR   2634
      AKEELAFYRASSVKNPHSNFDKTHQLSTLKETEDRMQLAQELLSLCTSILKAAGVTGEDFT
2698   DINPEVAEEALEQLKTKLGLLESEVHHFRLKGAKSRRSRNPERKMPSPRRSWSQSPRS   2659
      MSQVPFFSSLDR

```

Figure 9.6.: POK2_{2083–2771}-GFP sequence analysis for nucleotide binding. Manual screening of the POK2_{2083–2771} sequence proposed a P-loop site highlighted in dark red. This P-loop site/Walker A motif is unconventional and is most similar to SmC proteins that hydrolyse ATP. The predicted lysine residues are underlined. Alternative residues for the P-loop are underlined. Apart from a Walker A motif, sites similar to Walker B, ideally characteristic of hhhhDE, h being the hydrophobic residue are also highlighted in the text as cyan. Other non-conventional Walker motifs are marked in green.

Since the sequence, as well as structural similarities for the POK2 C-terminus, did not determine an ATP binding site conclusively, a manual screening of the POK2 tail that demonstrated motility was conducted. The manual screening of the ATP binding site was based upon the nucleotide protein families containing the P-loop motif. P-loop nucleoside triphosphatases (NTPases) basically hydrolyse the β - γ phosphate of bound NTP. Structure-wise, they form an $\alpha\beta$ sandwich, with mostly a parallel β sheet in the centre flanked by two α helices [73]. Sequence-wise, all of the P loop NTPases are characterized by the conserved motif A discovered by Walker and colleagues and therefore are called Walker A motif [72, 73]. Some of the family members also contain another sequence motif called Walker B, which is less conserved compared to Walker A [73]. The Walker A motif is arranged structurally between strand 1 and helix 1 of the P-loop domain, while the Walker B motif, if present, is arranged on the C-terminus of the hydrophobic strand and assists bonding between Mg^{2+} and β and γ phosphates of the NTP [72, 73]. The classical Walker A motif consensus sequence is GXXXXGK[TS], where X refers to any

residue and square brackets represent alternative residues [73]. The Walker A motif has many variations in different families, but the lysine (K) has been very conserved and important for the canonical P-loop function. The lysine could also interact and facilitate binding and hydrolysis of the β - γ phosphate bond. The Walker B motif is defined by mostly aspartate or glutamate and can occur in the preceding or succeeding sequence. The Walker A motif sequence was analysed in the following protein families. Adenylate kinases (GXPGXGKGT), ras proteins([IV][IV][IV]G[GAD]X[AG]XGK[ST]XL), the rho family (GDGAXGKT), elongation factors ([AIMS][AG]H[IV]D[AHS]GK[ST]T), ATP-synthase β -subunits (GGAGVGKTV), myosin heavy chains (GESGAGKT), kinesin heavy chains (GXXXSGKT), the dynein AAA+ family (GPXGXGKT), thymidine kinases (GXXGXGKT-T(LV)), phosphoglycerate kinases ([AV]XXGG[AS]KVXXK), and SmC families (GPXGS-GKS) [55, 70, 72, 73, 172]. Apart from these quite similar patterns of Walker A motifs, some proteins have unique consensus sequences such as DNA packaging motors in the Lambda TerL subunit (KSARVGYSK), DNA terminase Gp17 of bacteriophage T4 (LSRQLGKT) and other bacteriophage terminases, and ABC transporters in *Candida albicans* (GRPGAGCS) [181–183]. Clearly, as mentioned in the literature, there is no universal fingerprint for NTP binding and hydrolysis.

Based on this expanded literature survey, the POK2_{2083–2771}-GFP sequence was identified with probable non-canonical Walker A motif sequence (KGS~~G~~KPRGSG) (Figure 9.6). Since lysine is the most conserved residues in the Walker A motif, both of these lysine residues were identified as sites for point-mutations. The lysine in the middle of this consensus was replaced with an alanine residue by successful cloning, however, the protein is not purified yet (Figure 9.6). The first lysine was also planned for a point-mutation but has not been achieved so far. Apart from lysine, point-mutation in the arginine residue has also been planned but the construct has not been generated. Although Walker B motifs are less common, less conserved, and more diverse in the P-loop families, signatures of XXXXDE (X denotes hydrophobic residues) were identified in the POK2_{2083–2771}. Interestingly, the identified Walker A motif in the POK2 C-terminus is most similar to the SmC family Walker A motif, thus once again supporting the hits from BLAST and HHpred. This point-mutation analysis of the POK2 C-terminus are key experiments as they will prove the motility dependence of the POK2_{2083–2771}-GFP as well identify the ATPase site. It is worth noting that the analysis provided here is based on the P-loop family solely. However, there are other NTP binding protein/families without the P-loop, such as actin, tubulin, glycolytic kinases, E1/E2 type ATPases, and aminoacyl-tRNA synthetases.

Collectively, the data presented in the sections above and the bioinformatics dependent protein sequence and structural analysis suggests that POK2_{2083–2771} contains an unconventional motor. This microtubule-based motor is highly processive, slow, and plus-end-directed. This motor, I call, *Xenosin*—Greek ξένος or *Xenos* is ambiguous, meaning foreign, unusual, or strange as an adjective and guest, foreigner, stranger, mercenary, someone not from the community as a noun, or a guest-friend—contains a non-canonical ATP binding and hydrolysing site.

To rule out a possible unlabelled motor contamination, it is important to show the motility of POK2_{2083–2771}-GFP from an independent protein purification. Interestingly, the discovery of kinesin was initially also based on partial purification procedure [34]. In the current case, as mentioned earlier, originally the POK2_{2083–2771}-GFP was expressed and purified from yeast. Therefore, the POK2_{2083–2771}-GFP was cloned in an insect cell expression vector and was

expressed in SF9 cells (Figure 9.2). Unfortunately, the protein aggregated during expression. This could suggest that POK2_{2083–2771}-GFP might have been degraded, misfolded, or has a membrane binding affinity that targets it to vesicular compartments. Interestingly, the purified protein was detected on the western blot (Figure 9.2b). Even though the protein aggregates, it showed motility on the microtubule lattice. Since motility is a positive result, difficult to explain otherwise, motility validates the motor function. In Parallel, a bacterial and yeast expression system and purification is currently prepared to support the presented data.

9.5. Implications of the microtubule motor in the POK2 tail

The preceding sections have suggested the presence of a new cytoskeletal motor in the POK2 C-terminus, POK2_{2083–2771}-GFP that I call Xenosin. This observation is very exciting and raises many questions. Based on the primary and secondary protein sequence analysis of POK2_{2083–2771}, there are coiled-coil domains interspersed with unstructured regions that might form discontinuous loops or sheets. Apart from these regions, the end stretch of residues constitutes a disordered region as predicted by bioinformatics. The disordered kinesin tail region is quite a common feature as it allows specificity for binding to other cargo adaptors or post-translational modifications. How exactly POK2_{2083–2771} might fold to constitute a functional processive motor is unclear. So far it seems that the microtubule binding site with an unconventional ATP hydrolysing unit, might be enough to translocate on the microtubule lattice. These domains are located presumably in unstructured regions. If these regions are indeed unstructured, this would be a revolutionary finding as most of our understanding of proteins, in particular, motor proteins, is based on solid structural folds. Recently, researchers have tried to highlight the importance of unstructured regions in proteins. For example, tau, a key microtubule-associated protein that regulates microtubule dynamics in axons is a disordered protein and can diffuse along the microtubule lattice. XMAP215, a microtubule polymerase from *Xenopus* cooperates between its structured domains and disordered flexible regions to polymerise microtubules. XMAP215 displays processive motion on the microtubule lattice driven by microtubule dynamics [184, 185]. If the basic engine module upon folding remains remotely similar to what has been observed for myosin and kinesin, remains to be seen. Therefore, how this new motor Xenosin folds into 3D is thrilling and important for understanding of how the motor works. Further questions pertain to Xenosin's force generation capabilities, its mechanochemically driven walking gait, its stepping size, and its interaction with dynamic microtubules.

If POK2_{2083–2771}-GFP forms oligomeric structures such as dimers, tetramers, which are shown to be a requirement for processive kinesins, was not investigated in detail. The intensity profiles during the kymograph analysis of POK2_{2083–2771}-GFP, suggests that Xenosin is a dimer.

The presence of this microtubule-based motor in POK2_{2083–2771}-GFP directly confirms the *in vivo* suggestion of direct microtubule binding. It is interesting that POK2_{2083–2771}-GFP localized on cortical microtubules but not phragmoplast microtubules [92]. Thus Xenosin's motility might be dependent on the post-translational modified (PTM) state of the mi-

microtubules [22]. As discussed in the introduction, PTMs confer functional and structural differences to microtubules. In plants, the role of these PTM microtubules has also not been studied in detail, partly because of its challenging and non-conclusive results. Understanding this effect is difficult *in vitro*, however, a reconstituted assay with deacetylated, tyrosinated, detyrosinated etc. microtubules in future, might shed light on interaction between Xenosin and the microtubule lattice.

The *in vivo* localisation of POK2_{2083–2771}-GFP suggested its microtubule dependence by overlapping localisation with the preprophase band. Moreover, the continued presence of POK2_{2083–2771}-GFP at the division site after PPB disassembly hints that POK2_{2083–2771}-GFP could also interact with the plasma membrane directly. If affirmative, how does the POK2_{2083–2771}-GFP integrate the motor and the membrane interaction site structurally? Interestingly, POK2_{2083–2771}-GFP has been reported to directly interact with MAP65-3 similar to its N-terminal extension [92]. Although, this interaction using localisation microscopy looks weak, MAP65-3 might mediate plasma membrane POK2 tethering. MAP65s have been reported as interactors or mediators for membrane interaction, especially as MAP65-3 is localized at the division site [186, 187].

Xenosin, the new microtubule-based motor is located in the C-terminus of POK2 that already contains a conventional kinesin motor at its N-terminus. How does the presence of a new motor affect the structure and function of POK2? How does a POK2 molecule at the division site guides the phragmoplast? These questions are addressed in the last sections.

9.6. POK2 anchoring at the membrane

The continued presence of POK2_{2083–2771}-GFP at the division site despite the PPB compelled to investigate if POK2_{2083–2771}-GFP was capable of directly interacting with the plasma membrane. Therefore, an *in vitro* direct lipid interaction approach was taken. Phosphoinositides (PIP) strips were used for protein-lipid overlay assay. PIP strips are commercially available nitrocellulose sheets that are marked with pico-molar amounts of various lipids. Purified POK2_{2083–2771}-GFP was incubated with the PIP strip with an optimized protocol. Using an immunostaining method similar to the western blot, the protein-lipid interaction was read out under chemiluminescence. POK2_{2083–2771}-GFP interacted mainly with PIPs, however, with varying degrees of interaction strengths (Figure 9.7). The order of interaction from strongest to weakest was PI(4)P, PI(5)P, and PI(3)P (Figure 9.7). Dual phosphate inositides were also positive in the overlay assay, suggesting either a weak interaction with these or unspecific binding as POK2_{2083–2771}-GFP was interacting with single phosphate inositides. Apart from the strongest contender PI(4)P, POK2_{2083–2771}-GFP also showed interactions with phosphatidic acid (PA) and phosphatidylethanolamine (PE) (Figure 9.7).

Confirmatory tests for this protein-lipid interaction are planned using plant-specific lipids. An assay based on giant unilamellar vesicle (GUVs) with the protein was optimized. Preliminary experiments with GUVs, using animal lipids consisted of 5% PI(3)P, 1% PI(3,5)P₂, 89% EggPC, and 5% rhodamine labelled PE showed co-localisation with POK2_{2083–2771}-GFP under confocal microscopy. This suggests POK2_{2083–2771}-GFP directly interacts with PI(3)P and PI(3,5)P (Figure 9.7). The interaction was not observed immediately after protein addition. The co-localisation was observed after 30 minutes of incubation. This suggests a diffusive interaction of POK2_{2083–2771}-GFP with the lipids. GUVs prepared with

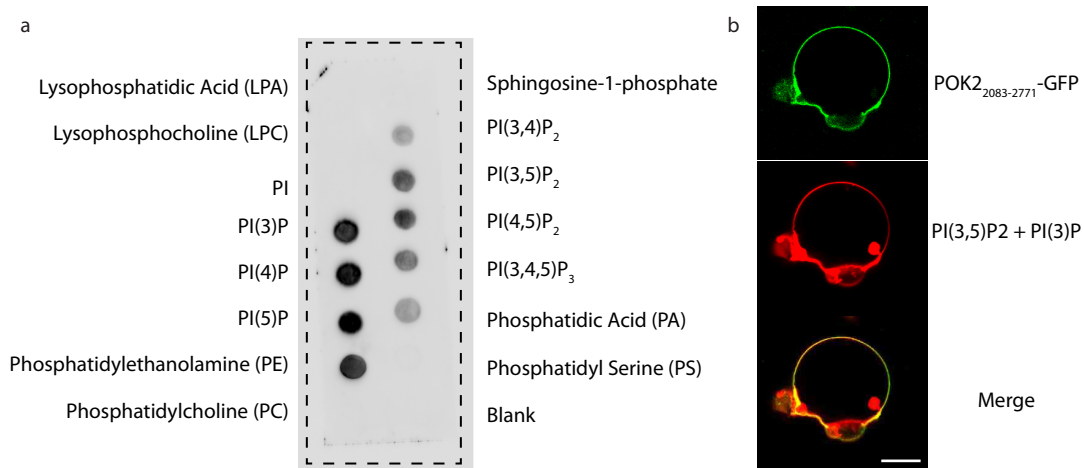


Figure 9.7.: POK2₂₀₈₃₋₂₇₇₁-GFP has a membrane binding site. (a) PIP strip showing the interaction of POK2₂₀₈₃₋₂₇₇₁-GFP with specific lipids as detected by anti-GFP antibody. The strongest interaction is with PI(4)P and other phosphoinositides. (b) Rhodamine labelled PI(3)P and PI(3,5)P₂ enriched GUVs show interaction with POK2₂₀₈₃₋₂₇₇₁-GFP. Scale bar 20 μm.

plant lipids and sterol are planned but have not been executed. Nevertheless, it is clear that POK2₂₀₈₃₋₂₇₇₁-GFP can directly interact with the plasma membrane at the division site. If the division site has a distinct membrane composition compared to the rest of the plasma membrane is not known. However, such a distinct composition is a tempting hypothesis as the membrane composition or lipid modifications at the division site could enable localisation of specific proteins to a localized region. This hypothesis is challenging to test, but the lipid interaction of division site markers such as POK2 might provide insights into this localized membrane environment. Based on a recent study, whether the Rho-type GTPases of plants (ROPs) localized at or around the division site plays a role in defining the membrane composition of the division site is fascinating [188].

The recent development of plant lipid sensors have enriched our knowledge of membrane composition (Figure 9.8). The plant plasma membrane is reported to be enriched with a cocktail of anionic lipids (PIPs, Phosphatidic acid (PA), Phosphatidylserine (PS)) and a gradient of this electrostatics exists from the plasma membrane, which defines the localisation of proteins [188, 189]. Among the PIPs, PI(4,5)P and PI(4)P are quite important in maintaining the surface charge of the plasma membrane [189–191]. PI(4)P accumulates in an abundant manner and is also hugely present in the developing cell plate. PI(3)P is suggested to be localized at endomembranes [192]. The localisation of PI(3,5)P is not known yet, however, mutants display vacuolar defects in pollen and reduced stomatal closure [192]. PI(3,4,5)P has not been shown in plants to date [192]. The observation made in the lipid-interaction assays in this thesis suggests that POK2₂₀₈₃₋₂₇₇₁-GFP strongly interacts with PI(4)P (Figure 9.7). This is consistent with the *in vivo* localisation data that shows POK2 is present at the division site (at the plasma membrane) as well as at the phragmoplast midzone (developing cell plate) [190, 191]. Interaction with PI(3)P and PI(5)P also suggests that the presence of these phosphoinositides at the division site or/and developing cell plate is possible.

Interestingly, POK2₂₀₈₃₋₂₇₇₁-GFP showed a weak interaction with PE in the PIP-strip

assay. PE has been reported to be present in only single-leaflet of the membranes and is abundant in extraplastidial membranes [193, 194] (Figure 9.8). The interaction of the POK2 C-terminus with PE is fascinating because PE is specifically localized at the cleavage furrow and is pumped actively from the inner leaflet to the outer leaflet that enables proper functioning of the contractile ring during animal cytokinesis [194]. If PE plays an analogous role at the plant division site remains to be explored.

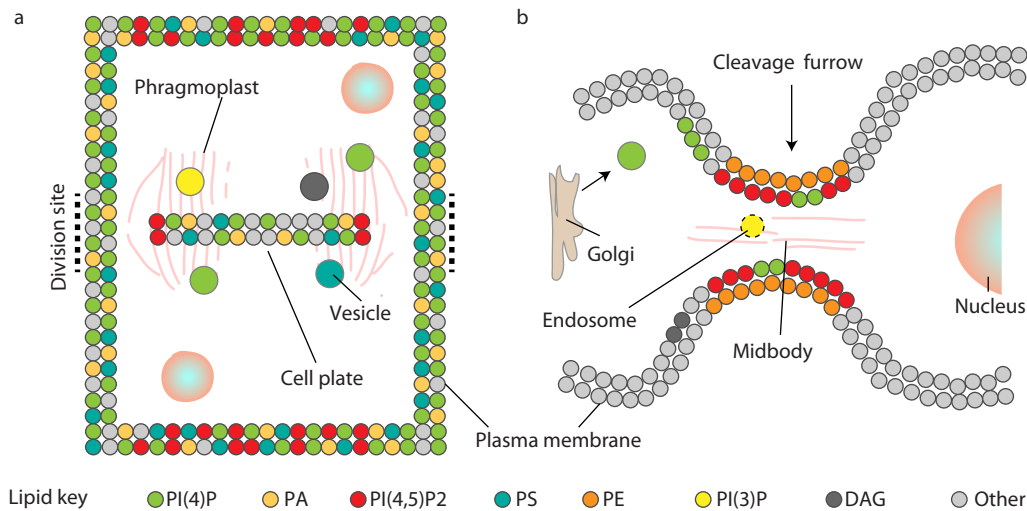


Figure 9.8.: Comparative analysis of membrane composition in plants and animal cytokinesis. (a) Schematic representation of the lipids enriched in the plant cell membrane and developing cell plate. The division site is represented as black dashed line outside the cell. The phragmoplast is shown near the cell plate as dim red lines. (b) Membrane composition at the cytokinetic furrow during animal cytokinesis. The midbody is represented as dim red lines. The figure was created from data in [189–192, 195].

Given that the data suggests a direct interaction of POK2_{2083–2771}-GFP with the lipids, it raises a few important questions. Is this interaction weak or strong? Conclusive quantitative measurements might determine the interaction strength. Presumably, this interaction might be reinforced by other residents of the division site. MAP65-3 and others might be the favourite candidates as also supported by the *in vivo* data [92, 186]. Another important question is where the exact lipid-interacting or binding motif in the POK2 C-terminus is. The localisation is interesting because POK2_{2083–2771}-GFP also contains a microtubule binding site and exhibits motor characteristics, and has no predicted membrane motif in the sequence. Since there is no clear membrane binding motif, the best way to approach this problem is to create further truncations of POK2_{2083–2771}-GFP, at least two, to narrow down the membrane binding region. It is hypothesized that the POK2_{2083–2771}-GFP might interact with lipids in a C-terminal anchor manner as demonstrated for Remorin [196]. Remorin is a well-characterized membrane nanodomain marker that has been recently shown to anchor and fold in the plasma membrane after its interaction with lipids [196]. The C-terminal anchor of remorin is also disordered and the membrane interaction is mediated by PI(4)P and sterols [196]. This hypothesis is favoured because POK2_{2083–2771}-GFP expression in protoplasts results in puncta like structures resembling nanodomains. This nanodomain hypothesis, if affirmative, would favour localized domain organisation at the division site, where the future

cell wall is perceived. Moreover, the disordered C-terminus in the membrane might act as a fluid anchor that becomes essential for narrowing of the division site during late stages of cytokinesis.

9.7. *POK2*_{2083–2771}-GFP does not bind actin filaments

The division site in plant cytokinesis is the cortical and membrane region that underlies and is defined by the preprophase band. Usually, the cellular cortex in close proximity of the plasma membrane has robust actin dynamics. Even though the division site in *Arabidopsis* is labelled as an actin-depleted zone, recent studies have postulated a re-evaluation of actin's role during late cytokinesis [94, 95]. Bioinformatics analysis identified two actin-binding motifs in the POK2 tail domain and the direct POK2_{2083–2771}-GFP lipid interaction suggest that the POK2 C-terminus could possibly modulate actin-dynamics (Figure 9.1). Moreover, the sequence-structural similarity yielded a myosin heavy chain similarity. Furthermore, the new microtubule-associated motor Xenosin might act as a dual-substrate motor too. Therefore, it was instructive to see if POK2_{2083–2771}-GFP might bind to actin as well.

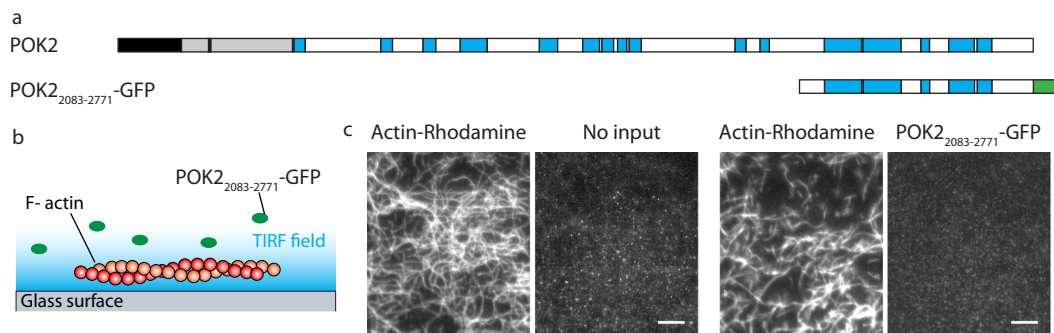


Figure 9.9.: *POK2*_{2083–2771}-GFP does not have an actin-binding site. (a) Schematic representation of the POK2_{2083–2771}-GFP construct relative to the full-length POK2. (b) Schematic of the *in vitro* experimental set up. (c) TIRF microscopy images depicting no co-localisation of POK2_{2083–2771}-GFP with phalloidin-stabilized actin-filaments in presence of 1 mM ATP.

The two predicted actin-binding sites were and located at residues 937–953 and 2674–2689, respectively. Since there was no availability of a full-length POK2 construct, POK2_{2083–2771}-GFP was used to check one of the proposed actin binding sites. Actin was polymerized and stabilized by rhodamine-phalloidin (Figure 9.9). Subsequently, actin was immobilised on the coverglass surface and purified POK2_{2083–2771}-GFP was flushed in the presence of 1 mM ATP. It was clear that POK2_{2083–2771}-GFP did not bind to actin in the presence or absence of ATP (Figure 9.9c). However, this finding does not rule out that full-length POK2 binds the actin filaments as the other predicted actin site lies in the middle of the POK2 tail region, for which no construct was created. It might also be possible that a POK2 mediated actin interaction is calcium based, which was not checked. Irrespective, an interaction of POK2_{2083–2771}-GFP seems unlikely as this tail domain already have two important functions.

9.8. Proposed role of POK2 during plant cell division

Based on the data presented in the current as well as previous chapter and the reported literature, this section postulates possible roles of POK2 during plant cell division. POK2 localizes at the division site via any of its two microtubule-based motor domains, i.e. highly conserved N-terminal kinesin motor domain or the unique and non-conventional xenosin motor at the C-terminus. The localisation data using POK2_{2083–2771}-GFP supports that the C-terminal motor might be enough for localisation [92]. This localisation is presumably preprophase band/microtubule-dependent as microtubule depolymerization leads to loss of POK2_{2083–2771}-GFP. Once POK2 is localized at the division site, the C-terminal disordered sequence might enable tethering to the membrane. This anchoring could primarily be dependent on PI(4)P, however, the division site might also contain PI(3)P, PI(5)P, PI(3,5)P, PE, PS, and PA, where the latter two showed weak or negligible interaction with the POK2 C-terminus [189, 190, 192] (Figure 9.10). This anchoring might be reinforced by other residents of the division site such as MAP65s, Tangled, etc. (Figure 9.10). MAP65-3 has been shown to interact with POK2_{2083–2771}-GFP and it has been suggested that POK2_{2083–2771}-GFP might also interact with other MAP65s localized at the division site, however, the exact interacting region in this 700 amino acid protein has not been identified yet [92]. Once the PPB disassembles, POK2 stays put at the division site till the end of cytokinesis. Subsequently, during late cytokinesis, when the peripheral microtubules start emanating from the expanding phragmoplast, division site localized POK2 captures the peripheral microtubules. Harnessing its high affinity N-terminal extension and motor domain, POK2 in then walks towards the plus-end of the peripheral microtubules. After a connection is established, the POK2 C-terminal xenosin motor might also grab the microtubules and start walking towards their plus-ends. Together, both motor domains effectively push against the expanding phragmoplast, thereby orienting the growing cell plate. Given that POK2 is tethered at the membrane, pushing of the phragmoplast might be enhanced by an entropic collapse of POK2's lengthy coiled-coil similar to Rab5 effector protein EEA1, thus releasing mechanical energy [197]. Such entropic collapse mechanism usually allows confirmation change in the coiled-coils. This is well known for coiled-coils and membrane-associated tethers [197–199].

As the two different motors are spatially separated on the POK2 molecule, what advantage does this incur to the POK2 molecule? One major consequence of pushing forces is the narrowing of the division site as discussed in section 8.10. The narrowing of the division site to a cell plate fusion site during late stages of cytokinesis is possibly a fine tuning process, whereby cell plate is accurately inserted. It is unlikely that both kinesin and xenosin motor would bind to the same microtubule given that they are separated by about 200-250 nm (inferred based on coiled-coils of CENP-E and EEA1 from [18, 197]) in an extended confirmation. In such a case, kinesin motor would first push against the peripheral microtubules and when a growing microtubule reaches xenosin, it would also push against it. Together, they might cross-link microtubules, thus preventing over-focussing of the division site (Figure 9.10, Figure 8.19). Thus, bringing a balance to accurately define the cell plate fusion site.

Given the POK2 localisation at the phragmoplast midzone, what is the role of xenosin? At the midzone, POK2 interacts with MAP65-3 [92], which cross-links anti-parallel microtubules. POK2 with its two motors should slide these microtubules apart and narrowing the overlap in analogy to Eg-5 [13]. Furthermore, away from the midzone, it may bundle parallel microtubules. This situation would then be quite similar to human kinesin-12 hKif15 at the

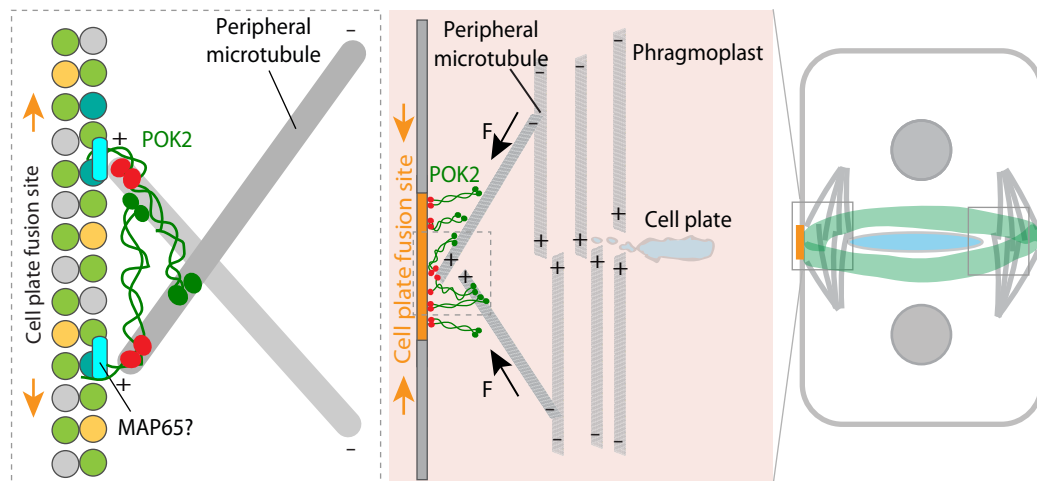


Figure 9.10.: Proposed role of full-length POK2 at the division site. (*Right*) Schematic of a plant cell depicting localisation of POK2 at the division site and denoting cell plate fusion site. (*Centre*) Full-length POK2 anchored at the cell plate fusion site is a dimer with two motors at front (green) and two motors at rear end (red). The POK2 molecules capture the peripheral microtubules from the phragmoplast leading edge and all the four motors walk towards the plus-ends, thus pushing against it. The black arrows show the opposite force acting from the phragmoplast to narrow the division site to cell plate fusion site (Figure 8.19). The kinesin motor domains are responsible for efficient catching and pushing against the phragmoplast. (*Left*) A magnified picture of possible POK2-peripheral microtubule action at the cell plate division site. POK2s are possibly anchored in the membrane with reinforced interaction with MAPs. Due to the separation between the kinesin domain and xenosin (about 230 nm), POK2 can cross-link peripheral microtubules and thus, preventing over-focussing/over-narrowing of the division site. The orange arrows show the counter force to narrowing. Note that the membrane composition here is represented from Fig. 8.

spindle, where it forms parallel microtubule bundles using its tetrameric ability [12] (Figure 9.11). Such parallel bundling might provide stability to the phragmoplast structure. On the other hand, the sliding apart of anti-parallel microtubules at the midzone in conjunction with cross-linking MAP65-3 might govern the extent of the midzone overlap. Phragmoplast midzone is also the centre for Golgi-derived vesicles that are enriched in PI(4)P. Since POK2 C-terminus showed the highest affinity for PI(4)P, it might interact with cytokinetic vesicles at the midzone. Together, POK2 at the midzone might provide stability to the phragmoplast and govern the extent of cell plate width and morphology.

As mentioned in preceding paragraphs, the two motors in the POK2 molecule are spatially separated. How important is this spatial distance with respect to functionality and regulation? The bioinformatic analysis also predicted many phosphorylation sites in the POK2 protein. Therefore, phospho-mimic protein constructs would be handy in delineating the regulatory and functional roles in POK2 motors. Moreover, the localisation data shows that the POK2 C-terminus motor not decorate all microtubules as strongly compared to the kinesin motor domain. This finding could be due to specific targeting of these motors on different post-translationally modified (PTM) microtubules. Thus, to what extent the cytokinetic driven microtubule apparatus has a varying composition and what effects PTMs might have on the orientation of the cell plate will have to be addressed in the future.

It has been well established that POK2 and POK1 function redundantly. This thesis also investigated the kinesin motor domain of POK1. POK1 was found to be a plus-end-directed processive motor. But what is the function of the POK1 C-terminus at the division site? Therefore, the POK1 sequence was analysed and did not suggest the presence of a P-loop containing protein in the C-terminus. There was a SmC similarity, however, the similarity was in the coiled-coil region. It has been shown that POK1 C-terminus interacts with Tangled and Ran GAP1 [91]. Tangled is a very interesting protein as it is a MAP and is a miniature version of APC (adenomatous polyposis coli) in animals, that steers microtubules by interacting with EB1 and kinesin molecules [7]. Additionally, it has been shown that tangled interacts with microtubules in maize [200]. Therefore, it is hypothesized that POK1 in complex with tangled has a second microtubule site and might be able to cross-link the peripheral microtubules. Although tangled lacks the Eb1 binding domain, it will be interesting to test to what extent tangled alters the activity of POK1 by binding to its C-terminus. Moreover, POK2 was also discovered in a yeast two-hybrid screen with tangled, it is also worth checking the direct interaction of POK2 [87]. Therefore, a full-length clone of *Arabidopsis* tangled was created but the protein has not been purified yet. Thus, how residents of the division site such as tangled contribute to cell plate orientation is unclear at the moment. The redundant mechanical function of POK2 and POK1 potentially in complex with tangled still needs to be demonstrated.

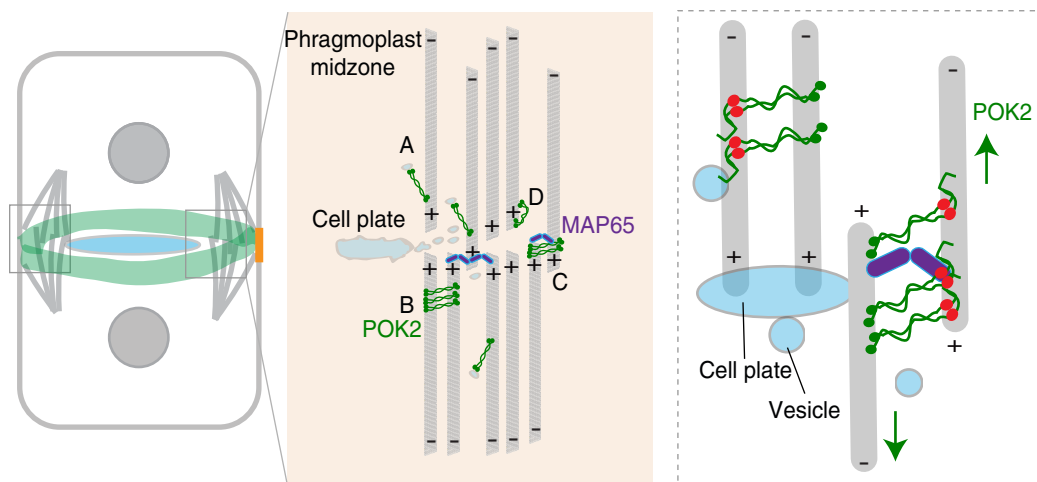


Figure 9.11.: Proposed role of full-length POK2 at the phragmoplast midzone. (Left) Schematic of a plant cell depicting localisation of POK2 at the division site and the late phragmoplast. (Centre) Possible roles of full-length POK2 at the phragmoplast midzone. (Right) Favourite hypothesis of POK2 mediated anti-parallel microtubule cross-linking and sliding at the phragmoplast midzone. MAP65 at the midzone stabilises the anti-parallel overlap while POK2 narrows it by sliding them apart in analogy to mitotic spindle midzone. Green arrows mark the direction of sliding. Based on the POK2 C-terminus and lipid interaction, it is believed that POK2 interact with cytokinetic vesicles or the fenestrated sheet in the division plane. Given the contour length of full-length POK2 and the presence of two novel plus-end-directed motors in the C-terminus in POK2 dimer, this might enable parallel bundling of the microtubules in the phragmoplast away from the midzone.

Apart from POKs, kinesin-14 members also localize at the division site, and possibly interact with the peripheral microtubules of the expanding phragmoplast [88]. In such a

case, a tug-of-war mediated phragmoplast guidance would be expected. To what extent kinesin-14 members are involved in phragmoplast guidance is not known. As mentioned in the preceding section, KCBP, the kinesin-14 member that localizes at the division site has been reported to possess a secondary microtubule binding site at its C-terminus [178]. With such a binding site, KCBP would also cross-link microtubules and increase the overlap of cross-linked anti-parallel microtubules. Thus, KCBP and POK2 might have an antagonistic function with MAP65s stabilizing the overlap. Such a scenario is analogous to the mitotic spindle [201, 202]. Interestingly, it seems that kinesins localized at the division site have been selected in evolution to contain a secondary microtubule binding site. Has the evolution of preprophase band or phragmoplast mediated cytokinesis in higher plants co-evolved with such a functionality too? This calls for an ancestral look at the kinesins that play a crucial role in the orientation of cell plates in higher plants during cytokinesis.

9.9. Evolutionary aspects of POK2

The presence of the unusual xenosin motor in a kinesin molecule along with the existing and conserved motor domain is a remarkable observation. This finding in the POK2 molecule, as presented in this thesis, raises questions about its evolution. Moreover, POK2 is one of the six members of the kinesin-12 family in *Arabidopsis*. This family is expanded as compared to animals and all of its members have a function during cytokinesis. Thus, it is compelling to investigate the evolutionary relationships for these kinesin-12 members that play an essential role during cytokinesis. Therefore, an evolutionary relationship amongst these kinesin-12 members were examined with a special focus on POK2.

Firstly, the phylogenetic relationship among kinesin-12 members was examined using PhyML (Figure 9.12) [35]. PhyML is an online platform that analyses the phylogeny between DNA and protein sequences based on the maximum-likelihood principle. All kinesin-12 member sequences were retrieved from Uniprot [169] and aligned using Clustal Omega [35]. The phylogenetic tree includes human kinesin-12, hKIF15. The PhyML tree suggests that Kinesin-12A and 12B are closely related to each other and share a common ancestor. Also, POK1, POK2, and Kinesin-E are closely related to each other and share a common ancestor. Kinesin-12F has diverted from this ancestor. These findings are supported by the functional evidence about the kinesin-12 family. POK1 and POK2 function redundantly at the division site during cytokinesis to possibly guide the phragmoplast [91, 92]. Kinesin-12A and 12B deliver cytokinetic vesicles to the phragmoplast midzone, and thus, are involved in cell plate formation [108]. The function of the two other kinesin-12 members is still unclear.

It is interesting that *Chlamydomonas* has only one kinesin-12 member, compared to six members in rice or *Arabidopsis*. Therefore, I investigated at what point this family started to expand in evolution. The sequence ancestral relationship was analysed using ANCESCON [35]. This software allows the reconstruction of ancestral protein sequences based on the distance-based phylogenies. It also considers observed variations of evolutionary rates at specific family-specific residue positions. Surprisingly, the phylogenetic tree looked different compared to the one based on PhyML. However, the relationships amongst the members remained the same. Kinesin-12A and 12B remained closest to each other. POK1, POK2, and kinesin-12E also showed a close relationship. One important observation in this tree is that POK2 might be the founding kinesin-12 member in *Arabidopsis*. This observation

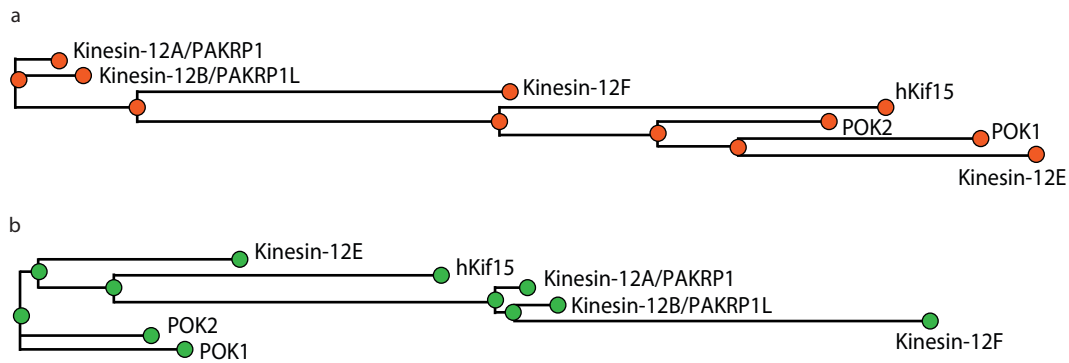


Figure 9.12.: Phylogenetic tree of the kinesin-12 family in Arabidopsis. (a) Phylogenetic tree representing relationships among the kinesin-12 family with human kinesin-12 as an outroot based on the amino acid sequence alignment. (b) Phylogenetic representation of the kinesin-12 family based on the ancestral relationships. This tree is based upon distance-based phylogeny estimation and involves evolutionary variations at the residue level in estimating the ancestral protein sequence construction.

is interesting because of POK2's xenosin motor domain. Therefore, I checked, if this new motor has similarities to motors in the plant kingdom and how it evolved.

To investigate the POK2 origin, a sequence-similarity-based approach was taken. Using kinesin-12 members individually as a query in BLASTp [170], I searched for proteins with any sequence similarities against each of the phyla presented in the phylogenetic tree (Figure 9.13). I found that except for POK2, no other kinesin-12 member showed sequence similarity in its C-terminus in lower plants including *Chlorophyta* (Figure 9.13). This conservation again suggests that indeed POK2 might be the founding kinesin-12, while other members expanded during evolution of higher plants. What function this ancestral protein homologue has in lower plants is intriguing and not known.

Tracing the POK2 similarity coverage from *Chlorophyta* to higher plants, it was observed that the similarity coverage gradually increased respectively. The blue regions in Figure 9.13 indicate the region of similarity when mapped onto full-length POK2. There are few phyla where no results were observed at all. This lack could be due to limited data in these databases. The sequence similarity match towards in the POK2 N-terminus most likely a conserved kinesin domain. The similarity in the C-terminus is more exciting and suggests that the xenosin motor domain and/or the non-canonical membrane binding motif in the POK2. It is worth to stress that these similarities exist within the same protein. Therefore, it is exciting to speculate if these proteins in lower plants also have the ability to bind membranes and/or whether the C-terminal domain has xenosin-like motor functions. Due to their unconventional sequence and structure these domains may have not been discovered. Whether these novel membrane and motor like features are exclusively present in plants or also in animals and even primitive prokaryotes still needs to be investigated. The BLASTp search for POK2 detects a family with a P-loop motif in the C-terminus of POK2 that is conserved in prokaryotes and eukaryotes suggesting that xenosin may not be limited to the plant kingdom.

Assuming, an ancestral version of POK2 existed in lower plants such as *Chlorophytes* and

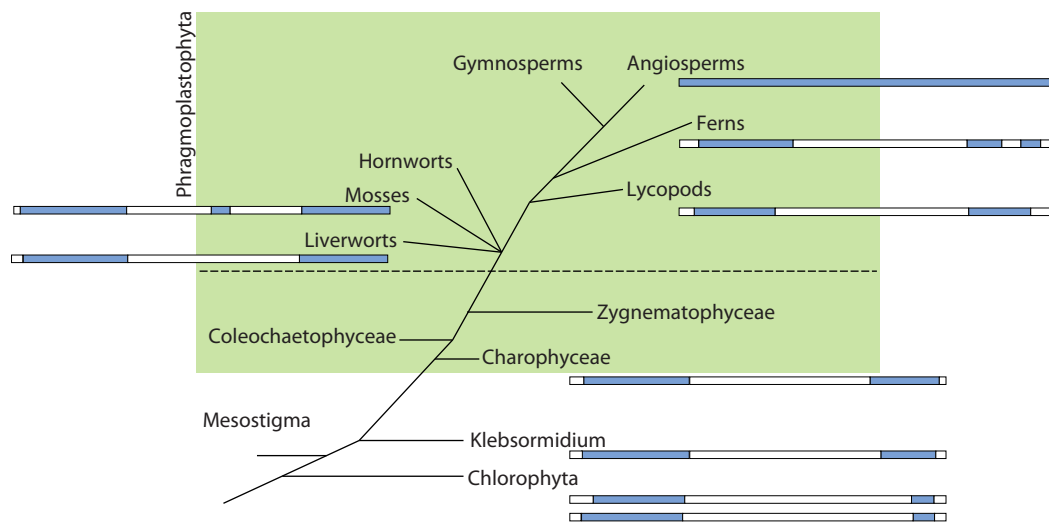


Figure 9.13.: Evolutionary origins of POK2. A phylogenetic tree representing the evolution of higher plants as previously shown in the Figure 2.4. POK2 full-length represented as a whole blue bar in angiosperms is traced back to lower plants and Streptophytes. The blue regions display the sequence similarity with POK2.

Klebsormidium, expressing or purifying those proteins and investigating the functionality in similar *in vitro* reconstituted assays will answer whether or not membrane binding and xenosin motor function was conserved. In particular, questions regarding how an ancestor of such a chimeric multifunctional motor might have worked can be approached by retrieving the ancestral sequence predicted from ANCESCON and investigating it in *in silico*.

One other striking thing, this bioinformatic analysis about POK2 has suggested is the presence of a POK2-like ancestral protein in plants where cleavage and other modes of cytokinesis were prevalent along with the presence of centrosomes. Did these proteins assist in a division plane dependent mechanism under cleavage and other modes of cytokinesis too?

In summary, this chapter has provided new insights into the tail domain of POK2. The presence of a second, novel xenosin motor domain in a protein that already contains a conserved kinesin motor domain is extraordinary. The presence of the C-terminus sequence in lower plants where cytokinesis was executed by cleavage without the presence of a pre-prophase band and the phragmoplast is intriguing. If proteins like POK2 and others have imbibed a centrosomic character in higher plants to steer microtubules for alignment purposes is an exciting possibility and a futuristic venture. The functionality of microtubule bundling and sliding them apart is important in mitotic spindle overlap, appears to be relevant in the phragmoplast midzone, and may be a key to the division site. In addition, the identification and presence of the new motor xenosin might provide new avenues for finding other unidentified molecular machines.

Part IV.

Closure

10. Outlook

In this thesis, I have characterized the function and mechanics of the POK1 and POK2 motor domains. Furthermore, I have discovered a novel microtubule-based motor, termed, xenosin, and unconventional membrane binding motif in the C-terminal tail domain of POK2. Together, the thesis proposes a pushing model for proper guidance of the phragmoplast towards the cell plate fusion site by POK2 and POK1 at the division site. Based on the data gathered, the thesis also postulates possible roles of POK2 at the phragmoplast midzone. This section suggests future experiments that would expand our understanding of the division site and POKs involvement in phragmoplast expansion and guidance during cytokinesis in higher plants.

The kinesin motor domains of POK1 and POK2: Although the first obvious experiment would be to purify full-length POK1 and POK2, several attempts were unsuccessful so far. As mentioned in the results and discussion chapter, the enormous size and possibly the complexity of the sequence poses a challenge in getting the full-length proteins. Therefore, *in vitro/cell free* cloning and synthesis of these kinesins might be a plausible solution. Using only the motor domains of POK1 and POK2 with their N-terminal extension remain to be addressed. The experiments carried out in this thesis were primarily conducted with stabilized microtubules. If POKs are capable of altering microtubule dynamics is unclear. Although the conditions for dynamic microtubule assays were optimized during this thesis, comprehensive experiments studying the effects of POK2 and POK1 on dynamic microtubules are still lacking. Since POKs localize at the division site and capture plus-ends of peripheral microtubules, POKs might be capable of stabilizing growing microtubule ends, for example, by reducing the catastrophe frequency. Stabilizing effects might also be important at the phragmoplast midzone as proposed already in Figure 8.20. Another open question is the stepping behaviour of POK2 and POK1, especially because these kinesins have a short neck linker (5-6 amino acids). As mentioned previously, the stepping behaviour of human kinesin-12, hKif15 has been proposed to be non-canonical [162]. Moreover, kinesin-10 family member that has been classified as orphan kinesin PAKRP2 and localizes to the phragmoplast has been recently suggested to have a non-canonical stepping mechanism with prolonged intermediate states [47]. Therefore, it would be interesting to look in detail at the stepping mechanism of POKs. Additionally, the ATP hydrolysis should be measured to test the mechano-chemical coupling. Due to the switching mechanism, ATP hydrolysis might not be tightly coupled to stepping.

Preliminary force measurements under multi-motor conditions for the POK1 motor domain suggest that it might be able to generate higher forces as compared to single POK2 motors with 0.3 pN. Therefore, force measurements for single POK1 are necessary to confirm the hypothesis.

Both POK2 and POK1 are capable of switching between processive and diffusive modes, however, to different extents. How a molecular motor is capable of switching motility modes is still an elusive question. Therefore, a structural understanding of these motors would be

helpful. A known POK structure could then be compared to kinesin-1. This way, certain loops and coils could be identified and altered to see how and which residues might create a mechanical level to cause the motility switch. The structure might also provide insight into how the N-terminal extension of the POKs is organized in 3D space. If these switches also depend on the post-translational state of the microtubules such as acetylation, tyrosination, glycylation etc., is an intriguing question. While it is a challenging question, with the advent of recombinant tubulin, it might be feasible [203, 204]. Removal of the e-hooks that harbour these PTMs using the enzyme subtilisin might be another way of understanding the motor-microtubule interaction behaviour. This could also provide insights into the PTMs state of peripheral microtubules from the phragmoplast given that POKs localize at the division site and capture them.

C-terminus tail of POK2 and POK1: The C-terminus of POK2 has revealed two new features: membrane binding and a motor domain. The processive microtubule-associated plus-end-directed motility, requires the presence of a nucleotide specific molecular motor. This is exciting given the absence of conserved motor domain in the sequence. Many open questions remain such as the ATP dependence of the speed and the ATP hydrolysis rates. Once these independent experiments validate the presence of xenosin in the POK_{2083–2771}-GFP, further experiments aiming at determining the exact domain size and in analogy to kinesin-1 would be essential. Cryo-EM might enable to determine the structure of xenosin. Moreover, proper identification of the microtubule binding site and the ATP binding/hydrolysing site would be necessary. This thesis has identified P-loop consensus sequences. Mutation of the two suggested lysine in the proposed consensus could confirm the P-loop. To identify the microtubule binding site, the POK_{2083–2771}-GFP sequence can be further truncated and subsequently, co-localisation and motility assays would then help in identifying the microtubule binding region.

A full-length POK2 would be indispensable to understand how such a hybrid motor functions. Which motor is stronger? Does the faster one accelerate the slow one? Is there communication between them, e.g. via tension? Does the POK2 motor cross-link microtubules?

Apart from the novel motor, this thesis also reports that POK_{2083–2771}-GFP interacts with the membrane. The terminal amino acids might provide an anchorage into the membrane enriched in PIPs. To identify the membrane binding site, truncated versions of POK_{2083–2771}-GFP as suggested above for microtubule binding will be useful. These truncated constructs, together with the PIP strips and GUVs could provide the membrane binding stretch and specificity of lipids.

The C-terminus of POK1 was not tested for membrane binding and motility assays. Basic bioinformatic analysis of POK1 did not indicate SMC and DUF domains in its C-terminus. Interestingly, the C-terminus of POK1 has been shown to interact with the MAP tangled [91]. How does the interaction of tangled affect the motility of POK1? To this end, tangled was cloned and after purification, its interaction with the POK1 can be tested. With two microtubule binding sites, does the POK1-tangled complex cross-links microtubules? Is the functionality of the complex comparable to POK2 to explain functional redundancy at the division site? It will be worth while to check if tangled also interacts with the POK2 C-terminus as POK2 was originally discovered in yeast-2-hybrid assays with tangled as bait.

Evolutionary understanding of POKs: POKs belong to the most enormous kinesins known across taxa. What makes them special? Why is the kinesin-12 family expanded

in plants? POKs might be the oldest kinesin-12 members among the family, with POK2 being the first. The phylogenetic analysis suggests the presence of POK2 homologues in Streptophyta. Therefore, it would be interesting to express those kinesins in *Arabidopsis* and check their localisation and function.

In this thesis, ANCESCON was used to infer these ancestral relationships among the kinesin-12 family in *Arabidopsis*. This tool also reconstructs the ancestral protein sequence for the family. It would be highly interesting to use this predicted protein sequence and purify this protein. Subsequently, in an *in vitro* reconstituted assay, the functionality of this ancestral protein could be tested. This information would support the evolution of kinesin-12 family themselves and would broaden our understanding of basic cell division.

***In planta* validation of POKs:** The experiments suggested in this chapter so far, primarily propose an investigation of POKs either as full-length proteins or truncated versions using single-molecule *in vitro* reconstituted assays. However, to validate these findings in plants, it is important to demonstrate the molecular mechanisms *in vivo*. The localisation of full-length POKs have been already shown in *Arabidopsis* [91, 92]. The findings in this thesis provide a base for *in planta* experiments that might bolster previous findings and shed light onto the molecular mechanisms underlying cell plate orientation.

The movement of POK2 has been shown *in planta* [92] but this movement might be coupled with microtubule dynamics. Therefore, single-molecule imaging in plants would be an interesting way to corroborate the *in vitro* findings presented in this thesis. To this end, a reflected light sheet microscope is custom-built in our laboratory. This microscope can allow fast *in vivo* imaging of low abundant POKs in plants with sufficient spatio-temporal resolution, which is not allowed by confocal and other conventional microscopy. This microscope, operated in a super-resolution mode, might enable visualization and characterization of POK2 kinesin as well as xenosin together, when labelled with different fluorophores. Moreover, this microscope can provide quantitative insights into the dynamics of division site itself with labelled marker proteins and lipids.

POK2 is possibly the earliest kinesin-12 member as supported by the bioinformatic analysis. Therefore, it is instructive to see the localisation of *Chlorophyta* and *Klesbormidium* homologues of POK2 in wild-type and POK mutant background *Arabidopsis* and whether they can rescue the *pok* phenotype. Interestingly, the homology in these lower plants exists even in the C-terminus, therefore, a chimeric construct with the POK2 kinesin motor domain and C-terminus of Streptophyta might even enrich our evolutionary understanding of the plant cell division.

Further insights into the spatial and functional aspects of POK2 at the division site as well as at the phragmoplast midzone can be achieved by electron microscopy (TEM or Cryo-EM). POK1 localisation in *Arabidopsis* is only restricted to the division site [91]. Whether POK1 can also associate with the membrane directly is unclear. A similar truncation approach in POK1 might provide insights into POK1 function.

Ultimately, testing of the phragmoplast pushing model by division site located POKs *in planta* might be essential. This could be achieved by laser ablation experiments of peripheral microtubules and mechanical simulations with measured *in vitro* parameters and phragmoplast expansion data measured *in vivo*.

In conclusion, this thesis has presented data about POK1 and POK2, which is a key step towards an active and dynamic understanding of the division site beyond what can be inferred from localisation studies alone [148]. The phragmoplast pushing model proposed here and in

the published paper [148] highlights the participation of active molecular machines and forces needed for the accurate insertion of cell plates during plant cytokinesis. Such accurate cell plate alignment is a requisite for proper plant growth and development. The findings of an unconventional membrane binding site and a motor—xenosin—in the C-terminal tail domain of POK2 further enriches our molecular and mechanical understanding of cytokinesis. The discovery of xenosin is remarkable as the last microtubule-associated motor was discovered more than 30 years ago. Is xenosin limited to plants or is an overlooked motor in the animal kingdom? How similar xenosin is to other classes of known molecular machines? How does xenosin works mechanically? These are a few intriguing questions. The answers to them require a detailed investigation and may offer opportunities for discovery of new molecular machines.

Contributions

POK2₁₋₅₈₉-GFP and POK1₁₋₅₆₄-GFP were originally cloned and test purified by Maja Reißner. POK2₂₀₈₃₋₂₇₇₁-GFP was cloned by Arvid Herrmann (Dr. Sabine Müller lab, ZMBP). Full-length POK1 was cloned by Caroline Wall and Steffi Zimmermann (Dr. Sabine Müller lab, ZMBP). Native gel protocol was optimized by Simon Schönberg under my supervision. The MSD-SCI analysis scripts were written by Dr. Michael Bugiel. Dr. Michael Bugiel also assisted in MSD-SCI based data analysis and force measurements for POK2₁₋₅₈₉-GFP. Data acquired for POK1₁₋₅₆₄-GFP and POK2₂₀₈₃₋₂₇₇₁-GFP was also contributed by Benedikt Fischer. Confocal imaging of Eb1-MBD in *Arabidopsis* was carried out with Dr. Elisabeth Lipka (Dr. Sabine Müller lab, ZMBP). Benedikt Fisher analysed the POK2C data. Prof. Erik Schäffer and Dr. Basudev Roy derived the MSD equation. Gero Hermsdorf provided the GUVs for and imaged them. The narrowing of division site data was acquired by Dr. Elisabeth Lipka. The samples for electron microscopy and imaging was done with Dr. York Stierhof. Rest of the work in this thesis including conceiving and experimental design, acquisition of data, analysis of data, writing the thesis and was performed by me.

Publications

- **Phragmoplast Orienting Kinesin 2 is a weak motor switching between processive and diffusive modes**
Mayank Chugh, Maja Reißner, Michael Bugiel, Elisabeth Lipka, Arvid Herrmann, Basudev Roy, Sabine Müller, Erik Schäffer
Biophysical Journal, 115.2, 375-385 (2018)
- **Developmentally Regulated GTP binding protein 1 (DRG1) controls microtubule dynamics.**
Anna K. Schellhaus, Daniel Moreno-Andres, Mayank Chugh, Hideki Yokoyama, Athina Moschopoulou, Suman De, Fulvia Bono, Katharina Hipp, Erik Schaeffer, Wolfram Antonin
Scientific Reports, 7.1, (2017)
- **Kinesin-8 depolymerizes microtubules with a force-dependent mechanism**
Michael Bugiel, Mayank Chugh, Erik Schäffer, Anita Jannasch
in preparation
- **Load bearing by EB1 during microtubule bending**
Mohammad A. Kazem, Mayank Chugh, Naghmeh Azadfar, William O. Hancock, Erik Schäffer
in preparation
- **A novel microtubule-associated motor *Xenosin* in plants**
Mayank Chugh, Benedict Fischer, Sabine Müller, Erik Schäffer
in preparation

List of Figures and Tables

1.1. Electron micrograph of a microtubule. A taxol-stabilized microtubule captured at the transmission electron microscope (TEM) in-house facility. The image depicts a microtubule with a hollow cylinder at the bottom and sheet of parallelly arranged tubulin resembling beads on a string called protofilaments as it flattens out at the top. Note that there are more than thirteen protofilaments in this microtubule. This is due to <i>in vitro</i> polymerization of tubulin without nucleating factors and MAPs. Scale bar 100 nm. This figure was captured with Dr. York-Dieter Stierhof.	6
1.2. Schematic of microtubule polymerization. The polymerization of microtubules are powered by attachment of GTP bound tubulin heterodimers (orange-purple) at the growing or plus-ends. This defines the GTP cap region at the microtubule growing end. Subsequently, GTP hydrolysis takes place in the β subunit of the heterodimer, resulting in a GDP bound (cyan-purple) microtubule lattice. This constitutes the minus-end of the microtubules. The GDP-bound state of microtubules leads to detachment of tubulin dimers from the minus-ends, thus creating a turnover of tubulin dimers in solution, which will ultimately power microtubule polymerization. Such tubulin turnover causes microtubule treadmilling.	7
1.3. Molecular addresses of tubulin post-translational modifications (PTMs). The globular tubulin heterodimers on the microtubule lattice expose their C-termini on the outer surface of microtubules. These C-termini also called e-hooks, serve as binding sites for several MAPs. The schematic here depicts common PTMs that occur on tubulin dimers. Most modifications take place on C-tails—polyglycation, polyglutamylation, detyrosination, and $\Delta 2$ -tubulin. Acetylation K40 takes place on α tubulin and in the microtubule luminal surface, while K252 acetylation takes place at the α and β tubulin interphase [22]. These PTMs possibly alter the interaction of microtubule associated proteins. Alphabets denote amino acids. The figure is adapted from [22]	8
1.4. Schematic of actin polymerization. The globular (G)-actin monomers bind ATP and form right-handed strands of filamentous (F)-actin. The barbed ends constitute the growing or plus-ends of the actin filaments while the pointed ends have lower growth rates thus defining minus-ends. Actin assembly and disassembly dynamics is fuelled by ATP hydrolysis and also exhibits treadmilling.	9

<p>1.5. Domain organisation and schematic of conventional kinesin. (<i>Top</i>) Domain organisation of human full-length kinesin-1 Kif5b. The Gray region represents the conserved motor domain that contains microtubule and ATP binding sites. The orange sequence represents the neck linker. The cyan stretches represents coiled-coils in the protein. The coiled-coil results were obtained from PCOILS from MPI toolkit (window 28, probability of 0.99–1) [35]. The white regions represents unstructured regions. (<i>Bottom</i>) Cartoon representation of a kinesin-1 homodimer with its motor domains, neck linker, coiled-coils and unstructured hinges.</p>	11
<p>1.6. Consensus view of the kinesin-1 mechanochemical cycle. Kinesin-1 binds to the microtubule lattice (cyan-purple) in a tethered two-head state (1). This allows rapid release of ADP from the front head creating an apo/ϕ state (2). Subsequently, the rear head turns into an ATP waiting state (3). It is presumed during this state (2-3) transition, kinesin heads are weakly bound and may involve release of inorganic phosphate from the rear head. The front head then binds ATP and triggers a conformation change that allows detachment of the rear head (4). The detached rear hand translocates 8 nm forward (5). In this state (5), kinesin-1 is ideally in a one head-bound state. Thereafter, ATP hydrolysis takes place in the former front head in state (6). This hydrolysis event may lead to a new cycle where the kinesin enters once again in two-head bound state (1) with rear head translocating another 8 nm or undergoes detachment from the microtubule lattice. HB: head bound, NL: neck linker. This figure has been modified from [46].</p>	13
<p>1.7. Schematic representation of dynein. A monomeric dynein motor is presented here, although dyneins are capable of forming higher oligomeric structures such as dimers or trimers. Dyneins bind the microtubules via its microtubule binding domain (violet). This domain is separated from the ATP binding and hydrolysis unit with the help of a coiled-coil called stalk (black). The motor activity of dynein is fuelled by an ATPase ring composed of six individual ATP binding motifs, which belong to the AAA+ superfamily. The hexameric ring is co-ordinated among itself with the help of linker (purple). The linker connects two AAA+ domains and is involved in stepping of the dynein motor. The hexameric ring further controls the microtubule binding domain by modulating the stalk with a buttress (dark orange).</p>	14
<p>1.8. Schematic representation of Myosin. A dimeric myosin-II belonging to conventional myosin family is depicted here. Similar to kinesins, myosin contain a head (violet) that includes an actin binding domain, ATP hydrolysing motif and a huge neck region. The heads are separated from each other with the help of an extended coiled-coil neck region (orange). This neck region serves as prime site for light chain interaction (cyan) and calcium-binding. The neck region is followed up by lengthy coiled-coil domains referred as tail (blue). This tail region also offer interacting sites for the light chains and other molecules. Compared to kinesins, the tail regions in myosins are quite large.</p>	15

- 2.1. **Cytokinesis overview in animals and plants.** (*Left*) In animals, cytokinesis is achieved by formation of the actomyosin based contractile ring (black dashed). The two daughter cells are abscised with the help of midbody—microtubule based structure (red). Nucleus positioning in the daughter cells is done via centrosomal asters (red). (*Right*) In plants, cytokinesis is achieved by the physical insertion of the cell plate in the dividing parent cell. The cell wall, present in plants, poses a physical challenge for cleavage-based separation. The cytokinesis is accomplished by plant-specific microtubule enriched organelle called the phragmoplast (red). 19
- 2.2. **Overview of the plant cell division cycle with focus on the division site.** The rear halves of plant cells are shown from interphase till the cytokinesis in a pseudo 3D rendering. The cell wall/outline is represented in black and is solid in the back plane and dashed towards the lateral and front for visibility purposes. The cortical microtubules (red) undergo reorganisation during interphase thus initiating the selection phase for the division site. During this time the cell's nucleus is also centred. PPB forms during late G2/M phase. During prophase, the PPB (shown in red) is distinctly visible at the cortex. The plasma membrane region, under which the PPB forms, is called the division site and is depicted in grey. This stage marks the appropriate establishment of the division site. The width of the division site is marked by a bracket outside the cell. Following the establishment of the division site, the PPB is disassembled and chromosomes (purple) are split with the mitotic spindle (red). This phase is referred to as maintenance of the division site as the molecular memory persists despite PPB disassembly. Ultimately, the cell plate (grey) is oriented with the expanding phragmoplast (red) towards the division site. During late cytokinesis, the width of the division site is reduced and is referred to as cell plate fusion site (cyan). The figure is adapted from [60] 21
- 2.3. **Cross-section of the phragmoplast structure and cell wall synthesis.** The phragmoplast is composed of a bipolar microtubular array (red) with microtubule plus-ends facing each other in the equatorial plane. Here, microtubules partially overlap. The phragmoplast initially starts as a donought where microtubules serve tracks for Golgi-derived vesicles (green with dashed black outline). The vesicles fuse together in the equatorial plane to form the cell plate (green). The phragmoplast expands centrifugally towards the cell cortex by virtue of the tubulin heterodimer turnover, as microtubules on the inner side depolymerizes (lagging zone). This process derives polymerization of new microtubules on the outer side (leading zone). The cell plate (green) develops and expands simultaneously with the phragmoplast. The direction of phragmoplast expansion (top) and cell wall maturation (bottom) is shown by the arrows. The daughter nuclei are marked in grey-blue with a red dashed outline. The figure is adapted from [98] 23

<p>2.4. Phylogenetic tree of the cell division. Phylogenetic tree representing the evolution of higher land plants from Streptophyte algae—common ancestors of land plants. The green box depicts phragmoplastophyta and the dashed line in the box marks the water-land transition. This diagram describes how Streptophytes including <i>Chlorophyta</i> and <i>Mesostigma</i> utilized cleavage (green H) to Chara and other land plants utilizing the phragmoplast (red H) to achieve cytokinesis. Some Zygnematophytes show both cytokinetic mechanisms. The tree also depicts the origin of the preprophase band (PPB, blue rings) that is evolutionary almost confined to the land plants. The figure has been adapted from [110]</p>	<p>25</p>
<p>7.1. Simplified depiction of forces experienced by a microsphere in an optical trap. When incident light rays hit the microsphere (grey), they undergo refraction and therefore, there is a net change in the momentum of light. Due to conservation of momentum, the microsphere experiences an equal momentum change and in the opposite direction. This momentum change is represented in two cases here. <i>Left</i>, a microsphere is displaced axially and <i>Right</i>, the bead is displaced laterally. The overall forces can be split in two components: gradient and scattering forces (see Section 7.1.1). The figure is adapted from [138]</p>	<p>44</p>
<p>7.2. Schematic of the optical tweezers setup. An infrared laser is focussed on the sample that is mounted on the stage (cyan) by passing through a set of lenses and mirrors and eventually a high NA objective. The piezo-tilt mirror (dark green) and piezo translation stage (light green) play a major role in beam steering relative to the sample. The condenser objective collects the light and reflects it onto a QPD. For microscopy, the sample is illuminated by a blue LED (mounted on top of the tower) and imaged by a zoom adjustable CCD camera. The figure has been adapted from [140]</p>	<p>45</p>
<p>7.3. Schematic illustrating TIRF microscopy. When incident rays beyond a critical angle hit the glass-water or coverslip-sample interface, the light rays undergo total internal reflection. This reflection leads to the creation of an evanescent field at the interface with an exponentially decaying intensity. This enables excitation and detection of fluorophores at or near the interface or cell periphery with a higher signal to noise ratio. The figure is adapted from [141].</p>	<p>46</p>
<p>7.4. Schematic of the TIRF setup used. A 488 nm laser is focussed on the back focal plane of the TIRF objective. Sample is mounted on the sample holder on top of the tower. The emission signal is collected by the same objective and channelled via a slit to a dual-beam splitter that enables imaging in two colour channel separated by the wavelength [142, 143]. The image is projected onto a sCMOS camera. The sample can also be visualised via a blue LED illumination and image projection onto a monochrome camera. * denotes moveable lens for angle adjustment. DM: dichroic mirror, BS: beam splitter.</p>	<p>47</p>
<p>7.5. Schematic illustration of a flow cell. A flow cell consisting of two channels is shown here in two views. It is a sandwich of 22×22 mm coverslip (bottom, white-blue), parafilm (separator, grey), and 18×18 mm coverslip (top, cyan-blue).</p>	<p>49</p>

- 8.1. **Size and domain comparison among kinesin-1, POK2, and POK1.** (*Top*) The full length protein domain organisation for POK2 and POK1 in comparison to conventional kinesin-1 (hKif5b). The colour key depicts associated domains, while white regions represent unstructured or unidentified domains. Coiled coil annotation was achieved using PCOILS and MARCOILS with window size 28 [35]. Coiled coil probabilities of 0.99–1 were considered. aa: amino acids. (*Below*) Table annotating the location of domains in the respective amino acid sequences. 56
- 8.2. **Quality control of POK2_{1–589}-GFP after purification.** (a) 4–20 % Tris-Glycine SDS-PAGE gel coomassie stained for protein fractions. (b) Anti-GFP western blot for purified POK2_{1–589}-GFP fractions. Cat. exc.: cation exchange, Desalt.:desalting, FT: flow through. The figure is modified from [148]. 57
- 8.3. **POK2_{1–589}-GFP is a dimeric kinesin.** (a) An example trace of the fluorescence intensity over time for a single POK2_{1–589}-GFP bound to the microtubule in the presence of 1 mM AMP-PNP. The relative frequencies of bleaching steps are represented in the inset ($N = 105$). (b) A 4–20 % Native PAGE gel depicting monomeric and dimeric state of POK2_{1–589}-GFP (94 kDa monomer) along with dimeric rK430 (80 kDa monomer) and oligomeric bovine serum albumin (BSA, 66 kDa monomer). The figure is modified from [148]. 58
- 8.4. **POK2_{1–589}-GFP is a plus-end-directed motor.** (a) Structural cartoon representation of the POK2_{1–589}-GFP used for *in vitro* experiments in comparison to the full length POK2. The N-terminal extension (*black*) precedes before the motor domain (*grey*). The motor domain contains an ATP binding site (*black strip in grey*). The motor domains are continuous with the neck linker (*orange*) and subsequently first coiled coil (*cyan*). *Green* towards the end represents fused GFP. (b) Predicted coiled-coil probability plot for POK2 (refer Figure 8.1). (c) Schematic of the *in vitro* reconstituted experimental set up. (d) Kymographs representing POK2_{1–589}-GFP motility on the microtubules represented on their left. (e) Polarity-marked microtubule denoting plus-end-directed motion of POK2_{1–589}-GFP. (f) An example montage illustrating POK2_{1–589}-GFP motility. Microtubules are labelled in red and green represents POK2_{1–589}-GFP. Images are 4.75 μm high. Time between frames is 0.5 sec. The figure is modified from [148]. 59
- 8.5. **Quality control of POK2_{183–589}-GFP after purification.** (a) 4–20 % Tris-Glycine SDS-PAGE gel coomassie stained for protein fractions. (b) Anti-GFP western blot for purified POK2_{183–589}-GFP fractions. FT: flow through. The figure is modified from [148]. 60

- 8.6. **POK2₁₈₃₋₅₈₉-GFP is a diffusive motor.** (a) Structural cartoon representation of N-terminal truncated POK2₁₈₃₋₅₈₉-GFP. (b) Exemplary kymographs of POK2₁₈₃₋₅₈₉-GFP diffusive motility on the microtubules represented on their left. (c) Disordered probability plot for POK2 full length. The plot was obtained from IUPRED under default parameters [153]. The blue bars indicate predicted globular/structured regions, while the red line represents disorder tendency estimated from pairwise amino acid energy content. The black line indicates the threshold below which polypeptides are predicted to be structured. The figure is modified from [148]. 61
- 8.7. **Reduced affinity of POK2₁₈₃₋₅₈₉-GFP with the microtubule lattice.** (a) Maximum projections representing the co-localisation of motors onto the microtubule lattice in 1mM AMP-PNP. Images were acquired using TIRF microscopy under the same conditions and contrast. Even though the concentration was about twice that of POK2₁₈₃₋₅₈₉-GFP based on the western blot and nanodrop quantification, much less POK2₁₈₃₋₅₈₉-GFP bound to the microtubules during the same amount of time. (b) Multiple sequence alignment (MSA) of the POK2 N-terminal extension (Nte) with BimC. The MSA was performed using Clustal Omega with default parameters [35]. Asterisks signify conserved residues, colons represent conservation among amino acids exhibiting strongly similar properties, and periods mark conservation among amino acids exhibiting weakly similar properties. Positively charged residues that may interact with the negatively charged tubulin e-hooks are indicated in red. The figure is modified from [148]. 62
- 8.8. **POK2₁₋₅₈₉-GFP switches between processive and diffusive modes.** Distributions of total interaction time (a) and overall displacement (b) of POK2₁₋₅₈₉-GFP on the microtubule lattice are shown. Mean values, \pm SE, and total number of molecules are indicated. (c) The mean-squared-displacement (MSD) of POK2₁₋₅₈₉ and POK2₁₈₃₋₅₈₉ in 1 mM ATP plotted against the lag time is shown. The orange line is a fit of the Eq. 8.3.1 to the POK2₁₋₅₈₉-GFP data, whereas the green line is a linear fit to the POK2₁₈₃₋₅₈₉ data. The error bars are SE of squared-displacement values. The figure is modified from [148]. 63
- 8.9. **SCI analysis can faithfully distinguish motility switches.** (a) Example traces of few POK2₁₋₅₈₉-GFP trajectories for better visulation. Trajectories of (b) all diffusive and (c) all directed segments from tracked single POK2₁₋₅₈₉-GFP molecules. All segments are offset such that they start at zero. Time distributions for (d) diffusive and (e) directed segments single exponentials are plotted as a guide to the eye). (f) speed histogram of directed segments has a Gaussian distribution (magenta line). Mean speed, \pm SE and number of molecules are indicated. The figure is modified from [148]. 65

- 8.10. **System validation for POK2₁₋₅₈₉-GFP diffusive trajectories.** (a-b) represent bias in the POK2₁₋₅₈₉-GFP diffusive segments. Mean-squared displacement (MSD) and (b) mean displacement versus time lag τ for diffusive segments (mean \pm SEM). A linear fit (black line) in (a) resulted in a diffusion coefficient of $0.015 \pm 0.001 \mu\text{m}^2/\text{s}$. A parabolic fit (grey dashed line) did not result in a significant speed. A linear fit (black line) in (b) resulted in a directed bias of $140 \pm 10 \text{ nm/s}$. All fits were weighted by the error bars. (c) Relation between diffusion coefficient and effective speed. Dependence of the diffusion coefficient on the effective speed according to Eq. 8.13 (red line) for a set of fit parameters resulting from a parabolic fit to the MSD relation. Specific directed-mode time fractions ϕ (Eq. 8.14) are indicated by the red circles and numbers. Grey lines indicate the values for POK2₁₋₅₈₉-GFP. The figure is modified from [148]. 66
- 8.11. **POK2₁₋₅₈₉-GFP is a weak motor.** (a) Schematic representation of the force measurement. (b) Representative traces depicting the force of single POK2₁₋₅₈₉-GFP molecules as a function of time (grey line, running median filter over 500 data points: purple line). The blue line marks zero force. Maximal forces are marked by black arrows. (c) Force traces under multi-motor conditions. Force traces of microspheres powered by multiple POK2₁₋₅₈₉-GFP as a function of time. A $10\times$ higher incubation concentration of POK2₁₋₅₈₉-GFP with microspheres was used compared to the single-molecule assays resulting in the motility of 5 out of 6 microspheres. The blue line marks zero force. Arrow heads point to the maximum force prior to detachment events. The figure is modified from [148]. 68
- 8.12. **POK1₁₋₅₆₄-GFP is a plus-end-directed motor.** (a) Structural cartoon representation of the POK1₁₋₅₆₄-GFP used for *in vitro* experiments in comparison to the full length POK1. (b) Predicted coiled-coil probability plot for POK1. (c) Disordered tendency index for POK1 based on the pair wise amino acid energy content (red line). The blue bars represent globular/structured regions, while the black line indicated the threshold (d-e) Kymographs representing POK1₁₋₅₆₄-GFP motility on the microtubules shown on the left. (f) Polarity-marked microtubule displaying POK1₁₋₅₆₄-GFP motility towards microtubule plus-ends. The schematic on the left indicates dark red as the nucleating end and dim red as the growing microtubule end. 69
- 8.13. **Purification trials of POK1 full-length.** (a) Coomassie stained 4-20% Tris-Glycine SDS-PAGE gel showing the protein fraction after the purification. (b) The anti-GFP western blot detects the protein at the wrong size and partially degraded. (c) Fluorescence image of insect cells expressing full-length POK1 shows inclusion-like bodies or aggregates instead of expected cytoplasmic green fluorescence. Cat. exc.: cation exchange, Desalt: desalting, FT: flow-through. 70

8.14. POK1₁₋₅₆₄-GFP also switch motility modes. Distributions of total interaction time (a) and speed for selected trajectories (b) of POK1 ₁₋₅₆₄ -GFP on the microtubule lattice are shown. Mean values \pm SE and total number of molecules are indicated. (c) The mean-squared-displacement (MSD) of POK1 ₁₋₅₈₉ in 1mM ATP plotted against the lag time is shown. The red line is a parabolic fit to the POK1 ₁₋₅₆₄ -GFP data. The error bars are SE of squared-displacement values.	71
8.15. Comparative summary of POK1 and POK2 motility quantification	71
8.16. Multiple POK1₁₋₅₆₄-GFP generate high forces. (a) Schematic representation of the force measurement. (b) Representative traces depicting the force of POK1 ₁₋₅₆₄ -GFP molecules as a function of time (grey line, running median filter over 500 data points: green line). The blue line marks zero force. Maximal forces are marked by black arrows.	72
8.17. Directionality of the phragmoplast peripheral microtubules. <i>Arabidopsis</i> root meristem stably expressing 35S:GFP-MBD and pUBQ:RFPEB1b during late cytokinesis. Plus-ends (RFP-EB1b) marked with arrow heads of peripheral microtubules (GFP-MBD) from the leading edge of the phragmoplast reach out towards the putative division site. The cell boundary is marked with a dashed line. MBD: microtubule binding domain. The figure is modified from [148].	72
8.18. Proposed model for phragmoplast guidance. POK motors (green) localized at the division site push against the leading edge of the expanding phragmoplast by capturing the peripheral microtubules and walking towards their plus-ends. The black arrow marks the direction of the pushing force. This model also supports the narrowing of the division site (orange) to the cell plate fusion site by a mechanical process. POK motors experience a counter force (green arrows). This force focusses the POKs to a precise spot, i.e., the cell plate fusion site. The figure is modified from [148].	74
8.19. Narrowing of the division site. <i>Arabidopsis</i> root meristem expressing YFP-POK1 and RFP-MBD indicating narrowing of the division site from early cytokinesis to the presumably cell plate fusion site during late cytokinesis. For experimental details see reference [91]. The figure is modified from [148].	75
8.20. Possible roles of POKs during cytokinesis. <i>Left</i> Possible tug-of-war mechanism mediated phragmoplast guidance to the cell plate fusion site. POKs (green) and kinesin-14/KCBP (red) both localize at the division site and might interact with the peripheral microtubules with opposite polarity, thus, enabling a push-pull mechanism for accurate cell plate insertion. <i>Right</i> Suggested roles of POK2 at the phragmoplast midzone based on this thesis and the current literature. (A) Transport of cytokinetic vesicles towards the cell division plane. (B) Parallel bundling of microtubules at the phragmoplast and interaction with MAP65-3. (c) Anti-parallel sliding or cross-linking of microtubules at the midzone and interaction with MAP65-3. (D) Regulation of microtubule plus-end dynamics.	76

- 9.1. **Domain and motif analysis of POK2.** Sequence analysis report of POK2 full-length with BLASTp and ELM [170, 171]. *Top* displays full-length POK2 with marked domains as presented in Figure 8.1. When used as query in BLASTp, the superfamilies that find specific and non-specific hits based on the sequence similarities are represented. * denotes the specific hit. Besides the superfamily similarities, selected ELM results are depicted as bars in the predicted regions in the protein sequence. The width of the bars represent the length of the motifs. 80
- 9.2. **Post-purification analysis of POK2_{2083–2771}-GFP.** (a) Coomassie stained 4-20 % Tris-Glycine SDS-PAGE gel with protein purification fractions. (b) Anti-GFP western blot of the purification fractions detects the protein at right size, 110 kDa. CP: cell pellet, S: supernatant, FT: flow through. 81
- 9.3. **POK2 C-terminus contains a secondary microtubule-binding site.** (a) Schematic representation of the POK2_{2083–2771}-GFP construct relative to the full-length POK2. (b) *in vivo* localisation of POK2_{2083–2771}-GFP is marked in green. POK2_{2083–2771}-GFP localizes at the division site through mitosis and cytokinesis [92].(c) Schematic of the *in vitro* experimental set up. (d) TIRF microscopy images depicting the co-localisation fo POK2_{2083–2771}-GFP with the rhodamine-labelled microtubules. 82
- 9.4. **POK2_{2083–2771}-GFP is a plus-end-directed processive motor.** (a-b) Representative kymographs of POK2_{2083–2771}-GFP motility on the microtubule lattice. Respective microtubules are presented on the left. The orange arrow heads point processive trajectories. White asterisk (*) mark some immobile molecules. (c) Single molecule trajectory of POK2_{2083–2771}-GFP depicting the processive slope (orange line). Note that the intensity decreases with time. (d) Polarity-marked microtubule displaying plus-end-directed motility of POK2_{2083–2771}-GFP. The schematic on the left indicates dark red as the nucleating-end and dim red as the growing microtubule-end. 83
- 9.5. **POK2_{2083–2771}-GFP is a slow, processive motor.** Distributions of total interaction times (a), speed calculated manually on the kymographs (b), run length (c) for POK2_{2083–2771}-GFP. 84
- 9.6. **POK2_{2083–2771}-GFP sequence analysis for nucleotide binding.** Manual screening of the POK2_{2083–2771} sequence proposed a P-loop site highlighted in dark red. This P-loop site/Walker A motif is unconventional and is most similar to SmC proteins that hydrolyse ATP. The predicted lysine residues are underlined. Alternative residues for the P-loop are underlined. Apart from a Walker A motif, sites similar to Walker B, ideally characteristic of hhhhDE, h being the hydrophobic residue are also highlighted in the text as cyan. Other non-conventional Walker motifs are marked in green. 85
- 9.7. **POK2_{2083–2771}-GFP has a membrane binding site.** (a) PIP strip showing the interaction of POK2_{2083–2771}-GFP with specific lipids as detected by anti-GFP antibody. The strongest interaction is with PI(4)P and other phosphoinositides. (b) Rhodamine labelled PI(3)P and PI(3,5)P2 enriched GUVs show interaction with POK2_{2083–2771}-GFP. Scale bar 20 μ m. 89

9.8. **Comparative analysis of membrane composition in plants and animal cytokinesis.** (a) Schematic representation of the lipids enriched in the plant cell membrane and developing cell plate. The division site is represented as black dashed line outside the cell. The phragmoplast is shown near the cell plate as dim red lines. (b) Membrane composition at the cytokinetic furrow during animal cytokinesis. The midbody is represented as dim red lines. The figure was created from data in [189–192, 195]. 90

9.9. **POK2_{2083–2771}-GFP does not have an actin-binding site.** (a) Schematic representation of the POK2_{2083–2771}-GFP construct relative to the full-length POK2. (b) Schematic of the *in vitro* experimental set up. (c) TIRF microscopy images depicting no co-localisation of POK2_{2083–2771}-GFP with phalloidin-stabilized actin-filaments in presence of 1 mM ATP. 91

9.10. **Proposed role of full-length POK2 at the division site.** (*Right*) Schematic of a plant cell depicting localisation of POK2 at the division site and denoting cell plate fusion site. (*Centre*) Full-length POK2 anchored at the cell plate fusion site is a dimer with two motors at front (green) and two motors at rear end (red). The POK2 molecules capture the peripheral microtubules from the phragmoplast leading edge and all the four motors walk towards the plus-ends, thus pushing against it. The black arrows show the opposite force acting from the phragmoplast to narrow the division site to cell plate fusion site (Figure 8.19). The kinesin motor domains are responsible for efficient catching and pushing against the phragmoplast. (*Left*) A magnified picture of possible POK2-peripheral microtubule action at the cell plate division site. POK2s are possibly anchored in the membrane with reinforced interaction with MAPs. Due to the separation between the kinesin domain and xenosin (about 230 nm), POK2 can cross-link peripheral microtubules and thus, preventing over-focussing/over-narrowing of the division site. The orange arrows show the counter force to narrowing. Note that the membrane composition here is represented from Fig. 8. 93

9.11. **Proposed role of full-length POK2 at the phragmoplast midzone.** (*Left*) Schematic of a plant cell depicting localisation of POK2 at the division site and the late phragmoplast. (*Centre*) Possible roles of full-length POK2 at the phragmoplast midzone. (*Right*) Favourite hypothesis of POK2 mediated anti-parallel microtubule cross-linking and sliding at the phragmoplast midzone. MAP65 at the midzone stabilises the anti-parallel overlap while POK2 narrows it by sliding them apart in analogy to mitotic spindle midzone. Green arrows mark the direction of sliding. Based on the POK2 C-terminus and lipid interaction, it is believed that POK2 interact with cytokinetic vesicles or the fenestrated sheet in the division plane. Given the contour length of full-length POK2 and the presence of two novel plus-end-directed motors in the C-terminus in POK2 dimer, this might enable parallel bundling of the microtubules in the phragmoplast away from the midzone. 94

9.12. **Phylogenetic tree of the kinesin-12 family in *Arabidopsis*.** (a) Phylogenetic tree representing relationships among the kinesin-12 family with human kinesin-12 as an outroot based on the amino acid sequence alignment. (b) Phylogenetic representation of the kinesin-12 family based on the ancestral relationships. This tree is based upon distance-based phylogeny estimation and involves evolutionary variations at the residue level in estimating the ancestral protein sequence construction. 96

9.13. **Evolutionary origins of POK2.** A phylogenetic tree representing the evolution of higher plants as previously shown in the Figure 2.4. POK2 full-length represented as a whole blue bar in angiosperms is traced back to lower plants and Streptophytes. The blue regions display the sequence similarity with POK2. 97

Acknowledgments

I am grateful to many people and in different ways without whom this thesis would not have been possible.

Firstly, I want to thank my advisor Prof. Erik Schäffer for the opportunity to work on an exciting project in an interdisciplinary research environment and instilling in me a huge interest in single-molecule biophysics. I thank him for the support, guidance, and encouragement that I have received from him during these five years. I am grateful for the freedom he provided, which enabled me to chase my research ideas and helped me grow as a scientist and a person. I am also thankful to him for his demanding high standards and excellent criticism, especially on this thesis. I am inspired by Erik's exquisite expertise in motor mechanics and data analysis.

I am humbled by and grateful to Dr. Sabine Müller for welcoming and including me as a part of her research crew. I thank her for the founding work, on which direction of my work is based. I thank her for the support, advice, encouragement, criticism, and guidance I received from her. The discussions with her have always been stimulating.

I would also like to thank my other committee members, Prof. Ana Garcia-Saez and Prof. Gerd Jürgens, for the ideas, time, and encouragement.

I am grateful to have an overlap with Dr. Suayb Üstun, who inspires me with his infectious and focussed attitude towards science and life. Many thanks for your critical comments on this thesis.

The former and current members of the cellular nanoscience and Müller lab have contributed vastly in my personal and professional time at ZMBP. These people have been a great source of friendships, advice, support, encouragement, and collaboration. I thank Elisabeth Lipka, Maja Rießner, Dorothy Stöckle, Avin Ramaiya, Basudev Roy, Naghmeh Azadfar, Michael Bugiel, Tobias Jachowski, Anita Jannasch, Steve Simmert, Christine Kiefer, Mohammad Kazem Abdosamadi, Gero Hermsdorf, Maria Kharlamova, Swathi Sudhakar, Viktoria Wedler, Benedikt Fischer, Steffi Zimmerman, Arvid Herrmann, and Pantelis Livanos. I would like to specifically thank Christine Kiefer for being an inspiring and supportive colleague as well as a kind and great friend who made my stay and experience in Germany, far from home, way easier and inclusive. I would like to acknowledge Elisabeth Lipka for integrating me in the Müller's lab, for her guidance in experiments, and introducing me to the developmental genetics at ZMBP. I thank cellular nanoscience, general genetics, and developmental genetics departments for making my lab. life fun, comfortable, and eccentric. Thanks to Kyrylo Schenstnyi, Marika Kunst, Angela Dressel, Lena Reister, and Claudia König.

Special thanks to Charly Rehm for tremendous help, advice, and administrative work that made my stay at ZMBP smoother and for being such a positive, kind, and homie spirit.

I gratefully acknowledge the funding and support from International Max Planck Research School 'From molecules to organisms', based at Max Planck Institute for Developmental Biology, Tübingen. I am thankful to Dr. Sarah Danes for her prompt help and support

during the entire course of my graduate program.

My time at ZMBP was made exciting and enjoyable immensely by many friends. I would like to thank Sabine Brumm, Tom Denyer, Christine Kiefer, Avin Ramaiya, Vikas Bhuria, and Kerstin Huhn. A pint is always an answer to good and bad days in the lab! I cannot neglect the names of my constant friends Tieme Helderma, Karandeep Singh, and Meenaskhi Bagadia.

I am very grateful to Sarina Schulze, Martin Schulze, Frederic Aldorf, and Jacob Schulze for including me as a part of their family. I am thankful for all the love, encouragement, constant support, and a home I got from them.

I am indebted to my family for fathomless inspiration, perseverance, encouragement, freedom, love, and constant support. Thank you for everything and being my rock. And most of all, my girlfriend, Maria Kharlamova, for believing in me. Thank you for always being encouraging and patient. Her constant love and support can be summed up in the fact that she is the first one to read through this thesis. Thank you!

Lastly, I would like to acknowledge the espresso coffee machine at ZMBP, my music playlists, and podcasts for getting me through everyday!

11. Appendix: list of primers

Table 11.1.: Used primers for all constructs.

NotI POK2 F	AATAATAACATGCGGCCGCa <u>ATGTCAAAGGAGACCAAGCTTTC</u>
Asc POK2 R	AATAATAACATGGCGCGCC <u>ACTTGATGGCGAATCGACT</u>
EB1b EcoRI F	gaattcAAAAATGGCGACGAACATT
EB1b XhoI R	ctcgagTTAAGTTTGGGTCTCTGCAGCA
GFP-2 R	GAACTTCAGGGTCAGCTTGC
GFP-6 R	CTTGACAGCTCGTCCATGCCGAG
AscI POK2FL R- w/o stop	gaattcAAAAATGGCGACGAACATT
K2409A F	GGTTCAGGGGCTCCTCGGGGTTCTG
K2409A R	CAGAACCCCGAGGAGCCCCTGAACC
K2405A F	TTGAGTGCTGGTTCAGGGAAACCTCG
K2405A R	GGTTCAGGGGCTCCTCGGGGTTCTG
ATN F	AATAATAACATGCGGCCGCa <u>ATGGTTGCAAGAACCCACAGAAGCA</u>
ATN R	AATAATAACATGGCGCGCC <u>CACCTTCCTGCTCTTCATTGGAGAT</u>
GFP-6 F	ctcgcatggacgagctgtacaag
NotI POK2 ₁₈₃₋₅₈₉ F	AATAATAACATGCGGCCGCa <u>ATGGAAGATCCATCTTTCTGGATGGATCACAA</u>

Bibliography

1. Borisy, G., Heald, R., Howard, J., Janke, C., Musacchio, A. & Nogales, E. Microtubules: 50 years on from the discovery of tubulin. *Nat. Rev. Mol. Cell Biol.* **17**, 322 (2016) (cit. on p. ix).
2. Hyman, A. A., Chrétien, D, Arnal, I & Wade, R. H. Structural changes accompanying GTP hydrolysis in microtubules: information from a slowly hydrolyzable analogue guanylyl-(alpha,beta)-methylene-diphosphonate. *J. Cell Biol.* **128**, 117–125 (1995) (cit. on p. 5).
3. Desai, A. & Mitchison, T. J. Microtubule Polymerization Dynamics. *Ann. Rev. Cell Dev. Bio.* **13**. PMID: 9442869, 83–117 (1997) (cit. on p. 6).
4. Mitchison, T. & Kirschner, M. Dynamic instability of microtubule growth. *Nature* **312**, 237 (1984) (cit. on p. 6).
5. Zhang, R., Alushin, G. M., Brown, A. & Nogales, E. Mechanistic Origin of Microtubule Dynamic Instability and Its Modulation by EB Proteins. *Cell* **162**, 849–859 (2015) (cit. on pp. 6, 7).
6. Tran, P., Walker, R. & Salmon, E. A Metastable Intermediate State of Microtubule Dynamic Instability That Differs Significantly between Plus and Minus Ends. *J. Cell Biol.* **138**, 105–117. ISSN: 0021-9525 (1997) (cit. on p. 6).
7. Akhmanova, A. & Steinmetz, M. O. Control of microtubule organization and dynamics: Two ends in the limelight. *Nat. Rev. Mol. Cell. Bio.* **16**, 711–726 (2015) (cit. on pp. 6, 94).
8. Xia, P., Liu, X., Wu, B., Zhang, S., Song, X., Yao, P. Y., Lippincott-Schwartz, J. & Yao, X. Superresolution imaging reveals structural features of EB1 in microtubule plus-end tracking. *Mol. Bio. Cell* **25**, 4166–4173 (2014) (cit. on p. 6).
9. Honnappa, S., Gouveia, S.M., Weisbrich, A., Damberger, F. F., Bhavesh, N. S., Jawhari, H., Grigoriev, I., Rijssel, F. J. van, Buey, R. M., Lawera, A., *et al.* An EB1-binding motif acts as a microtubule tip localization signal. *Cell* **138**, 366–376 (2009) (cit. on p. 6).
10. Akhmanova, A. & Steinmetz, M. O. Microtubule end binding: EBs sense the guanine nucleotide state. *Curr. Biol.* **21**, R283–R285 (2011) (cit. on p. 6).
11. Maurer, S. P., Fourniol, F. J., Bohner, G., Moores, C. A. & Surrey, T. EBs Recognize a Nucleotide-Dependent Structural Cap at Growing Microtubule Ends. *Cell* **149**, 371–382 (2012) (cit. on p. 7).
12. Drechsler, H. & McAinsh, A. D. Kinesin-12 motors cooperate to suppress microtubule catastrophes and drive the formation of parallel microtubule bundles. *Proc. Natl. Acad. Sci. U.S.A.* **113**, E1635–E1644 (2016) (cit. on pp. 7, 13, 24, 93).

13. Microtubule cross-linking triggers the directional motility of kinesin-5. *J. Cell Biol.* **182**, 421–428 (2008) (cit. on pp. 7, 13, 24, 81, 92).
14. Tolić-Nørrelykke, I. M. Push-me-pull-you: how microtubules organize the cell interior. *Eur. Biophys. J.* **37**, 1271–1278 (2008) (cit. on pp. 7, 75, 81).
15. Sturgill, E., Das, D., Takizawa, Y., Shin, Y., Collier, S., Ohi, M., Hwang, W., Lang, M. & Ohi, R. Kinesin-12 Kif15 Targets Kinetochore Fibers through an Intrinsic Two-Step Mechanism. *Curr. Biol.* **24**, 2307–2313 (2014) (cit. on p. 7).
16. Rogers, S. L., Wiedemann, U., Häcker, U., Turck, C. & Vale, R. D. Drosophila RhoGEF2 Associates with Microtubule Plus Ends in an EB1-Dependent Manner. *Curr. Biol.* **14**, 1827–1833 (2004) (cit. on p. 7).
17. Grigoriev, I., Gouveia, S. M., Vaart, B. van der, Demmers, J., Smyth, J. T., Honnappa, S., Splinter, D., Steinmetz, M. O., Putney, J. W., Hoogenraad, C. C. & Akhmanova, A. STIM1 Is a MT-Plus-End-Tracking Protein Involved in Remodeling of the ER. *Curr. Biol.* **18**, 177–182 (2008) (cit. on p. 7).
18. Kim, Y., Heuser, J. E., Waterman, C. M. & Cleveland, D. W. CENP-E combines a slow, processive motor and a flexible coiled coil to produce an essential motile kinetochore tether. *J. Cell Biol.* **181**, 411–419 (cit. on pp. 7, 12, 57, 74, 92).
19. Foley, E. A. & Kapoor, T. M. Microtubule attachment and spindle assembly checkpoint signalling at the kinetochore. *Nat. Rev. Mol. Cell Biol.* **14**, 25 (2013) (cit. on p. 7).
20. Gundersen, G. G., Gomes, E. R. & Wen, Y. Cortical control of microtubule stability and polarization. *Curr. Opin. Cell Biol.* **16**, 106–112 (2004) (cit. on p. 7).
21. Pfister, A. S., Hadjihannas, M. V., Röhrig, W., Schambony, A. & Behrens, J. Amer2 protein interacts with EB1 protein and adenomatous polyposis coli (APC) and controls microtubule stability and cell migration. *J. Bio. Chem.* **287**, 35333–35340 (2012) (cit. on p. 8).
22. Gadadhar, S., Bodakuntla, S., Natarajan, K. & Janke, C. The tubulin code at a glance. *J. Cell Sci.* **130**, 1347–1353 (2017) (cit. on pp. 8, 88).
23. Magiera, M. M. & Janke, C. Post-translational modifications of tubulin. *Curr. Biol.* **24**, R351–R354 (2014) (cit. on p. 8).
24. Barisic, M. & Maiato, H. The Tubulin Code: A Navigation System for Chromosomes during Mitosis. *Trends Cell Biol.* **26**, 766–775 (2016) (cit. on p. 8).
25. Pollard, T. D. Actin and actin-binding proteins. *Cold Spring Harb. Perspect Biol.* **8**, a018226 (2016) (cit. on p. 9).
26. Korn, E. D., Carlier, M.-F. & Pantaloni, D. Actin polymerization and ATP hydrolysis. *Science* **238**, 638–644 (1987) (cit. on p. 9).
27. Wegner, A. Head to tail polymerization of actin. *J. Mol. Bio.* **108**, 139–150 (1976) (cit. on p. 9).
28. Davidson, A. J. & Wood, W. Unravelling the Actin Cytoskeleton: A New Competitive Edge? *Trends Cell Biol.* **26**, 569–576 (2016) (cit. on p. 10).

29. Gittes, F., Mickey, B., Nettleton, J. & Howard, J. Flexural rigidity of microtubules and actin filaments measured from thermal fluctuations in shape. *J. Cell Biol.* **120**, 923–934 (1993) (cit. on p. 10).
30. Bezanilla, M., Gladfelter, A. S., Kovar, D. R. & Lee, W.-L. Cytoskeletal dynamics: a view from the membrane. *J. Cell. Biol.* **209**, 329–337 (2015) (cit. on p. 10).
31. Iwai, S., Ishiji, A., Mabuchi, I. & Sutoh, K. A novel actin-bundling kinesin-related protein from *Dictyostelium discoideum*. *J. Bio. Chem.* **279**, 4696–4704 (2004) (cit. on p. 10).
32. Walter, W. J., Machens, I., Rafeian, F. & Diez, S. The non-processive rice kinesin-14 OsKCH1 transports actin filaments along microtubules with two distinct velocities. *Nat. Plants* **1**, 15111 (2015) (cit. on p. 10).
33. Weber, K. L., Sokac, A. M., Berg, J. S., Cheney, R. E. & Bement, W. M. A microtubule-binding myosin required for nuclear anchoring and spindle assembly. *Nature* **431**, 325–329 (2004) (cit. on p. 10).
34. Vale, R. D., Reese, T. S. & Sheetz, M. P. Identification of a novel force-generating protein, kinesin, involved in microtubule-based motility. *Cell* **42**, 39–50 (1985) (cit. on pp. 11, 12, 27, 86).
35. Zimmermann, L., Stephens, A., Nam, S.-Z., Rau, D., Kübler, J., Lozajic, M., Gabler, F., Söding, J., Lupas, A. N. & Alva, V. A completely reimplemented MPI bioinformatics toolkit with a new HHpred server at its core. *J. Mol. Bio.* **430**, 2237–2243 (2018) (cit. on pp. 11, 55, 56, 62, 95).
36. Vale, R. D. & Fletterick, R. J. The design plan of kinesin motors. *Ann. Rev. Cell Dev. Bio.* **13**, 745–77 (1997) (cit. on pp. 11, 16, 27, 85).
37. Lawrence, C. J., Dawe, R. K., Christie, K. R., Cleveland, D. W., Dawson, S. C., Endow, S. A., Goldstein, L. S., Goodson, H. V., Hirokawa, N., Howard, J., Malmberg, R. L., McIntosh, J. R., Miki, H., Mitchison, T. J., Okada, Y., Reddy, A. S., Saxton, W. M., Schliwa, M., Scholey, J. M., Vale, R. D., Walczak, C. E. & Wordeman, L. A standardized kinesin nomenclature. *J. Cell Biol.* **167**, 19–22 (2004) (cit. on p. 11).
38. Hancock, W. O. & Howard, J. Processivity of the motor protein kinesin requires two heads. *J. Cell Biol.* **140**, 1395–405 (1998) (cit. on pp. 12, 56).
39. Bugiel, M., Fantana, H., Bormuth, V., Trushko, A., Schiemann, F., Howard, J., Schäffer, E. & Jannasch, A. Versatile microsphere attachment of GFP-labeled motors and other tagged proteins with preserved functionality. *J. Biol. Methods* **2.4** (2015) (cit. on pp. 12, 51, 67).
40. Schnitzer, M. J. & Block, S. M. Kinesin hydrolyses one ATP per 8-nm step. *Nature* **388**, 386 (1997) (cit. on p. 12).
41. Howard, J., Hudspeth, A. & Vale, R. Movement of microtubules by single kinesin molecules. *Nature* **342**, 154 (1989) (cit. on p. 12).
42. Block, S. M., Goldstein, L. S. & Schnapp, B. J. Bead movement by single kinesin molecules studied with optical tweezers. *Nature* **348**, 348 (1990) (cit. on pp. 12, 43).

43. Yildiz, A., Tomishige, M., Vale, R. D. & Selvin, P. R. Kinesin walks hand-over-hand. *Science* **303**, 676–678 (2004) (cit. on p. [12](#)).
44. Ramaiya, A., Roy, B., Bugiel, M. & Schäffer, E. Kinesin rotates unidirectionally and generates torque while walking on microtubules. *Proc. Natl. Acad. Sci. U.S.A.* **114**, 10894–10899 (2017) (cit. on pp. [12](#), [28](#), [67](#)).
45. Svoboda, K. & Block, S. M. Force and velocity measured for single kinesin molecules. *Cell* **77**, 773–784 (1994) (cit. on p. [12](#)).
46. Hancock, W. O. The Kinesin-1 Chemomechanical Cycle: Stepping Toward a Consensus. *Biophys. J.* **110**, 1216–1225 (2016) (cit. on pp. [12](#), [13](#)).
47. Gicking, A. M., Wang, P., Liu, C., Mickolajczyk, K. J., Guo, L., Hancock, W. O. & Qiu, W. The Orphan Kinesin PAKRP2 Achieves Processive Motility Via a Noncanonical Stepping Mechanism. *Biophys. J.* **116**, 1270–1281 (2019) (cit. on pp. [12](#), [67](#), [101](#)).
48. Helenius, J., Brouhard, G., Kalaidzidis, Y., Diez, S. & Howard, J. The depolymerizing kinesin MCAK uses lattice diffusion to rapidly target microtubule ends. *Nature* **441**, 115–119 (2006) (cit. on pp. [12](#), [57](#)).
49. Furuta, K. & Toyoshima, Y. Y. Minus-End-Directed Motor Ncd Exhibits Processive Movement that Is Enhanced by Microtubule Bundling In Vitro. *Curr. Biol.* **18**, 152–157 (2008) (cit. on pp. [12](#), [57](#)).
50. Fink, G., Hajdo, L., Skowronek, K. J., Reuther, C., Kasprzak, A. A. & Diez, S. The mitotic kinesin-14 Ncd drives directional microtubule–microtubule sliding. *Nat. Cell Biol.* **11**, 717 (2009) (cit. on pp. [12](#), [57](#)).
51. Kwok, B. H., Kapitein, L. C., Kim, J. H., Peterman, E. J. G., Schmidt, C. F. & Kapoor, T. M. Allosteric inhibition of kinesin-5 modulates its processive directional motility. *Nat. Chem. Biol.* **2**, 480–485 (2006) (cit. on pp. [12](#), [57](#), [81](#)).
52. Drechsler, H., McHugh, T., Singleton, M. R., Carter, N. J. & McAinsh, A. D. The Kinesin-12 Kif15 is a processive track-switching tetramer. *eLife* **3**, e01724 (2014) (cit. on pp. [12](#), [57](#), [67](#), [74](#)).
53. Gibbons, I. R. & Rowe, A. Dynein: a protein with adenosine triphosphatase activity from cilia. *Science* **149**, 424–426 (1965) (cit. on p. [13](#)).
54. Hook, P. & Vallee, R. B. The dynein family at a glance. *J. Cell Sci.* **119**, 4369–4371 (2006) (cit. on p. [13](#)).
55. Mocz, G. & Gibbons, I. R. Model for the motor component of dynein heavy chain based on homology to the AAA family of oligomeric ATPases. *Structure* **9**, 93–103 (2001) (cit. on pp. [13](#), [86](#)).
56. Mallik, R., Carter, B. C., Lex, S. A., King, S. J. & Gross, S. P. Cytoplasmic dynein functions as a gear in response to load. *Nature* **427**, 649 (2004) (cit. on pp. [13](#), [14](#), [43](#)).
57. Nicholas, M. P., Höök, P., Brenner, S., Wynne, C. L., Vallee, R. B. & Gennerich, A. Control of cytoplasmic dynein force production and processivity by its C-terminal domain. *Nat. comm.* **6**, 6206 (2015) (cit. on p. [13](#)).

58. Bhabha, G., Johnson, G. T., Schroeder, C. M. & Vale, R. D. How Dynein Moves Along Microtubules. *Trends Biochem. Sci.* **41**, 94–105 (2016) (cit. on p. 14).
59. Gennerich, A. & Vale, R. D. Walking the walk: how kinesin and dynein coordinate their steps. *Curr. Opin. Cell Biol.* **21**, 59–67 (2009) (cit. on pp. 14, 16, 27).
60. Livanos, P. & Müller, S. Division Plane Establishment and Cytokinesis. *Ann. Rev. Plant Bio.* **70** (2019) (cit. on pp. 14, 15, 20–25).
61. Kühne, W. *Untersuchungen über das Protoplasma und die Contractilität* (W. Engelmann, 1864) (cit. on p. 15).
62. Rayment, I. Kinesin and myosin: Molecular motors with similar engines. *Structure* **4**, 501–504 (1996) (cit. on pp. 15, 16).
63. Hartman, M. A. & Spudich, J. A. The myosin superfamily at a glance. *J. Cell. Sci.* **125**, 1627–1632 (2012) (cit. on p. 15).
64. Yildiz, A., Forkey, J. N., McKinney, S. A., Ha, T., Goldman, Y. E. & Selvin, P. R. Myosin V walks hand-over-hand: single fluorophore imaging with 1.5-nm localization. *science* **300**, 2061–2065 (2003) (cit. on p. 15).
65. Ali, M. Y., Krementsova, E. B., Kennedy, G. G., Mahaffy, R., Pollard, T. D., Trybus, K. M. & Warshaw, D. M. Myosin Va maneuvers through actin intersections and diffuses along microtubules. *Proc. Natl. Acad. Sci.* **104**, 4332–4336 (2007) (cit. on p. 15).
66. Molloy, J., Burns, J., Kendrick-Jones, J, Tregear, R. & White, D. Movement and force produced by a single myosin head. *Nature* **378**, 209 (1995) (cit. on pp. 16, 27, 43).
67. Finer, J. T., Simmons, R. M. & Spudich, J. A. Single myosin molecule mechanics: piconewton forces and nanometre steps. *Nature* **368**, 113 (1994) (cit. on p. 16).
68. Lohner, J., Rupprecht, J.-F., Hu, J., Mandriota, N., Saxena, M., Araujo, D. P. de, Hone, J., Sahin, O., Prost, J. & Sheetz, M. P. Large and reversible myosin-dependent forces in rigidity sensing. *Nat. Physics*, 1 (2019) (cit. on p. 16).
69. Mizuno, N., Toba, S., Edamatsu, M., Watai-Nishii, J., Hirokawa, N., Toyoshima, Y. Y. & Kikkawa, M. Dynein and kinesin share an overlapping microtubule-binding site. *EMBO Journal* **23**, 2459–2467 (2004) (cit. on p. 16).
70. Kull, F. J., Vale, R. D. & Fletterick, R. J. The case for a common ancestor: kinesin and myosin motor proteins and G proteins. *J. Muscle Res. Cell Motil.* **19**, 877–886 (1998) (cit. on pp. 16, 86).
71. Kull, F. J., Sablin, Elena, P, Lau, R., Fletterick, Robert, J & Vale, Ronald, D. Crystal structure of the kinesin motor domain reveals a structural similarity to myosin (Nature Letters). *Nature* **380**, 7–12 (1996) (cit. on p. 16).
72. Saraste, M., Sibbald, P. R. & Wittinghofer, A. The P-loop—a common motif in ATP- and GTP-binding proteins. *Trends in biochemical sciences* **15**, 430–434 (1990) (cit. on pp. 16, 81, 84–86).
73. Leipe, D. D., Wolf, Y. I., Koonin, E. V. & Aravind, L. Classification and evolution of P-loop GTPases and related ATPases. *J. Mol. Bio.* **317**, 41–72 (2002) (cit. on pp. 16, 85, 86).

74. Molecular control of animal cell cytokinesis. *Nat. Cell Biol.* **14**, 440–447 (2012) (cit. on p. 19).
75. Lipka, E., Herrmann, A. & Mueller, S. Mechanisms of plant cell division. *Wiley Interdiscip. Rev. Dev. Biol.* **4**, 391–405 (2015) (cit. on p. 19).
76. Besson, S. & Dumais, J. Universal rule for the symmetric division of plant cells. *Proc. Natl. Acad. Sci.* **108**, 6294–6299 (2011) (cit. on p. 20).
77. Rasmussen, C. G., Wright, A. J. & Müller, S. The role of the cytoskeleton and associated proteins in determination of the plant cell division plane. *The Plant J.* **75**, 258–269 (2013) (cit. on p. 20).
78. Hamant, O. Mechano-devo. *Mech. Dev.* **145**, 2–9 (2017) (cit. on p. 20).
79. Apostolakos, P., Livanos, P., Giannoutsou, E., Panteris, E. & Galatis, B. The intracellular and intercellular cross-talk during subsidiary cell formation in *Zea mays*: Existing and novel components orchestrating cell polarization and asymmetric division. *Ann. Bot.* **122**, 679–696 (2018) (cit. on p. 20).
80. Chakraborty, B., Willemsen, V., Zeeuw, T. de, Liao, C.-Y., Weijers, D., Mulder, B. & Scheres, B. A plausible microtubule-based mechanism for cell division orientation in plant embryogenesis. *Curr. Biol.* **28**, 3031–3043 (2018) (cit. on p. 20).
81. Martinez, P., Allsman, L. A., Brakke, K. A., Hoyt, C., Hayes, J., Liang, H., Neher, W., Rui, Y., Roberts, A. M., Moradifam, A., Goldstein, B., Anderson, C. T. & Rasmussen, C. G. Predicting Division Planes of Three-Dimensional Cells by Soap-Film Minimization. *The Plant Cell* **30**, 2255–2266 (2018) (cit. on p. 20).
82. Camilleri, C., Azimzadeh, J., Pastuglia, M., Bellini, C., Grandjean, O. & Bouchez, D. The Arabidopsis TONNEAU2 gene encodes a putative novel protein phosphatase 2A regulatory subunit essential for the control of the cortical cytoskeleton. *The Plant Cell* **14**, 833–845 (2002) (cit. on p. 20).
83. Dhonukshe, P. & Gadella, T. W. Alteration of microtubule dynamic instability during preprophase band formation revealed by yellow fluorescent protein–CLIP170 microtubule plus-end labeling. *The Plant Cell* **15**, 597–611 (2003) (cit. on p. 20).
84. Smertenko, A., Assaad, F., Baluška, F., Bezanilla, M., Buschmann, H., Drakakaki, G., Hauser, M.-T., Janson, M., Mineyuki, Y., Moore, I., Müller, S., Murata, T., Otegui, M. S., Panteris, E., Rasmussen, C., Schmit, A.-C., Šamaj, J., Samuels, L., Staehelin, L. A., Van Damme, D., Wasteneys, G. & Žárský, V. Plant Cytokinesis: Terminology for Structures and Processes. *Trends Cell Biol.* **27**, 885–894 (2017) (cit. on p. 20).
85. Rasmussen, C. G., Sun, B. & Smith, L. G. Tangled localization at the cortical division site of plant cells occurs by several mechanisms. *J. Cell. Sci.* **124**, 270–9 (2011) (cit. on pp. 20, 21).
86. Stöckle, D., Herrmann, A., Lipka, E., Lauster, T., Gavidia, R., Zimmermann, S. & Müller, S. Putative RopGAPs impact division plane selection and interact with kinesin-12 POK1. *Nat. Plants* **2**, 16120 (2016) (cit. on pp. 20, 22, 75, 77).
87. Müller, S., Han, S. & Smith, L. G. Two kinesins are involved in the spatial control of cytokinesis in *Arabidopsis thaliana*. *Curr. Biol.* **16**, 888–94 (2006) (cit. on pp. 20, 24, 55, 94).

88. Buschmann, H., Dols, J., Kopischke, S., Peña, E. J., Andrade-Navarro, M. A., Heinlein, M., Szymanski, D. B., Zachgo, S., Doonan, J. H. & Lloyd, C. W. Arabidopsis KCBP interacts with AIR9 but stays in the cortical division zone throughout mitosis via its MyTH4-FERM domain. *J. Cell Sci.* **128**, 2033–2046 (2015) (cit. on pp. 20, 22, 77, 82, 94).
89. Xu, X. M., Zhao, Q., Rodrigo-Peirís, T., Brkljacic, J., He, C. S., Müller, S. & Meier, I. RanGAP1 is a continuous marker of the Arabidopsis cell division plane. *Proc. Natl. Acad. Sci. U S A* **105**, 18637–42 (2008) (cit. on pp. 20, 22, 73, 75, 77).
90. Schaefer, E., Belcram, K., Uyttewaal, M., Duroc, Y., Goussot, M., Legland, D., Laruelle, E., Tauzia-Moreau, M.-L. de, Pastuglia, M. & Bouchez, D. The preprophase band of microtubules controls the robustness of division orientation in plants. *Science* **356**, 186–189 (2017) (cit. on pp. 20, 25).
91. Lipka, E., Gadeyne, A., Stöckle, D., Zimmermann, S., De Jaeger, G., Ehrhardt, D. W., Kirik, V., Van Damme, D. & Müller, S. The Phragmoplast-Orienting Kinesin-12 Class Proteins Translate the Positional Information of the Preprophase Band to Establish the Cortical Division Zone in Arabidopsis thaliana. *Plant Cell* **26**, 2617–2632 (2014) (cit. on pp. 21, 24, 68, 73, 75, 94, 95, 102, 103).
92. Herrmann, A., Livanos, P., Lipka, E., Gadeyne, A., Hauser, M., Van Damme, D. & Müller, S. Dual localized kinesin-12 POK2 plays multiple roles during cell division and interacts with MAP65-3. *EMBO Reports* **19**, e46085 (2018) (cit. on pp. 21, 24, 59, 68, 72, 76, 79, 81, 82, 87, 88, 90, 92, 95, 103).
93. Li, H., Sun, B., Sasabe, M., Deng, X., Machida, Y., Lin, H., Julie Lee, Y. & Liu, B. Arabidopsis MAP65-4 plays a role in phragmoplast microtubule organization and marks the cortical cell division site. *New Phytol.* **215**, 187–201 (2017) (cit. on pp. 22, 23).
94. Wu, S.-Z. & Bezanilla, M. Myosin VIII associates with microtubule ends and together with actin plays a role in guiding plant cell division. *eLife* **3**, e03498 (2014) (cit. on pp. 22, 24, 73, 91).
95. Abu-Abied, M., Belausov, E., Hagay, S., Peremyslov, V., Dolja, V. & Sadot, E. Myosin XI-K is involved in root organogenesis, polar auxin transport, and cell division. *Journal of experimental botany* **69**, 2869–2881 (2018) (cit. on pp. 22, 24, 77, 91).
96. Panteris, E. Cortical actin filaments at the division site of mitotic plant cells: a reconsideration of the ‘actin-depleted zone’. *New Phyt.* **179**, 334–341 (2008) (cit. on p. 22).
97. Smertenko, A., Piette, B. & Hussey, P. The Origin of Phragmoplast Asymmetry. *Curr. Biol.* **21**, 1924–1930 (2011) (cit. on pp. 22, 23).
98. Livanos, P., Chugh, M. & Müller, S. in *Plant Protein Secretion* 137–150 (Springer, 2017) (cit. on pp. 22, 23).
99. Smertenko, A., Hewitt, S. L., Jacques, C. N., Kacprzyk, R., Liu, Y., Marcec, M. J., Moyo, L., Ogden, A., Oung, H. M., Schmidt, S., *et al.* Phragmoplast microtubule dynamics—a game of zones. *J. Cell. Sci.* **131**, jcs203331 (2018) (cit. on pp. 22, 23).

100. Janski, N., Masoud, K., Batzenschlager, M., Herzog, E., Evrard, J.-L., Houlné, G., Bourge, M., Chabouté, M.-E. & Schmit, A.-C. The GCP3-interacting proteins GIP1 and GIP2 are required for γ -tubulin complex protein localization, spindle integrity, and chromosomal stability. *The Plant Cell* **24**, 1171–1187 (2012) (cit. on p. 23).
101. Hotta, T., Kong, Z., Ho, C.-M. K., Zeng, C. J. T., Horio, T., Fong, S., Vuong, T., Lee, Y.-R. J. & Liu, B. Characterization of the Arabidopsis augmin complex uncovers its critical function in the assembly of the acentrosomal spindle and phragmoplast microtubule arrays. *The Plant Cell* **24**, 1494–1509 (2012) (cit. on p. 23).
102. Murata, T., Sano, T., Sasabe, M., Nonaka, S., Higashiyama, T., Hasezawa, S., Machida, Y. & Hasebe, M. Mechanism of microtubule array expansion in the cytokinetic phragmoplast. *Nat. Commun.* **4**. doi:10.1038/ncomms2967 (2013) (cit. on p. 23).
103. Yamada, M., Tanaka-Takiguchi, Y., Hayashi, M., Nishina, M. & Goshima, G. Multiple kinesin-14 family members drive microtubule minus end-directed transport in plant cells. *J. Cell. Biol.* **216**, 1705–1714 (2017) (cit. on p. 23).
104. Ho, C.-M. K., Hotta, T., Guo, F., Roberson, R. W., Lee, Y.-R. J. & Liu, B. Interaction of Antiparallel Microtubules in the Phragmoplast Is Mediated by the Microtubule-Associated Protein MAP65-3 in Arabidopsis. *The Plant Cell* **23**, 2909–2923 (2011) (cit. on pp. 23, 24).
105. Sasabe, M., Kosetsu, K., Hidaka, M., Murase, A. & Machida, Y. Arabidopsis thaliana MAP65-1 and MAP65-2 function redundantly with MAP65-3/PLEIADE in cytokinesis downstream of MPK4. *Plant Sign. Beh.* **6**, 743–747 (2011) (cit. on p. 23).
106. Keijzer, J. de, Kieft, H., Ketelaar, T., Goshima, G. & Janson, M. E. Shortening of microtubule overlap regions defines membrane delivery sites during plant cytokinesis. *Curr. Biol.* **27**, 514–520 (2017) (cit. on p. 23).
107. Reddy, A. S. & Day, I. S. Kinesins in the Arabidopsis genome: A comparative analysis among eukaryotes. *BMC Genomics* **2** (2001) (cit. on p. 24).
108. Lee, Y.-R. J., Li, Y. & Liu, B. Two Arabidopsis Phragmoplast-Associated Kinesins Play a Critical Role in Cytokinesis during Male Gametogenesis. *The Plant Cell* **19**, 2595–2605 (2007) (cit. on pp. 24, 95).
109. Miki, T., Naito, H., Nishina, M. & Goshima, G. Endogenous localizome identifies 43 mitotic kinesins in a plant cell. *Proc. Natl. Acad. Sci.* **111**, E1053–E1061 (2014) (cit. on p. 24).
110. Buschmann, H. & Zachgo, S. The Evolution of Cell Division: From Streptophyte Algae to Land Plants. *Trends Plant Sci.* **21**, 872–883 (2016) (cit. on pp. 24, 25).
111. Whitewoods, C. D., Cammarata, J., VENZA, Z. N., Sang, S., Crook, A. D., Aoyama, T., Wang, X. Y., Waller, M., Kamisugi, Y., Cuming, A. C., *et al.* CLAVATA was a genetic novelty for the morphological innovation of 3D growth in land plants. *Curr. Biol.* **28**, 2365–2376 (2018) (cit. on p. 25).
112. Nishiyama, T., Sakayama, H., Vries, J. de, Buschmann, H., Saint-Marcoux, D., Ullrich, K. K., Haas, F. B., Vanderstraeten, L., Becker, D., Lang, D., *et al.* The Chara genome: secondary complexity and implications for plant terrestrialization. *Cell* **174**, 448–464 (2018) (cit. on p. 25).

113. Gest, H. The discovery of microorganisms by Robert Hooke and Antoni Van Leeuwenhoek, fellows of the Royal Society. *Notes and records of the Royal Society of London* **58**, 187–201 (2004) (cit. on p. 27).
114. Eckert, M. Max von Laue and the discovery of X-ray diffraction in 1912. *Ann. Phys.* **524**, A83–A85 (2012) (cit. on p. 27).
115. Ruska, E. The development of the electron microscope and of electron microscopy. *Rev. Modern Phys.* **59**, 627 (1987) (cit. on p. 27).
116. Shimomura, O. The discovery of aequorin and green fluorescent protein. *J. Microscopy* **217**, 3–15 (2005) (cit. on p. 27).
117. Kasten, F. H. in *Cell structure and function by microspectrofluorometry* 3–50 (Elsevier, 1989) (cit. on p. 27).
118. Wright, S. Recombinant DNA technology and its social transformation, 1972-1982. *Osiris* **2**, 303–360 (1986) (cit. on p. 27).
119. Ashkin, A., Dziedzic, J. M., Bjorkholm, J. E. & Chu, S. Observation of a single-beam gradient force optical trap for dielectric particles. *Opt. Lett.* **11**, 288–290 (1986) (cit. on pp. 27, 43).
120. *Once upon a time in the history of microfluidics* <https://www.elflow.com/microfluidic-tutorials/microfluidic-reviews-and-tutorials/history-of-microfluidics/>. [Online; last accessed 20-July-2019] (cit. on p. 27).
121. Verhey, K. J., Kaul, N. & Soppina, V. Kinesin Assembly and Movement in Cells. *Ann. Rev. Biophys.* **40**, 267–288 (2011) (cit. on p. 27).
122. Vale, R. D. The Way Things Move: Looking Under the Hood of Molecular Motor Proteins. *Science* **288**, 88–95 (2002) (cit. on p. 28).
123. Grover, R., Fischer, J., Schwarz, F. W., Walter, W. J., Schwille, P. & Diez, S. Transport efficiency of membrane-anchored kinesin-1 motors depends on motor density and diffusivity. *Proc. Natl. Acad. Sci.* **113**, E7185–E7193 (2016) (cit. on p. 28).
124. *Thermo Scientific TM calculator* <https://www.thermofisher.com/de/de/home/brands/thermo-scientific/molecular-biology/molecular-biology-learning-center/molecular-biology-resource-library/thermo-scientific-web-tools/tm-calculator.html>.. [Online; last accessed 20-July-2019] (cit. on p. 35).
125. *Northwestern University TM calculator* <http://biotools.nubic.northwestern.edu/OligoCalc.html>.. [Online; last accessed 20-July-2019] (cit. on p. 35).
126. *Double digest calculator* <https://www.thermofisher.com/de/de/home/brands/thermo-scientific/molecular-biology/thermo-scientific-restriction-modifying-enzymes/restriction-enzymes-thermo-scientific/double-digest-calculator-thermo-scientific.html>. [Online; last accessed 20-July-2019] (cit. on p. 35).
127. *NEBio calculator* <https://nebiocalculator.neb.com/>. [Online; last accessed 21-July-2019] (cit. on p. 36).
128. Ashkin, A & Dziedzic, J. Optical trapping and manipulation of viruses and bacteria. *Science* **235**, 1517–1520 (1987) (cit. on p. 43).

129. Block, S. M., Blair, D. F. & Berg, H. C. Compliance of bacterial flagella measured with optical tweezers. *Nature* **338**, 514–518 (1989) (cit. on p. 43).
130. Dupuis, D. E., Guilford, W. H., Wu, J. & Warshaw, D. M. Actin filament mechanics in the laser trap. *J. Muscle Res. Cell Motil.* **18**, 17–30 (1997) (cit. on p. 43).
131. Hawkins, T., Mirigian, M., Yasar, M. S. & Ross, J. L. Mechanics of microtubules. *J. Biomech.* **43**, 23–30 (2010) (cit. on p. 43).
132. Wang, M. D., Yin, H., Landick, R., Gelles, J. & Block, S. M. Stretching DNA with optical tweezers. *Biophys. J.* **72**, 1335–1346 (1997) (cit. on p. 43).
133. Wang, M. D., Schnitzer, M. J., Yin, H., Landick, R., Gelles, J. & Block, S. M. Force and Velocity Measured for Single Molecules of RNA Polymerase. *Science* **282**, 902–907 (1998) (cit. on p. 43).
134. Dumont, S., Cheng, W., Serebrov, V., Beran, R. K., Tinoco Jr, I., Pyle, A. M. & Bustamante, C. RNA translocation and unwinding mechanism of HCV NS3 helicase and its coordination by ATP. *Nature* **439**, 105 (2006) (cit. on p. 43).
135. Kellermayer, M. S. Z., Smith, S. B., Granzier, H. L. & Bustamante, C. Folding-Unfolding Transitions in Single Titin Molecules Characterized with Laser Tweezers. *Science* **276**, 1112–1116 (1997) (cit. on p. 43).
136. Smith, D. & Simmons, R. Models of motor-assisted transport of intracellular particles. *Biophys. J.* **80**, 45–68 (2001) (cit. on p. 43).
137. Newton, M. D., Taylor, B. J., Driessen, R. P., Roos, L., Cvetesic, N., Allyjaun, S., Lenhard, B., Cuomo, M. E. & Rueda, D. S. DNA stretching induces Cas9 off-target activity. *Nat. Struc. Mol. Bio.* **1** (2019) (cit. on p. 43).
138. Anita, J. High performance photonic probes and applications of optical tweezers to molecular motors. *PhD Thesis* (2012) (cit. on p. 44).
139. Neuman, K. C. & Block, S. M. Optical trapping. *Rev. Sci. Instrum.* **75**, 2787–2809 (2004) (cit. on p. 43).
140. Mahamdeh, M. & Schäffer, E. Optical tweezers with millikelvin precision of temperature-controlled objectives and base-pair resolution. *Opt. Express* **17**, 17190–17199 (2009) (cit. on pp. 45, 51, 67).
141. Mattheyses, A. L., Simon, S. M. & Rappoport, J. Z. Imaging with total internal reflection fluorescence microscopy for the cell biologist. *J. Cell Sci.* **123**, 3621–3628 (2010) (cit. on p. 46).
142. Simmert, S., Abdosamadi, M. K., Hermsdorf, G. & Schäffer, E. LED-based interference-reflection microscopy combined with optical tweezers for quantitative three-dimensional microtubule imaging. *Opt. express* **26**, 14499–14513 (2018) (cit. on p. 47).
143. Schellhaus, A. K., Moreno-Andrés, D., Chugh, M., Yokoyama, H., Moschopoulou, A., De, S., Bono, F., Hipp, K., Schäffer, E. & Antonin, W. Developmentally Regulated GTP binding protein 1 (DRG1) controls microtubule dynamics. *Sci. Rep.* **7**, 9996 (2017) (cit. on pp. 47, 55).

-
144. Bormuth, V., Varga, V., Howard, J. & Schäffer, E. Protein Friction Limits Diffusive and Directed Movements of Kinesin Motors on Microtubules. *Science* **325**, 870–873 (2009) (cit. on pp. 51, 57, 61, 67).
145. Mahamdeh, M., Campos, C. P. & Schäffer, E. Under-filling trapping objectives optimizes the use of the available laser power in optical tweezers. *Opt. Express* **19**, 11759–11768 (2011) (cit. on p. 51).
146. Tolić-Nørrelykke, S. F., Schäffer, E., Howard, J., Pavone, F. S., Jülicher, F. & Flyvbjerg, H. Calibration of optical tweezers with positional detection in the back focal plane. *Rev. Sci. Instrum.* **77**, 103101 (2006) (cit. on p. 51).
147. Schäffer, E., Nørrelykke, S. F. & Howard, J. Surface forces and drag coefficients of microspheres near a plane surface measured with optical tweezers. *Langmuir* **23**, 3654–3665 (2007) (cit. on p. 51).
148. Chugh, M., Reißner, M., Bugiel, M., Lipka, E., Herrmann, A., Roy, B., Müller, S. & Schäffer, E. Phragmoplast Orienting Kinesin 2 Is a Weak Motor Switching between Processive and Diffusive Modes. *Biophysical J.* **115**, 375–385 (2018) (cit. on pp. 55, 57–63, 65, 66, 68, 72, 74, 75, 103, 104).
149. Tripet, B., Vale, R. D. & Hodges, R. S. Demonstration of Coiled-Coil Interactions within the Kinesin Neck Region Using Synthetic Peptides IMPLICATIONS FOR MOTOR ACTIVITY. *J. Bio. Chem.* **272**, 8946–8956 (1997) (cit. on p. 56).
150. Shin, Y., Du, Y., Collier, S. E., Ohi, M. D., Lang, M. J. & Ohi, R. Biased Brownian motion as a mechanism to facilitate nanometer-scale exploration of the microtubule plus end by a kinesin-8. *Proce. Natl. Acad. Sci. U.S.A.* **112**, E3826–E3835 (2015) (cit. on pp. 57, 60, 67).
151. Lu, H., Ali, M. Y., Bookwalter, C. S., Warshaw, D. M. & Trybus, K. M. Diffusive Movement of Processive Kinesin-1 on Microtubules. *Traffic* **10**, 1429–1438 (2009) (cit. on p. 58).
152. Stock, M. F., Chu, J. & Hackney, D. D. The kinesin family member BimC contains a second microtubule binding region attached to the N terminus of the motor domain. *J. Biol. Chem.* **278**, 52315–52322 (2003) (cit. on p. 58).
153. *Disorder prediction IUPRED* <https://iupred2a.elte.hu/>. [Online; last accessed 20-July-2019] (cit. on p. 61).
154. Ruhnaw, F., Zwicker, D. & Diez, S. Tracking single particles and elongated filaments with nanometer precision. *Biophys. J.* **100**, 2820–2828 (2011) (cit. on p. 59).
155. Moffitt, J. R., Chemla, Y. R. & Bustamante, C. Chapter Ten-Methods in Statistical Kinetics. *Methods Enzymol.* **475**, 221–257. ISSN: 0076-6879 (2010) (cit. on p. 60).
156. Qian, H., Sheetz, M. P. & Elson, E. L. Single particle tracking. Analysis of diffusion and flow in two-dimensional systems. *Biophys. J.* **60**, 910–921 (1991) (cit. on p. 60).
157. Saxton, M. J. & Jacobson, K. SINGLE-PARTICLE TRACKING: Applications to Membrane Dynamics. *Annu. Rev. Biophys. Biomol. Struct.* **26**, 373–399 (1997) (cit. on p. 60).

158. Michalet, X. Mean square displacement analysis of single-particle trajectories with localization error: Brownian motion in an isotropic medium. *Phys. Rev. E*. **82**, 041914 (2010) (cit. on pp. 60, 61).
159. Bouzigues, C. & Dahan, M. Transient directed motions of GABA A receptors in growth cones detected by a speed correlation index. *Biophys. J.* **92**, 654–660 (2007) (cit. on p. 64).
160. Bugiel, M., Jannasch, A. & Schäffer, E. in *Optical Tweezers: Methods and Protocols* (ed Gennerich, A.) 109–136 (Springer Press, New York, NY, 2017) (cit. on p. 67).
161. Jannasch, A., Bormuth, V., Storch, M., Howard, J. & Schäffer, E. Kinesin-8 is a low-force motor protein with a weakly bound slip state. *Biophys. J.* **104**, 2456–2464 (2013) (cit. on pp. 67, 74).
162. McHugh, T., Drechsler, H., McAinsh, A. D., Carter, N. J. & Cross, R. A. Kif15 functions as an active mechanical ratchet. *Mol. Bio. Cell* **29**, 1743–1752 (2018) (cit. on pp. 67, 101).
163. Reinemann, D. N., Sturgill, E. G., Das, D. K., Degen, M. S., Vörös, Z., Hwang, W., Ohi, R. & Lang, M. J. Collective force regulation in anti-parallel microtubule gliding by dimeric Kif15 kinesin motors. *Curr. Biol.* **27**, 2810–2820 (2017) (cit. on pp. 67, 81).
164. Dhonukshe, P., Mathur, J., Hülskamp, M. & Gadella, T. W. J. Microtubule plus-ends reveal essential links between intracellular polarization and localized modulation of endocytosis during division-plane establishment in plant cells. *BMC Biol.* **3**, 11 (2005) (cit. on p. 73).
165. Powers, A. F., Franck, A. D., Gestaut, D. R., Cooper, J., Graczyk, B., Wei, R. R., Wordeman, L., Davis, T. N. & Asbury, C. L. The Ndc80 kinetochore complex forms load-bearing attachments to dynamic microtubule tips via biased diffusion. *Cell* **136**, 865–875 (2009) (cit. on p. 74).
166. Sarangapani, K. K. & Asbury, C. L. Catch and release: how do kinetochores hook the right microtubules during mitosis? *Trends Genet.* **30**, 150–159 (2014) (cit. on p. 74).
167. Hill, T. L. Theoretical problems related to the attachment of microtubules to kinetochores. *Proc. Natl. Acad. Sci. U.S.A.* **82**, 4404–4408 (1985) (cit. on p. 74).
168. Walker, K. L., Müller, S., Moss, D., Ehrhardt, D. W. & Smith, L. G. Arabidopsis TANGLED identifies the division plane throughout mitosis and cytokinesis. *Curr. Biol.* **17**, 1827–36 (2007) (cit. on p. 75).
169. *Uniprot* <https://www.uniprot.org/>. [Online; last accessed 20-July-2019] (cit. on pp. 79, 95).
170. *BLASTp* <https://blast.ncbi.nlm.nih.gov/Blast.cgi?PAGE=Proteins>. [Online; last accessed 21-July-2019] (cit. on pp. 80, 96).
171. *Eukaryotic Linear Motif (ELM) prediction* <http://elm.eu.org/>. [Online; last accessed 20-July-2019] (cit. on p. 80).
172. Hirano, T. The ABCs of SMC proteins: Two-armed ATPases for chromosome condensation, cohesion, and repair. *Genes Dev.* **16**, 399–414 (2002) (cit. on pp. 80, 85, 86).

173. Terakawa, T., Bisht, S., Eeftens, J. M., Dekker, C., Haering, C. H. & Greene, E. C. The condensin complex is a mechanochemical motor that translocates along DNA. *Science* **358**, 672–676 (2017) (cit. on pp. [81](#), [85](#)).
174. Ganji, M., Shaltiel, I. A., Bisht, S., Kim, E., Kalichava, A., Haering, C. H. & Dekker, C. Real-time imaging of DNA loop extrusion by condensin. *Science* **360**, 102–105 (2018) (cit. on pp. [81](#), [85](#)).
175. Graumann, P. L. SMC proteins in bacteria: Condensation motors for chromosome segregation? *Biochimie* **83**, 53–59 (2001) (cit. on p. [81](#)).
176. Weaver, L. N., Ems-McClung, S. C., Stout, J. R., Leblanc, C., Shaw, S. L., Gardner, M. K. & Walczak, C. E. Kif18A uses a microtubule binding site in the tail for plus-end localization and spindle length regulation. *Current Biology* **21**, 1500–1506 (2011) (cit. on p. [82](#)).
177. Su, X., Qiu, W., Gupta Jr, M. L., Pereira-Leal, J. B., Reck-Peterson, S. L. & Pellman, D. Mechanisms underlying the dual-mode regulation of microtubule dynamics by Kip3/kinesin-8. *Mol. cell* **43**, 751–763 (2011) (cit. on p. [82](#)).
178. Narasimhulu, S. B. & Reddy, A. S. N. Characterization of Microtubule Binding Domains in the Arabidopsis Kinesin-Like Calmodulin Binding Protein. *The Plant Cell* **10**, 957. ISSN: 10404651 (2007) (cit. on pp. [82](#), [95](#)).
179. Structural maintenance of chromosome (SMC) proteins link microtubule stability to genome integrity. *J. Bio. Chem.* **289**, 27418–27431 (2014) (cit. on p. [85](#)).
180. Losada, A. & Hirano, T. Dynamic molecular linkers of the genome: The first decade of SMC proteins. *Genes Dev.* **19**, 1269–1287 (2005) (cit. on p. [85](#)).
181. Deltoro, D., Ortiz, D., Ordyan, M., Sippy, J., Oh, C. S., Keller, N., Feiss, M., Catalano, C. E. & Smith, D. E. Walker-A Motif Acts to Coordinate ATP Hydrolysis with Motor Output in Viral DNA Packaging. *J. Mol. Biol.* **428**, 2709–2729 (2016) (cit. on p. [86](#)).
182. Rao, V. B. & Feiss, M. The Bacteriophage DNA Packaging Motor. *Ann. Rev. Gen.* **42**, 647–681 (2008) (cit. on p. [86](#)).
183. Kumar, A., Shukla, S., Mandal, A., Shukla, S., Ambudkar, S. V. & Prasad, R. Divergent signature motifs of nucleotide binding domains of ABC multidrug transporter, CaCdr1p of pathogenic *Candida albicans*, are functionally asymmetric and noninterchangeable. *Biochim. Biophys. Acta Biomembr.* **1798**, 1757–1766 (2010) (cit. on p. [86](#)).
184. Brouhard, G. J., Stear, J. H., Noetzel, T. L., Al-Bassam, J., Kinoshita, K., Harrison, S. C., Howard, J. & Hyman, A. A. XMAP215 is a processive microtubule polymerase. *Cell* **132**, 79–88 (2008) (cit. on p. [87](#)).
185. Geyer, E. A., Miller, M. P., Brautigam, C. A., Biggins, S. & Rice, L. M. Design principles of a microtubule polymerase. *Elife* **7**, e34574 (2018) (cit. on p. [87](#)).
186. Steiner, A., Rybak, K., Altmann, M., McFarlane, H. E., Klaeger, S., Nguyen, N., Facher, E., Ivakov, A., Wanner, G., Kuster, B., *et al.* Cell cycle-regulated PLEIADE/At MAP 65-3 links membrane and microtubule dynamics during plant cytokinesis. *The Plant J.* **88**, 531–541 (2016) (cit. on pp. [88](#), [90](#)).

187. Mao, T., Jin, L., Li, H., Liu, B. & Yuan, M. Two microtubule-associated proteins of the Arabidopsis MAP65 family function differently on microtubules. *Plant Phys.* **138**, 654–662 (2005) (cit. on p. 88).
188. Platre, M. P., Bayle, V., Armengot, L., Bareille, J., Mar Marquès-Bueno, M. del, Creff, A., Maneta-Peyret, L., Fiche, J.-B., Nollmann, M., Miège, C., *et al.* Developmental control of plant Rho GTPase nano-organization by the lipid phosphatidylserine. *Science* **364**, 57–62 (2019) (cit. on p. 89).
189. Platre, M. P., Noack, L. C., Doumane, M., Bayle, V., Simon, M. L. A., Maneta-Peyret, L., Fouillen, L., Stanislas, T., Armengot, L., Pejchar, P., Caillaud, M. C., Potocký, M., Čopič, A., Moreau, P. & Jaillais, Y. A Combinatorial Lipid Code Shapes the Electrostatic Landscape of Plant Endomembranes. *Dev. Cell* **45**, 465–480.e11 (2018) (cit. on pp. 89, 90, 92).
190. Simon, M. L. A., Platre, M. P., Marquès-Bueno, M. M., Armengot, L., Stanislas, T., Bayle, V., Caillaud, M. C. & Jaillais, Y. A PtdIns(4)P-driven electrostatic field controls cell membrane identity and signalling in plants. *Nat. Plants* **2**, 1–10 (2016) (cit. on pp. 89, 90, 92).
191. Tejos, R., Sauer, M., Vanneste, S., Palacios-Gomez, M., Li, H., Heilmann, M., Wijk, R. van, Vermeer, J. E. M., Heilmann, I., Munnik, T. & Friml, J. Bipolar Plasma Membrane Distribution of Phosphoinositides and Their Requirement for Auxin-Mediated Cell Polarity and Patterning in Arabidopsis. *The Plant Cell* **26**, 2114–2128 (2014) (cit. on pp. 89, 90).
192. Heilmann, I. Phosphoinositide signaling in plant development. *Development* **143**, 2044–2055 (2016) (cit. on pp. 89, 90, 92).
193. Nerlich, A., Orlow, M. von, Rontein, D., Hanson, A. D. & Dormann, P. Deficiency in Phosphatidylserine Decarboxylase Activity in the psd1 psd2 psd3 Triple Mutant of Arabidopsis Affects Phosphatidylethanolamine Accumulation in Mitochondria. *Plant Phys.* **144**, 904–914 (2007) (cit. on p. 90).
194. Emoto, K. & Umeda, M. An Essential Role for a Membrane Lipid in Cytokinesis. *J. Cell Biol.* **149**, 1215–1224 (2000) (cit. on p. 90).
195. Brill, J. A., Wong, R. & Wilde, A. Phosphoinositide function in cytokinesis. *Curr. Biol.* **21**, R930–R934 (2011) (cit. on p. 90).
196. Gronnier, J., Crowet, J.-M., Habenstein, B., Nasir, M. N., Bayle, V., Hosy, E., Platre, M. P., Gouguet, P., Raffaele, S., Martinez, D., *et al.* Structural basis for plant plasma membrane protein dynamics and organization into functional nanodomains. *Elife* **6**, e26404 (2017) (cit. on p. 90).
197. Murray, D. H., Jahnel, M., Lauer, J., Avellaneda, M. J., Brouilly, N., Cezanne, A., Morales-Navarrete, H., Perini, E. D., Ferguson, C., Lupas, A. N., *et al.* An endosomal tether undergoes an entropic collapse to bring vesicles together. *Nature* **537**, 107 (2016) (cit. on p. 92).
198. Moreno-Herrero, F., Jager, M. de, Dekker, N. H., Kanaar, R., Wyman, C. & Dekker, C. Mesoscale conformational changes in the DNA-repair complex Rad50/Mre11/Nbs1 upon binding DNA. *Nature* **437**, 440 (2005) (cit. on p. 92).

-
199. Taylor, K. C., Buvoli, M., Korkmaz, E. N., Buvoli, A., Zheng, Y., Heinze, N. T., Cui, Q., Leinwand, L. A. & Rayment, I. Skip residues modulate the structural properties of the myosin rod and guide thick filament assembly. *Proc. Natl. Acad. Sci.* **112**, E3806–E3815 (2015) (cit. on p. 92).
 200. Smith, L. G., Gerttula, S. M., Han, S. & Levy, J. Tangled1: a microtubule binding protein required for the spatial control of cytokinesis in maize. *J. Cell Biol.* **152**, 231–236 (2001) (cit. on p. 94).
 201. Braun, M., Lansky, Z., Fink, G., Ruhnaw, F., Diez, S. & Janson, M. E. Adaptive braking by Ase1 prevents overlapping microtubules from sliding completely apart. *Nat. Cell. Biol.* **13**, 1259 (2011) (cit. on p. 95).
 202. Janson, M. E. & Tran, P. T. Chromosome segregation: organizing overlap at the midzone. *Curr. Biol.* **18**, R308–R311 (2008) (cit. on p. 95).
 203. Minoura, I., Hachikubo, Y., Yamakita, Y., Takazaki, H., Ayukawa, R., Uchimura, S. & Muto, E. Overexpression, purification, and functional analysis of recombinant human tubulin dimer. *FEBS letters* **587**, 3450–3455 (2013) (cit. on p. 102).
 204. Sirajuddin, M., Rice, L. M. & Vale, R. D. Regulation of microtubule motors by tubulin isotypes and post-translational modifications. *Nature cell biology* **16**, 335 (2014) (cit. on p. 102).

Statement of Authorship

Statement of Authorship

I hereby certify that

- I have composed this thesis by myself,
- All references and verbatim extracts have been quoted, and all sources of information have been specifically acknowledged,
- This thesis has not been accepted in any previous application for a degree, neither in total nor in substantial parts.

Eidesstattlicher Versicherung

Ich versichere hiermit, dass ich

- die vorliegende Arbeit selbstständig verfasst habe,
- keine anderen als die angegebenen Quellen benutzt und alle wörtlich oder sinngemäß aus anderen Werken übernommenen Aussagen als solche gekennzeichnet habe
- description und die eingereichte Arbeit weder vollständig noch in wesentlichen Teilen Gegenstand eines anderen Prüfungsverfahrens gewesen ist.

.....
Ort, Datum
Place, Date

.....
Unterschrift/Signature
Mayank Chugh